Internal Dynamics of Equilibrium Colloidal Clusters

Internal Dynamics of Equilibrium Colloidal Clusters

A DISSERTATION PRESENTED
BY
REBECCA WOOD PERRY
TO
THE SCHOOL OF ENGINEERING AND APPLIED SCIENCES

IN PARTIAL FULFILLMENT OF THE REQUIREMENTS
FOR THE DEGREE OF
DOCTOR OF PHILOSOPHY
IN THE SUBJECT OF
APPLIED PHYSICS

HARVARD UNIVERSITY
CAMBRIDGE, MASSACHUSETTS
APRIL 2015

Dissertation Advisor: Professor Vinothan N. Manoharan Rebecca Wood Perry

Internal Dynamics of Equilibrium Colloidal Clusters

Abstract

Colloidal clusters, aggregates of a few micrometer-sized spherical particles, are a model experimental system for understanding the physics of self-assembly and processes such as nucleation. Colloidal clusters are well suited for studies on these topics because they are the simplest colloidal system with internal degrees of freedom. Clusters made from particles that weakly attract one another continually rearrange between different structures. By characterizing these internal dynamics and the structures connected by the rearrangement pathways, we seek to understand the statistical physics underlying self-assembly and equilibration.

In this thesis, we examine the rearrangement dynamics of colloidal clusters and analyze the equilibrium distributions of ground and excited states. We prepare clusters of up to ten microspheres bound by short-range depletion interactions that are tuned to allow equilibration between multiple isostatic arrangements. To study these clusters, we use bright-field and digital holographic microscopy paired with computational post-processing to amass ensemble-averaged and time-averaged probabilities.

We study both two-dimensional (2D) and three-dimensional (3D) clusters composed of either one or two species of particles. To learn about geometrical nucleation barriers, we track rearrangements of particles within freely rotating and translating 3D clusters. We show that rearrangements occur on a timescale of seconds, consistent with diffusion-dominated internal dynamics. To better understand excited states and transition pathways, we track hundreds of rearrangements between degenerate ground states in 2D clusters. We show that the rearrangement rates can be understood using a model with two parameters, which account for the diffusion coefficient along the excited-state

rearrangement pathways and the interaction potential. To explore new methods to control self-assembly, we analyze clusters of two species with different masses and different interactions. We find that the interactions allow for control over the intracluster placement of each species, while the masses have no influence. To provide a theoretical framework for understanding these observations, we derive the classical partition function of colloidal clusters in terms of translational, rotational, and vibrational degrees of freedom. We show that the masses of the particles enter the partition function through the kinetic energy but have no effect on the probabilities of states that differ only in where the masses are placed. This result is consistent with our experiments.

Overall, this work shows that the equilibrium distribution of self-assembled colloidal clusters is well-modeled by classical statistical physics, and that the rearrangement dynamics of colloidal clusters can be understood by incorporating diffusion and the effect of the interaction potential. Because both the structures and dynamics can be accurately predicted, these clusters are a promising system for self-assembling novel materials and for studying the emergence of phase transitions.

Contents

1 Introduction 1
- 1.1 Dynamics of Individual Colloidal Microspheres . . . 3
- 1.2 Interactions of Colloidal Microspheres . . . 4
- 1.3 Geometries of Equilibrium Colloidal Clusters . . . 11
- 1.4 Overview . . . 13

2 Real-Space Studies of the Structure and Dynamics of Self-Assembled Colloidal Clusters 14
- 2.1 Introduction . . . 15
- 2.2 Background . . . 16
- 2.3 Experimental . . . 20
- 2.4 Results and Discussion . . . 30
- 2.5 Conclusions . . . 51

3 2D Clusters of Colloidal Spheres: Ground States, Excited States, and Structural Rearrangements 53
- 3.1 Introduction . . . 54
- 3.2 Experimental Methods . . . 56
- 3.3 Results . . . 59
- 3.4 Analysis . . . 62
- 3.5 Conclusion . . . 69

4 The Partition Function of Colloidal Clusters 71
- 4.1 Partition Functions: from Atoms to Colloids . . . 72
- 4.2 Partition Function in Particle Coordinates . . . 72
- 4.3 Partition Function in Center-of-Mass Coordinates . . . 74
- 4.4 Mass in the Partition Function . . . 78
- 4.5 Calculating Partition Functions for Colloidal Clusters . . . 81
- 4.6 Evidence for the Irrelevance of Mass Distribution . . . 90
- 4.7 Discussion . . . 93

5 Isotope Effects in Colloidal Molecules 97
- 5.1 Self-Assembly of Heterogeneous Colloidal Molecules . . . 97
- 5.2 Experimental and Computational Methods . . . 98
- 5.3 Results . . . 103
- 5.4 Analysis . . . 106

5.5 Conclusion 115

6 Conclusion 117
6.1 Future Work 118

Appendix A Supplemental Movies 121

Appendix B Sample Preparation Protocol 123

Appendix C Occupation Probability Error Bars for Correlated Measurements 125

Appendix D Vibrational Modes of 2D Clusters of Six Particles 130

References 142

Listing of figures

1.1 Trajectory of a microsphere confined to a plane . . . 3
1.2 Debye length as a function of SDS concentration . . . 6
1.3 Combined electrostatic, van der Waals, and depletion interaction potential . . . 8
1.4 Depletion interaction: sphere-sphere and sphere-plate . . . 11
1.5 Ground states for clusters of up to six sticky spheres . . . 12

2.1 Microwell and optical tweezer methods of making clusters . . . 17
2.2 Temperature dependence of PNIPAM . . . 21
2.3 Microwells fabricated from hydrogel . . . 23
2.4 Holographic imaging and optical trapping setup . . . 28
2.5 Concentration dependence of PNIPAM depletion interaction . . . 31
2.6 Temperature dependence of PNIPAM depletion interaction . . . 32
2.7 A 5-particle cluster melts with increased temperature . . . 33
2.8 6-particle ground state probabilities as a function of depletant concentration . . . 35
2.9 Ground states and probabilities for 6- and 7-particle clusters . . . 37
2.10 Ground states and probabilities for 8-particle clusters . . . 38
2.11 Ground states and probabilities for 9- and 10-particle clusters . . . 41
2.12 Bright-field micrographs showing an octahedron to polytetrahedron transition . . . 42
2.13 Holographic fitting and reconstruction . . . 45
2.14 Dynamics of 2-, 3-, and 4-particle clusters including a tetrahedral inversion transition 47
2.15 A 6-particle transition between ground states . . . 49

3.1 Diagram of two-dimensional system . . . 55
3.2 Adjacency matrix . . . 58
3.3 Histogram of interparticle distances in 6-particle clusters . . . 59
3.4 Excited state probability distributions . . . 61
3.5 Transition pathways between 6-particle ground states . . . 66
3.6 Diffusion coefficients of non-rigid 6-particle clusters . . . 67

4.1 Permutations of particles in a 3-particle cluster . . . 82
4.2 Vibrational modes of a 3-particle cluster . . . 84
4.3 Translational partition function: free volume for spherical particles . . . 87
4.4 Translational partition function: free volume for anisotropic clusters . . . 89
4.5 Configurations of particles in a 4-particle cluster . . . 92
4.6 Mass distribution dependence of partition function components . . . 96

5.1 Optically distinguishing silica and polystyrene particles . . . 99

5.2 Automatically distinguishing silica and polystyrene particles 102
5.3 Modified adjacency matrix for colloidal molecules with two species 103
5.4 Selective placement of two species of colloids in small colloidal molecules 104
5.5 Permutations of particles in a 4-particle heterogeneous molecule. 107
5.6 Extreme selectivity of colloidal isotopes 111
5.7 Dependence of colloidal molecule composition on polystyrene fraction 113
5.8 Weighted binomial distribution to model the composition distribution 114

D.1 Vibrational modes of a 6-particle parallelogram 131
D.2 Vibrational modes of a 6-particle chevron 132
D.3 Vibrational modes of a 6-particle triangle 133

Prior Publications

This thesis is primarily based on the following previously published works:

- R. W. Perry, G. Meng, T. G. Dimiduk, J. Fung, and V. N. Manoharan, "Real-space studies of the structure and dynamics of self-assembled colloidal clusters." *Faraday Discussions* 159 (1), 211–234 (2012).
- R. W. Perry, M. C. Cerfon, M. P. Brenner, and V. N. Manoharan, "Two-dimensional clusters of colloidal spheres: ground states, excited states, and structural rearrangements." (in press) *Physical Review Letters* (2015).

Other works to which the author has contributed in graduate school include:

- J. Fung, K. E. Martin, R. W. Perry, D. M. Kaz, R. McGorty, and V. N. Manoharan, "Measuring translational, rotational, and vibrational dynamics in colloids with digital holographic microscopy." *Optics Express* 19 (9), 8051–8065 (2011).
- J. Fung, R. W. Perry, T. G. Dimiduk, and V. N. Manoharan, "Imaging multiple colloidal particles by fitting electromagnetic scattering solutions to digital holograms." *Journal of Quantitative Spectroscopy and Radiative Transfer* 113 (18), 2482–2489 (2012).
- T. Dimiduk, R. W. Perry, J. Fung, and V. N. Manoharan, "Random-subset fitting of digital holograms for fast three-dimensional particle tracking." *Applied Optics* 53 (27), G177-G183 (2014).

Other publications relating to work discussed in this thesis are in preparation.

Acknowledgments

First, I would like to thank my advisor and my dissertation committee. Vinny Manoharan directed me to truly interesting research projects while simultaneously giving me space to branch out. Vinny's simple but sage advice to "take data" led me to uncover new directions for my research. I am particularly thankful for Vinny's strong inclination towards open source software, which opened my eyes to the flexibility that can be gained by developing your own software tools. I appreciate Michael Brenner for organizing my favorite seminar series in which experimentalists present challenges to theorists. Through these seminars, I got to see how Michael and other scientists and mathematicians think about problems, which was one of the most beneficial and enjoyable experiences of my time in graduate school. I also thank Michael for his enthusiasm for collaborations between research groups. I thank Dave Weitz for implementing the 3 o'clock "coffee-and-cookies" break to facilitate cooperation between the research groups on the 5th floor of McKay. During these breaks, I received invaluable advice from members of Dave's Lab. I thank Ian Morrison for encouraging me to apply to graduate school in 2008. I am very appreciative of the consistency Ian provided while I transitioned from Cabot Corporation to Harvard University and am grateful for the scientific knowledge he has imparted to me.

Jerome Fung and Tom Dimiduk devoted inordinate amounts of time to helping me grow as a scientist. Jerome was a willing mentor for me on topics ranging from digital holographic microscopy to academic writing. Tom has been a true ally as I discovered my passion for scientific computing. He was extremely generous with his time and always made for an insightful companion with whom to discuss science. These two scientists also deserve tremendous credit for the work they put into developing the HoloPy software package.

I would like to thank my co-authors Miranda Holmes-Cerfon and Guangnan Meng. Their prior scientific works inspired much of my research, and it was a pleasure to work with them directly. I also thank Beth Chen, with whom I had a wonderful time collaborating on a mathematical question relating to the shapes of two-dimensional clusters.

I would like to thank all the members of the Manoharan Lab, both past and present. A few lab members in particular have made a lasting impression on my graduate school experience. I truly admire Ben Rogers for being the most level-headed scientist I know. Ben always makes time to provide feedback and support for his labmates while still managing to be productive in his own research. Ben does not let anyone off easily, and is able to deliver critiques in a truly constructive manner. He will make a wonderful professor. Having Nick Schade as an accomplice while moving through each step of graduate school has been a huge source of support. Nick is a wonderful public speaker and has generously helped me by unfailingly taking notes of questions asked during each of my practice presentations. It has been particularly fun to discuss science with Nick on the edges of vacations when we were the only ones back in lab from our local holidays. Anna Wang has been a fantastic scientific colleague whose humor keeps things from getting too serious in lab. I thank Aaron Goldfain for his

willingness to get drawn into the "α" problem. I thank Sofia Magkiriadou for letting me bother her on days when I was too hyper to sit quietly at my desk and supporting me with the advice and care of a true friend. Both Dave Kaz and Ryan McGorty deserve recognition for building tools that continue to be used in the Manoharan Lab well past their tenure as graduate students. I have benefited from their work on the überscope and hologram analysis software as well as their friendship. I also look up to Jesse Collins for his determination and his generous curiosity for problems relating to clusters of colloidal spheres and scientific data visualization. I thank Emily Gehrels for many interesting scientific discussions and all she does to cultivate a great environment in the Manoharan Lab. Finally, I would like to thank Ellen Klein for her contagious enthusiasm for her own projects on colloidal clusters which got me reinvigorated about my own research in these last couple of months.

I had the good fortune of making strong connections with graduate students in other labs and universities. I received countless pieces of advice from Don Aubrecht during the daily coffee-and-cookies breaks as well as during some of the lowest points in my time as a graduate student. Don also provided feedback on the first draft of this thesis, for which I cannot thank him enough. For encouraging my interest in computational science, I owe thanks to Tom Caswell and Dan Allan for organizing a Software for Soft Matter group. Tom and Dan are also the incredibly responsive and supportive authors of a particle tracking software package, Trackpy, which I used for some of the work in this thesis.

I owe much gratitude to those who simplified the logistics of being a graduate student. I thank Barbara Drauschke and Glenda Guerra for all they do to keep the Manoharan Lab running smoothly and for many friendly conversations. I also thank Barbara for facilitating all of my conference trips. I thank Jordan Suchow for generously sharing and maintaining the LaTeX template I used to format this thesis.

I could not have asked for better resources for research. I am grateful for the funding I received from the National Science Foundation through grant no. DMR-1306410 and Harvard MRSEC, grant no. DMR-1420570. I would also like to acknowledge the support I received from a National Science Foundation Graduate Research Fellowship and from Harvard's School of Engineering and Applied Sciences. Harvard's FAS Division of Science, Research Computing Group deserves thanks for supporting the Odyssey cluster on which I performed many hologram fits. I dream of a time when all journals will be open access, but as that is not yet the case, I am very grateful for the access Harvard provides to academic journals.

I certainly would not be at this point in my education without many teachers and mentors who helped me along the way. Some of the most influential were Heidi Kaiter, Ellen Turner, Dick Peller, Stephen Naculich, Karen Topp, Mark Battle, and Ariel Balter.

During the course of my PhD I have received support from a host of friends. In particular, Emily Pratt and Haley Bridger helped me prepare for my qualifying exam. I thank Naveen Sinha for his support via various means – from early morning runs to catching up over cocktails. Naveen's strategies for productivity and enthusiasm for trying new things are inspiring. I thank Mike Marineau for being a peaceful person to co-work with. I attribute my precise defense time, 2:00 PM, to Peter Kinnaird who always convinced me it was alright to take a coffee break with him because I could just "graduate half an hour later." And to those who have supported me personally or professionally: Julia

Novak, Zsofia Botyanszki, Stacy Wong, Shanying Cui, Kelly Miller, Kasey Phillips, Bitsy Perlman, EB Sheldon-Morris, Josh Chase, Liz Raible, and Jay Pottharst. I value their friendship which has stayed strong even during times when I did not have a whole lot to give back.

I owe deepest thanks to Gill, Nick, and Carlin Thompson who provided much needed escapes during the hardest parts of graduate school by welcoming me to their idyllic island farm in Maine. Gill also introduced me to Acadia who has kept me company during countless hours of work and listened to many practice talks.

I sincerely thank Matt Berntsen for keeping me grounded and reminding me to breathe. Matt took it upon himself to remind me of how much I love science during times I was struggling with it. Matt has shown me the power of steadfast support.

Lastly, it is with great appreciation that I thank my family for considering my endeavors to be worthwhile. Thank you to my sister and brother-in law, Kate and Jody Kaufman, for providing much needed breaks and being interested in my research. My father, Ned Perry, coached me on many soccer teams when I was young and taught me how to play many sports that have been a form of stress relief for me during graduate school. My mother, Cynthia Wood, made science a normal thing to play with as a child. She also set me (perhaps unwittingly) on a path towards studying soft matter science from a young age by teaching me about the angle of repose of granular materials and about liquid minisci while baking together. Finally, I thank my grandfather, Edwin Wood, who is the most widely-read person I know. I look up to him because of his intellectual curiosity and the critical analysis he brings to any discussion. Thank you to all my family members for their love and support.

1

Introduction

Self-assembly in nature reliably produces structures such as viruses, micelles, and crystals from smaller-scale interacting components. Each of these components must come together in just the right way to yield a product with dependable material and functional properties. Naturally self-assembled structures are used in a wide range of applications, including gene-therapy (viruses), detergents (micelles), and drilling (crystals). Appropriating self-assembly to economically manufacture novel nano- and micro-scale structures is a central goal of current research.[1] Two recent successes include the self-assembly of a nano-scale box with a controllable lid made from DNA,[2] and the self-assembly of pigment-free colorful spheres.[3,4]

One approach to engineering self-assembled structures is to controllably aggregate nano- or micro-scale building blocks, the simplest of which are colloidal microspheres. Silica and polystyrene microspheres are readily synthesized in large batches and are small enough to be Brownian, but large enough

to be observed with an optical microscope. To successfully self-assemble a functional object out of microspheres, the components must come together into the desired configuration, perhaps incorporating microspheres with different material properties into specific positions.

Colloidal microspheres are typically stabilized against aggregation by a repulsive interaction, but an attractive interaction can be engineered and added to sculpt a desired interaction potential. The added attractive interaction can be chosen from a diverse set of options including depletion,[5,6,7] grafted DNA,[8,9,10] and magnetism.[11,12] One approach to directing the self-assembly of colloidal structures is to change the interaction potential by modifying the surfaces of the particles, giving them specificity or directionality, for example, DNA-coated particles, lock and key particles,[13] and janus particles.[14] The counterpart to these approaches using specific and anisotropic particles is the self-assembly of identical isotropic building blocks.[15,16,17] There is still much to be learned from the self-assembly of even these simple isotropic building blocks.

Small aggregates, or clusters, of a few microspheres exhibit dynamics that can help us understand the physics of self-assembly. This thesis presents the results of experiments on isotropic colloidal microspheres assembled into two-dimensional (2D) and three-dimensional (3D) clusters containing up to 6 particles. The particles are bound together weakly enough to allow equilibration at room temperature. In this chapter, I bring together background information on how individual Brownian particles join together to make geometrically interesting, dynamic clusters. In subsequent chapters, we explore the rich collection of excited states that the clusters access by breaking bonds to transition between ground states in three dimensions (Chapter 2) and in two dimensions (Chapter 3). We develop a statistical mechanical model of the equilibrium distributions of isostatic clusters showing how highly-symmetric clusters and clusters with high normal mode frequencies are suppressed while clusters with large radii of gyration are enhanced (Chapter 4). Lastly, we present experiments that reveal design criteria for self-assembling specific clusters of two species of particles using three different interparticle interactions (Chapter 5).

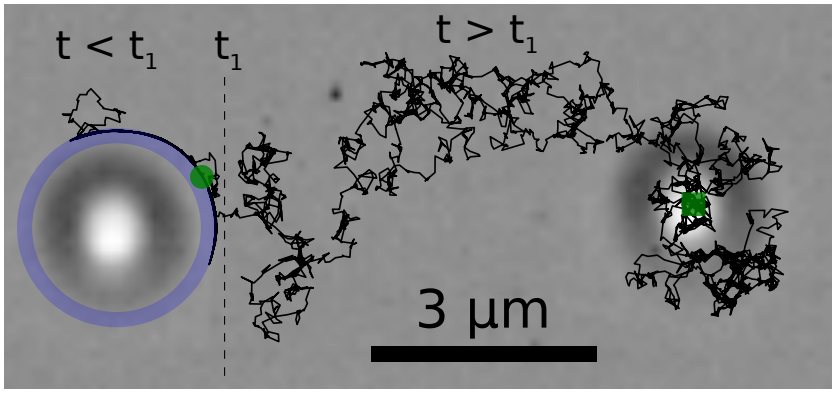

Figure 1.1: The trajectory[18] of a 1.3 µm diameter polystrene sphere from the initial position marked with a green circle to the position marked with a green square shows two regimes: at times less than t_1 the particle is bound to both a glass coverslip and to the static particle at the left side of the image and so diffuses only along the circle marked in blue (with small excursions). Around time t_1 the mobile particle breaks away from the static particle and diffuses across the coverslip to the location shown in the micrograph and marked with a green square.

1.1 Dynamics of Individual Colloidal Microspheres

Systems of isolated colloidal microspheres have interesting dynamics that have been instrumental in the understanding of condensed matter physics. For example, the dynamics of single spherical particles confirmed the molecular theory of matter. In 1905, Einstein described how the mean square displacement of micrometer-sized particles in suspension would scale with time if their motion was caused by random thermal motion of discrete molecules composing the continuous phase[19]:

$$\langle \Delta x^2 \rangle = (2n) D \Delta t, \tag{1.1}$$

where n is the number of spatial dimensions included in the measurement of the displacements Δx, and Δt is the period of time over which each displacement is measured. Einstein's formulation of the diffusion coefficient, D, provides the connection to the thermal energy[19]:

$$D = \frac{k_B T}{6\pi\eta a}, \tag{1.2}$$

where k_B is Boltzmann's constant (the gas constant divided by Avogadro's number), T is the temperature, η is the viscosity of the continuous phase, and a is the radius of a particle. Equation 1.2 is called the Stokes-Einstein equation. In experiments designed to test Einstein's prediction, Perrin measured that the mean square displacement of Brownian microspheres in fact obeys Equation 1.1 with D given by Equation 1.2, thus showing that matter is composed of discrete units.[20] Today, the experiment painstakingly carried out by Perrin and his student Chaudesaigues can be repeated with commercially available microspheres, a microscope, a digital camera, and particle tracking algorithms.[21,18] Indeed, we replicate Perrin's work in the course of this thesis to measure diffusion coefficients.

Colloids have continued to be useful as experimental systems for investigations in condensed matter. For example, colloidal microspheres can be used as model atoms. Like collections of atoms or molecules, suspensions of microspheres have solid and fluid phases.[22,23] They can be used to study phenomena such as crystallization (Chapter 2) and epitaxy.[24] While we can use colloids as models of atomic systems, colloidal particles are certainly not identical to atoms. One important difference between colloidal particles and atoms is that colloidal particles are classical and distinguishable (in principal) whereas atoms are not. We discuss how to incorporate the distinguishability of the particles into a statistical mechanical model in Chapter 4.

1.2 Interactions of Colloidal Microspheres

The interactions between colloidal microspheres are tunable. This allows us to design the interactions to obtain desired structures and dynamics. For all of the experiments in this thesis, we create interactions with a short range, around 10% of the particle diameter. The behaviors resulting from different short-range interaction potentials vary greatly: particles can bind, not bind, or bind temporarily, and bound particles can be free to rotate with respect to each other or their relative orientations can be fixed. For our studies of rearrangement dynamics, we want particles to bind temporarily and be free

to roll or slide around each other.

To establish a framework for designing an interaction, we turn to theories of colloidal interaction potentials. While there are many different interparticle interactions, here I introduce only the three types of interactions that are relevant to later chapters: electrostatic repulsion, van der Waals attraction, and depletion attraction. To show the contribution that any one factor has on the interaction, I present the components of the modeled interaction potential as a function of the distance between the surfaces of two particles. All interaction potentials are given in units of k_BT. With increasing interparticle distance, a purely repulsive interaction potential monotonically decreases and a purely attractive interaction potential monotonically increases. The most interesting interaction potentials, however, are balanced combinations of both repulsive and attractive interactions that yield an energy minimum . When two particles get caught in an energy minimum, we call them "bound," in analogy to chemical bonds.

1.2.1 DLVO theory: van der Waals and Electrostatic Interaction

The primary repulsive interaction stabilizing like-charged colloids against aggregation is electrostatic. DLVO theory models the interaction between charged particles as the sum of an electrostatic interaction and a van der Waals attraction.[25] The theory explains why particles irreversibly aggregate when salt is added: ions screen the repulsive electrostatic interaction, allowing the van der Waals attraction to dominate. The length scale of the electrostatic repulsion is the Debye length, with the following dependence on the salt concentration ρ:

$$\kappa^{-1} = \sqrt{\frac{k_BT\epsilon_0\epsilon}{2Z^2e^2\rho}}, \tag{1.3}$$

where k_B is Boltzmann's constant, T is the temperature, ϵ_0 is the dielectric permitivity of the vaccuum, ϵ is the dielectric constant, Z is the valency of the ions, and e is the fundamental charge.[25] For reference,

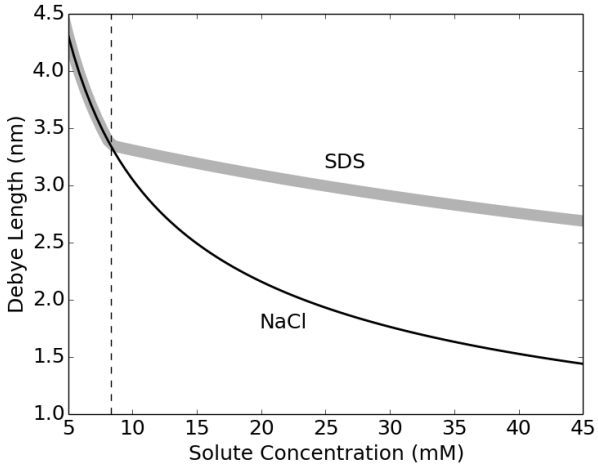

Figure 1.2: Debye length as a function of concentration of NaCl (Equation 1.3) or Sodium Dedecyl Sulfate (SDS) (Equation 1.4). Below the critical micelle concentration (indicated by a dashed line), the concentrations of SDS and NaCl affect the Debye length identically. Above the critical micelle concentration, the Debye length reduces more rapidly with NaCl concentration than with SDS concentration.

an aqueous solution of 30 mM NaCl ($\epsilon = 78.4$,[25] $Z = 1, T = 298$) has a Debye length of 1.76 nm.

The Debye length can also be reduced by ionic surfactants. Below the critical micelle concentation (CMC), all of the surfactant molecules dissociate and affect the Debye length identically to a salt. Above the CMC, some of the molecules in micelles also release their counterions into solution. The co-ion stays with the micelle and has a negligible effect on the Debye length[26] (Figure 1.2). For SDS, the CMC is around 8 mM,[27] and the fraction of molecules in a micelle that dissociate, β, is estimated to be 0.25.[26] The Debye length can be calculated by replacing the salt concentration with the concentration of dissociated ions, where ρ_t is the total concentration of surfactant[26]:

$$\kappa^{-1} = \sqrt{\frac{k_B T \epsilon_0 \epsilon}{2Z^2 e^2 (\rho_{cmc} + \frac{1}{2}(\rho_t - \rho_{cmc})\beta)}} \tag{1.4}$$

With Equations 1.3 and 1.4 for the Debye length in terms of salt or surfactant concentration, we can now express the electrostatic interaction potential as an experimentally-tunable interaction. Salt

and surfactant concentrations are easy to modify when preparing a sample and affect the Debye length, which relates to the electrostatic potential. For particles with constant surface charge as a function of interparticle separation distance, such as sulfate polystyrene microspheres, the electrostatic contribution to the interaction potential is[28,16]:

$$\frac{U(x)}{k_BT} = Z_p^2 \frac{e^2}{4\pi\epsilon\epsilon_0 k_BT}\left(\frac{e^{\kappa a}}{1+\kappa a}\right)^2 \frac{e^{-\kappa(x+2a)}}{x+2a}, \tag{1.5}$$

where Z_p is the charge on a colloidal particle.

The other contribution in the DLVO theory is the van der Waals attraction, which has a large contribution to the potential at short range. According to Hamaker thoery, the van der Waals interaction between two spheres is given by[25]:

$$\frac{U(x)}{k_BT} = \frac{1}{k_BT}\frac{-Aa}{12x} \tag{1.6}$$

where A, the Hamaker constant, is specific to the materials of the dispersed and continuous phases. The van der Waals attraction is not as easily tuned as the electrostatic repulsion.

The sum of Equations 1.5 and 1.6 is the potential described by DLVO theory. Figure 1.3a shows an interaction potential that combines electrostatic and van der Waals contributions calculated using parameters relevant to our colloidal system: a = 500 nm, sulfate polystyrene charge density = 8 μC/cm^2 or, equivalently, $Z = 1.6 \times 10^6$ negative charges per particle (similar to the charge of 1 μm sulfate polystyrene microspheres from Life Technologies™), ϵ=78.4[25], κ^{-1}= 3.4 nm, T = 298 K, and A = 1×10^{-21} J.[25]

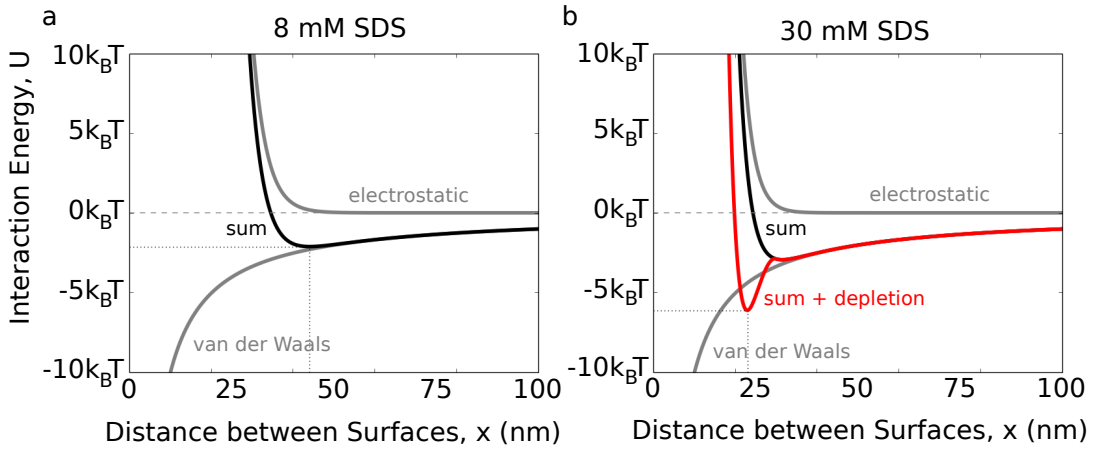

Figure 1.3: Theoretical interaction potentials for two concentrations of SDS including electrostatic, van der Waals, and depletion interactions. (a) The concentration of SDS is set to the CMC. Approximately all the surfactant molecules dissociate and have the same effect on the electrostatic interaction as a monovalent salt would at the same concentration. A shallow secondary minimum exists around 45 nm. (b) At 30 mM SDS, there are both more ions in solution and micelles, which act as depletants. The depletion interaction is purely attractive and contributes at distances less than 30 nm ($2a_s$). Both potentials have a primary minimum, near zero distance, that is not visible here. Interaction curves are calculated from Equations 1.4 -1.10 (see text for parameters).

1.2.2 Depletion Interaction

The depletion interaction is a purely attractive, entropic interaction.[5,6] To generate a depletion interaction in a colloidal suspension, a high number-density of smaller spheres, called depletants, is added. Hard-sphere depletants cannot go within a small-sphere-radius a_s of any surface. This results in a region, called the excluded volume, that lies around every surface and that is depleted of smaller spheres. If two surfaces come close together such that their excluded volumes overlap, more volume is accessible to the depletants elsewhere in the suspension, increasing the total entropy of the system. The amount by which the excluded volumes overlap is aptly named the overlap volume.

The depletion interaction is experimentally useful for tuning the overall interaction potential because its range and depth are controlled primarily by the size and number density of the depletants, two parameters that can easily be changed when preparing a colloidal suspension. The range of the depletion attraction is approximately the diameter of the smaller spheres, which can include polymers, smaller colloidal microspheres, and self-assembled micelles. The strength of the depletion attraction depends linearly on the number density of depletants in the bulk.[29]

While the range of the depletion attraction is set by the choice of depletant, the strength of the depletion attraction additionally depends on the curvature of the interacting objects, through the overlap volume. Assuming hard-sphere interactions between the depletants and objects and ignoring interactions between the depletants, the depletion attraction takes the following form[29]:

$$\frac{U(x)}{k_B T} = \begin{cases} -\rho_s V_{ov}(x) & : x < 2a_s \\ 0 & : x \geq 2a_s \end{cases} \tag{1.7}$$

The overlap volume is a function of the distance, x, between the objects' surfaces (Figure 1.4). For two neighboring spheres of equal diameter, the overlap volume takes the shape of a biconvex lens constructed from two identical spherical caps. The volume of a spherical cap can be written in terms

of its height h and the sphere radius s [30]:

$$V_{cap}(h,s) = \frac{\pi}{3}h^2(3s-h) \tag{1.8}$$

Each of the two spherical caps has $h = (2a_s - x)/2$ and $s = a_l + a_s$. The overlap volume simplifies to[29]:

$$\text{sphere-sphere: } V_{ov}(x) = 2V_{cap}\left(\frac{2a_s - x}{2}, a_l + a_s\right) = \frac{\pi}{6}(2a_s - x)^2\left(3a_l + 2a_s + \frac{x}{2}\right) \tag{1.9}$$

In contrast, for a sphere close to a flat plate, the overlap volume is a single spherical cap with $h = 2a_s - x$ and radius $s = a_l + a_s$.[29]

$$\text{sphere-plate: } V_{ov}(x) = V_{cap}(2a_s - x, a_l + a_s) = \frac{\pi}{3}(2a_s - x)^2(3a_l + a_s + x) \tag{1.10}$$

At any surface-to-surface distance, the overlap volume, and thus the depletion potential, between a sphere and a plate approaches double that between two spheres in the limit where $a_l >> a_s$ (Figure 1.4). Because the overlap volume is doubled, the depletion interaction strength is also doubled.[31,29] We use this curvature-dependence of the depletion interaction potential in Chapters 3 and 5 to induce temporary bonds between particles and more permanent bonds between particles and a coverslip.

To summarize the interactions I have presented in this section, I show a calculated potential for the combined effect of electrostatic, van der Waals, and depletion interactions (Equations 1.5, 1.6, and 1.7) between polystyrene microspheres in Figure 1.3b using: a_l = 500 nm, a_s= 15 nm, ρ_s = $2.2 \times 10^5\,\mu\text{m}^{-3}$, and the same parameters used for the electrostatic and van der Waals interactions in Figure 1.3a. The size we select for a_s is much larger than the physical radius of an SDS micelle (2.4 nm[27]) because Iracki *et al.* have shown that charged depletants act with an effective radius extending 4.7 Debye lengths beyond their physical radius.[27]

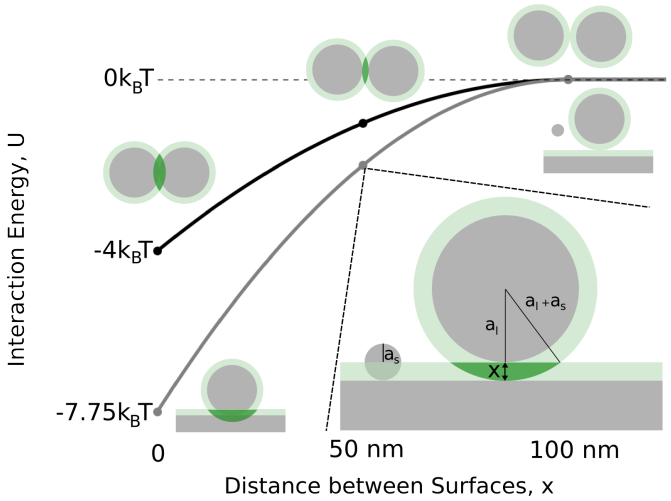

Figure 1.4: In a suspension of 1 μm diameter spheres, 100 nm depletants induce an attractive interaction of a few k_BT at distances less than 100 nm. Illustrations at three points along both potentials show that the overlap volumes (bright green) of the depletion zones (pale green) decrease as the distance increases. At all distances, the depth of the depletion interaction potential between a sphere and a flat surface is approximately twice that between two spheres. Calculations use a depletant volume fraction of 0.25 ($\rho_s = 480\,\mu\text{m}^{-3}$). The depletants are not drawn to scale.

1.3 Geometries of Equilibrium Colloidal Clusters

When an interaction potential has been tuned to support the formation of clusters and allow particle rearrangements, the resulting clusters will often be found in ground states. For clusters of N isotropic particles with short-range interactions like ours, the ground states maximize the number of bonds, leading to the structures shown in Figure 1.5.[32,33,34] These ground states are rigid structures that satisfy Maxwell's criterion for stiffness of having at least $2N - 3$ bonds in two dimensions and at least $3N - 6$ bonds in three dimensions.[35] The number of bonds required by Maxwell's criterion is equal to the number of coordinates needed to describe the positions of all the particles minus the number of translational and rotational degrees of freedom of the cluster. We have experimentally observed all of the ground states in Figure 1.5 using systems of depletion-bound polystyrene microspheres (Chapters 2 and 3).[16]

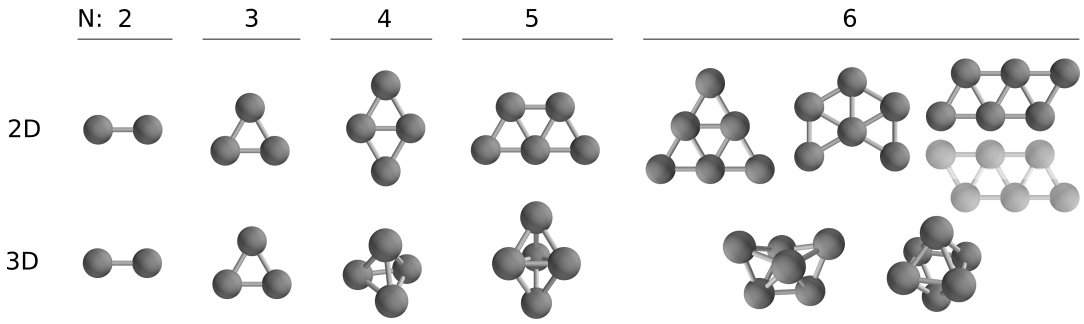

Figure 1.5: The ground states of sticky hard-sphere clusters in two and three dimensions. In both cases the clusters at $N = 6$ have degenerate ground states. The 2D 6-sphere parallelogram has an enantomeric copy. The particles and bonds are represented by balls and sticks for the purposes of illustration. Realistic colloidal clusters with short-range interactions have minimal gaps between particles.

While the smallest clusters have single ground states, the 2D and 3D clusters of six particles have degenerate ground states. Degenerate ground states are interesting because they have the same potential energy but not necessarily the same free energy, which determines their probabilities.[16] By looking at an ensemble of 3D equilibrium clusters, Meng and collaborators found that the 6-particle octahedral ground state is rare compared to the other 6-particle ground state, the polytetrahedron.[16] The rarity of the octahedron was used to show that the octahedron has higher free energy due primarily to its high symmetry.[16,36] In Chapter 3, we examine 2D ground states of six particles and again find that the most symmetric ground state, the triangle, is rare compared to the other ground states.

The 6-particle ground states in two dimensions have a geometrical nuance: they include a pair of enantiomeric states. The parallelogram and its mirror image shown in Figure 1.5 cannot be rotated to match one another without breaking out of the 2D plane they lie in. The physics we are interested in, such as the free energy and the transition pathways, depends on the cluster's network of nearest-neighbors and not the chirality of the cluster. For this reason, we group pairs of enantiomers together and treat them as a single structure. Pairs of chiral enantiomers also exist in 3D clusters of 7 or more particles.

Clusters from the set of sticky hard-sphere ground states pictured in Figure 1.5 are the reoccurring

test subjects and examples used throughout all the experiments and theoretical derivations described in this thesis.

1.4 Overview

In this chapter, I have presented the underpinnings of Brownian motion of isolated particles and attraction mechanisms that can hold such particles together in dynamic clusters. In Chapters 2 and 3 we investigate the dynamics and equilibrium distributions of the set of clusters shown in Figure 1.5, and in Chapters 4 and 5 we examine equilibrium distributions of 2D clusters containing particles of different masses. Before moving on, I reiterate a key concept. While it is difficult to convey a vivid impression in these static pages, it is important to remember that these clusters are always in flux. They do not simply move towards a permanent global minimum, but instead continuously explore different configurations (it may be instructive to watch the videos of Appendix A). Room-temperature dynamics make soft-condensed-matter systems visually captivating and experimentally rich.

2

Real-Space Studies of the Structure and Dynamics of Self-Assembled Colloidal Clusters

In this chapter I describe experiments on the energetics and assembly pathways of 3D colloidal clusters. The goal of the experiments is to understand processes occuring in the earliest stages of nucleation. It is not yet clear whether the observed dynamics are relevant for small nuclei, which may not have sufficient time to transition between states before other particles or clusters attach to them. However, the measurements do provide some glimpses into how systems containing a small number of particles traverse their free-energy landscape.

2.1 Introduction

A nucleus growing in a bulk fluid must overcome a number of challenges to become a crystal. The most well-known of these is its high surface area-to-volume ratio, which makes it prone to melting or evaporating back into the fluid. Rarely do nuclei grow to the critical size at which they are no longer unstable. A more subtle challenge arises from the structure of the nucleus, which may differ from that of the final crystal. In this case the nucleus must rearrange in order to become a bulk crystallite, and it must do so on a timescale smaller than that at which new particles attach. If the dynamics of rearrangement are slow, as might happen in a deeply quenched system, growth leads to metastable, disordered structures.[37,38]

These challenges illustrate the complex coupling between energetics, structure, and dynamics that makes nucleation a difficult process to study experimentally. Colloidal systems offer several advantages over molecular systems for such studies: the interparticle energies can be controlled using model attractive interactions such as the depletion force; the structure of the suspension can be studied in real-space, at the single-particle level, using optical or confocal microscopy[39,40,41]; and the dynamics can be made slow enough to allow the growth of nuclei to be studied in detail.[42,43] But even in colloids it is difficult to observe the embryonic stages of nucleation, when the nuclei are clusters rather than crystallites, and successful nucleation may hinge on a structural transition. The main source of difficulty is the disparity between the rate of cluster formation and the rate of rearrangement, which can differ by orders of magnitude. This makes it nearly impossible to find a cluster – the formation of which is a rare event that can occur anywhere in the bulk – and simultaneously observe its structural transitions. Furthermore, common 3D microscopy techniques are not fast enough to image the rearrangements of a cluster on timescales short compared to the rotational and translational diffusion time of a nucleus. Thus only the late stages of growth have been investigated in 3D colloidal systems, while the early stages remain elusive.

Here we describe a different approach to addressing these challenges: we study the structure and dynamics of the clusters themselves. To avoid the problem of finding a cluster in the bulk fluid, we localize its assembly in either lithographically-prepared microwells that contain only a small number ($N \approx 10$) of colloidal particles, or we use optical tweezers to collect several particles from a dilute gas phase (Figure 2.1). We also use a fast 3D imaging technique, holographic microscopy, to capture the structural rearrangements of these colloidal clusters on short timescales.

These experiments do not directly probe nucleation, since the clusters are in a state of artificial isolation[36]: they are either walled off from the bulk fluid or placed in a suspension too dilute to favor growth. Nonetheless, the experiments provide information critical to understanding nucleation and growth, such as the rearrangement timescales and probabilities of obtaining clusters with symmetries that differ from the bulk. A previous article[16] by our group examined the energy landscape and equilibrium probabilities for small clusters ($N < 10$) in detail. Here we expand on these results by presenting (a) the chemical techniques required to control the interparticle interactions and assemble colloidal clusters; (b) a new method to image transition states and rearrangement dynamics of clusters in 3D; and (c) data on the structure and dynamics of such systems for different types of depletion interactions. Although much remains to be done to relate this type of data to bulk nucleation experiments, the results show that all three of the aspects fundamental to nucleation – energetics, structure, and dynamics – can be measured in detail through an approach combining synthesis, fabrication, and modern optical techniques.

2.2 Background

The central theoretical concept behind our experimental study is the free-energy landscape, a multidimensional surface characterizing the free energy of a system of N particles as a function of all of their configurational degrees of freedom. Understanding the landscape entails mapping out the minima,

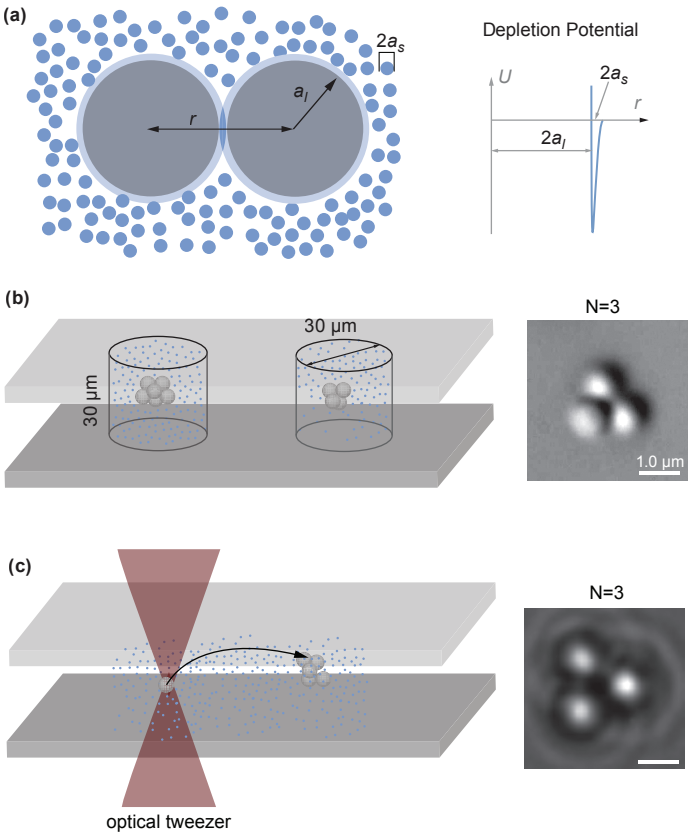

Figure 2.1: Experimental systems. (a) Two large spherical particles feel a mutual attraction when they come within a small-sphere (depletant) diameter of each other. The width of the depletion interaction potential is much smaller than the large sphere size. (b) To self-assemble clusters of spheres, we deposit small volumes of dilute colloidal suspension into microwells. Within 24 hours, clusters form. The image at the right is an optical micrograph (differential interference contrast) of a three particle cluster. (c) A second method of assembling clusters uses an optical tweezer to bring several particles together. Once the desired number of particles is reached, the trap is turned off. The image at the right is an optical micrograph (bright field) of a three particle cluster. Cartoons of clusters in (b) and (c) are not drawn to scale. Micrograph scale bars, 1.0 μm.

which represent stable clusters, and the transition pathways between them. Recent theoretical work has shown that the minima of the landscape can be enumerated exhaustively for a small number of hard spherical particles interacting through a short-range attraction. "Short" means that the width of the potential well is much smaller than the radius of the spheres. This limit permits a geometrical solution to the problem of enumerating the minima: the stable clusters must be rigid, or isostatic, sphere packings where the number of contacts, or "bonds," is at least $3N - 6$. To a first approximation, the potential energy of such clusters is proportional to the total number of bonds. Geometrical solutions have enumerated all possible clusters and their energies up to $N = 13$.[32,33,44,45,46,47,48] A potentially complete set of $N = 14$ clusters has also been enumerated in addition to the lowest energy clusters for $15 \leq N \leq 18$.[47] The transition pathways have been enumerated through a combination of theory and simulation.[49,50]

Creating and observing clusters with such short-range interactions in an experimental system requires careful design. We work with dilute colloids to obtain the clearest possible images of clusters. To favor aggregation in such systems, the attractive interaction between colloidal particles has to be several k_BT deep. At the same time, the binding between colloidal particles has to be reversible. If the particles become stuck together by a strong attractive potential such as the van der Waals interaction, the cluster will not be able to rearrange on experimental timescales.

We therefore use a depletion attraction, the weak entropic interaction introduced in Section 1.2.2, as the driving force to assemble colloidal particles into clusters. In Chapter 1 it was useful to write interaction potentials in terms of the distance between surfaces to compare different types of interactions and different geometries. Here we write the depletion potential in terms of the distance r between the centers of two particles. Figure 2.1a summarizes the depletion attraction: the larger particles experience an effective attraction because the entropy of the smaller spheres, or "depletants," is maximized when the excluded volumes of the larger spheres overlap. The depletion interaction between two large

spheres can be modeled by Asakura-Oosawa theory[5,6]:

$$U_{AO}(r) = -k_B T \frac{\pi}{6} \rho_s (2a_s + 2a_l - r)^2 (2a_s + 2a_l + \frac{r}{2}) \tag{2.1}$$

where r is the center-to-center distance between the two large spheres, a_s and a_l are the radii of small and large spheres, and ρ_s is the number density of small spheres in the solvent. The range of U_{AO} is approximately the diameter of the depletants, $r < 2a_l + 2a_s$; the minimum of a purely depletion potential occurs at contact, $r = 2a_l$:

$$\begin{aligned} U_{AO}(r = 2a_l) &= -(k_B T)\rho_s \frac{\pi (2a_s)^3}{6} \left(1 + \frac{3a_l}{2a_s}\right) \\ &\approx -(k_B T) 2\pi \rho_s a_s^2 a_l \quad \text{when } a_s \ll a_l. \end{aligned} \tag{2.2}$$

According to Equation 2.2, when two types of colloidal particles, 1.0 μm particles ($a_l = 500$ nm) and 100 nm depletants ($a_s = 50$ nm, $\phi_s = \rho_s \pi (2a_s)^3/6 = 20\%$), are mixed together, the attractive potential between large particles has a well depth of about $3k_B T$ at contact and a range of 100 nm. At very small separations, the van der Waals force might cause the large particles to stick irreversibly to one another, but this can be prevented by using particles with an electrostatic double layer. The range of the electrostatic repulsive barrier can be tuned through the salt concentration (Section 1.2.1).

The Asakura-Oosawa model for the depletion potential assumes that the small particles reach equilibrium instantaneously as the large particles move, whereas in reality the depletion potential takes some time to saturate due to the finite diffusivity of the depletants. Using theoretical results from Vliegenthart and van der Schoot,[51] we estimate that for the depletants used in our study the potential saturates on timescales orders of magnitude smaller than the diffusion timescale of the large particles and the observed rearrangement timescales for our clusters (Section 2.4.3). Thus the kinetics of the depletants should not significantly affect the dynamics of the clusters. However, this approximation

may break down for larger depletants or smaller particles.

2.3 Experimental

2.3.1 Colloidal system

Our system consists of negatively-charged polystyrene (PS) microspheres, approximately 1 μm in diameter, and either poly(*N*-Isopropylacrylamide) (PNIPAM) particles or sodium dodecyl sulfate (SDS) micelles as depletants. The sizes of the depletants are chosen so that the range of the depletion attraction is less than 10% of the diameter of the PS particles, so that the attraction is strictly pairwise additive[52]. Whereas the micelles are self-assembled in solution, the PNIPAM particles are synthesized beforehand and added to the suspension. In both systems the depletant scatters negligibly, allowing us to obtain clear images of the clusters through microscopy or scattering. The refractive index of PNIPAM closely matches that of our solvent, water, so the PNIPAM particles are optically transparent in aqueous solution. Furthermore, the strength of the depletion interaction can be easily controlled in both systems simply by modifying the concentration of depletants.

Using PNIPAM spheres allows us to tune the strength and range of the depletion interaction *in situ*. The PNIPAM depletants shrink by 50% in diameter when they are heated above their lower critical solution temperature, around 30 °C. This results in a reduction in the magnitude of the interaction strength by a factor of four, according to Equation 2.2.

We use precipitation polymerization[53,54] to synthesize 80 nm PNIPAM hydrogel particles. The reactor includes a 250 ml three-necked round bottom flask, a magnetic stirrer, a reflux condenser and a nitrogen gas inlet. We dissolve 2.0 g *N*'-Isopropylacrylamide (NIPAM, monomer, 99%, Acros Organics), 0.1 g *N*,*N*'-Methylenebisacrylamide (BIS, crosslinker, 99%, Promega), and 0.18 g ($\approx$ 6 mM) sodium dodecyl sulfate (SDS, 99%, EMD Chemicals) in 93 ml DI water (Milli-Q synthesis grade, Millipore) under gentle stirring. The solution is then heated to 70 °C and bubbled with nitrogen for one

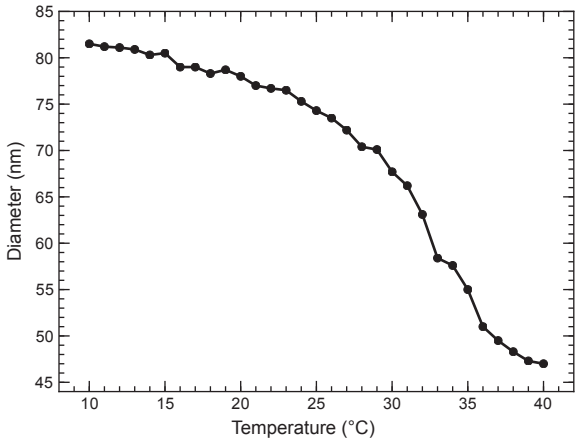

Figure 2.2: Temperature dependence of the diameter of the PNIPAM hydrogel depletants.

hour. To start the polymerization, we inject 40 mg potassium persulfate (KPS, initiator, 99%, Acros Organics) dissolved in 5ml DI water. During the reaction, the solution is stirred with a magnetic stirrer at 300 rpm and bubbled with nitrogen. After four hours, the reaction is stopped by cooling the reactor down to room temperature, and the PNIPAM product is collected. To remove unreacted monomer, initiator, and surfactant molecules from the solution, we dialyze the PNIPAM product against DI water for seven days, exchanging DI water every 24 hours.

The hydrodynamic radius of the PNIPAM particles is 80 nm at 20 °C and 46 nm at 40 °C, with a lower critical solution temperature around 33 °C, as measured by dynamic light scattering (Zetasizer Nano ZS, Malvern Instruments) and shown in Figure 2.2. The polydispersity of the particles is less than 5% at all measured temperatures. The weight concentration of particles in the stock solution is 2.13% w/w, as measured by thermogravimetric analysis (TGA, Q5000IR, TA Instruments).

For the microwell experiments described below, we prepare a suspension of 1.0 μm-diameter sulfate latex PS particles (Batch# 2090,1, Invitrogen Molecular Probes, polydispersity (standard deviation in particle diameter) 3%) and 80 nm PNIPAM hydrogel particles in water. For fluorescence microscopy, we use 1.0 μm sulfate fluorescent latex PS particles (FluoSpheres sulfate microspheres,

1.0 μm, red fluorescent (580/605), Invitrogen, polydispersity 5%). The volume fraction of PS particles is 10^{-5}, and the concentration of PNIPAM is 1.0% w/w (estimated volume fraction $\phi_s \approx 0.25$ at 20 °C). 15 mM NaCl are added to screen the long-ranged electrostatic repulsion between the PS particles. 0.1% w/w Pluronic P123 (BASF) surfactant is also added to stabilize the PS particles in the salt solution. This procedure ensures that the depletion attraction between PS particles induced by PNIPAM can be reversed by either diluting the PNIPAM particles or by increasing the temperature, thereby shrinking the PNIPAM particle size.

For bulk experiments, we load the PS/PNIPAM suspension (with PS volume fraction 4×10^{-3}) directly into sandwiched glass cover slips through capillary action. The cover slips are separated by 40-μm-thick Mylar®A spacers (DuPont Teijin Films) to provide the same thickness across the samples. The edges of the glass cell are sealed with optical glue (NOA-61, Norland Products Inc.) to prevent evaporation.

For the optical-tweezer-assisted assembly method, we prepare a suspension of 1.3 μm-diameter PS particles (Batch #1279,1, Invitrogen Molecular Probes, Surfactant-Free White Sulfate Latex, polydispersity 2.7%), DI water, 5 mM NaCl (EMD, assay (dry basis) 99.0%), and 40 mM SDS (Sigma Aldrich, 99.0%). The volume fraction of PS particles is 10^{-6}, on the order of one particle per 100 μm cube. Because the concentration of SDS is well above the critical micelle concentration, the surfactant molecules assemble into micelles that act as depletants.[40] Following the analysis of Iracki *et al.*,[27] we estimate the width of the SDS induced depletion potential, which includes a factor proportional to the Debye length in addition to the physical size of a micelle, to be approximately 30 nm. In terms of the width of the depletion potential, the effective micelle radius, a_s, is 15 nm. Samples are prepared in cells consisting of a glass slide (25 × 76 mm, VWR) and a No. 1 cover slip (22 × 22 mm, VWR). The slide and cover slip are rinsed with DI water and dried with nitrogen before use. We use UV curing epoxy (NOA-61, Norland Products Inc.) to secure 100-μm-thick strips of Mylar®A (DuPont Teijin Films) as spacers between the slide and cover slip. After using capillary action to fill the sample

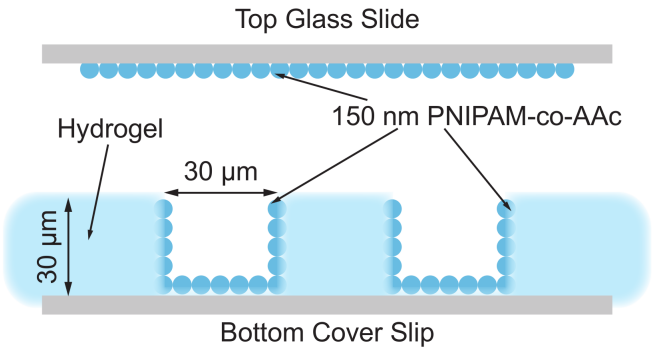

Figure 2.3: Schematic of microwells and glass slides, shown from the side. All surfaces are saturated with 150 nm PNIPAM-*co*-AAc particles (not drawn to scale) to suppress the depletion attraction between the PS particles and the surfaces.

chamber with suspension, we seal the sample cell with epoxy (Devcon 5 Minute Epoxy) to prevent evaporation (Appendix B).

2.3.2 Formation of clusters

We prepare clusters either by letting them self-assemble in lithographically patterned microwells or by bringing particles together in a dilute suspension using an optical tweezer.

Microwell method

Colloidal clusters can be assembled under equilibrium conditions in microwells, as shown in Figure 2.1(b). Since the purpose of the microwells is to isolate a set of particles, and not to confine them, we work at small PS volume fractions such that the volume of each well is 10^5 times the volume of the particles. This ensures that formation of clusters is driven by the attraction between particles rather than by a confinement effect. The solution conditions are the same for every microwell in the plate. Because each plate has tens of thousands of microwells, a single plate yields enough samples to determine ensemble probabilities of cluster structures at small N.

Microwell fabrication. Microwell array plates are fabricated using soft lithography.[55] We use standard photolithography procedures to make a master mold of SU-8 with the microwell pattern on the wafer. We first design a photomask pattern using AutoCAD (Autodesk Inc.). The pattern (20×20 mm) has an array of circles 30 μm in diameter with a pitch of 60 μm on a square lattice. The pattern is printed on a photomask transparency at 20,000 dpi resolution by CAD/Art Services, Inc. We then spin coat SU-8 photoresist (SU-8 3035, MicroChem Corp.) onto a silicon wafer (University Wafer) at 3000 rpm, setting the thickness of the SU-8 layer at 35 μm. The microwells are made by replica molding on the SU-8 master. We prepare a pre-gel solution by dissolving 10% w/w acrylamide (monomer, 99%, Promega), 0.5% w/w *N,N'*-Methylenebisacrylamide (crosslinker, 99%, Promega), 0.5% w/w allylamine (copolymer, 98%, Alfa Aesar) and 0.1% w/w DAROCUR 1173 (photoinitiator, Ciba Specialty Chemicals Inc.) in DI water. The pre-gel solution is poured onto the SU-8 master mold and covered by a silanized cover slip (see below), which later becomes the bottom "window" of the microwell, through which the clusters can be viewed using an inverted microscope. The solution is placed 10 cm from an UV lamp (B-100YP, UVP) for 10 minutes to polymerize the hydrogel. The polymerized microwell plate is carefully separated from the SU-8 master mold, rinsed with DI water, and stored in DI water.

Microwell functionalization. Because the depletion attraction causes particles to stick not only to one another, but also to the walls of the microwells, we attach similar PNIPAM particles to the microwell walls and glass surfaces that bound the wells (Figure 2.3). This matches the roughness of the surface to the scale of the depletants, which has been shown to minimize the depletion interaction between large particles and surfaces.[56] We synthesize a separate batch of poly(*N'*-Isopropylacrylamide-*co*-Acrylic Acid) (PNIPAM-*co*-AAc) hydrogel particles for this purpose. The PNIPAM-*co*-AAc hydrogel particles are synthesized using the same procedure as the 80 nm PNIPAM particles, except that we add 200 mg acrylic acid (99%, Sigma) to the reacting solution. The hydrodynamic diameter of

these PNIPAM-*co*-AAc particles is 150 nm at 20 °C and 60 nm at 40 °C. These particles are attached to the microwell boundaries and glass surfaces using silane chemistry. First the surfaces of the precleaned No. 1 cover slips (24 × 30 mm, VWR) or precleaned glass slides (25 × 75 mm, VWR) are silanized. Cover slips are silanized in 1.0% w/w 3-Methacryloxypropyltrimethoxysilane (98%, Sigma) in anhydrous ethanol solution for 24 hours at room temperature. Glass slides are immersed in 1.0% w/w (3-Aminopropyl)triethoxysilane (98%, Sigma) in anhydrous ethanol solution for 24 hours at room temperature. Then the cover slips and glass slides are rinsed with anhydrous ethanol and blow-dried with compressed dry air. The silanization is completed by leaving the cover slips and glass slides in an oven at 110 °C for one hour.

The cover slips form the bottom windows of the microwell plates, while the glass slides are coated with PNIPAM-*co*-AAc particles and used to cover the tops of the wells. To coat the microwells and silanized slides with particles, we immerse them in a dialyzed colloidal suspension of 150 nm PNIPAM-*co*-AAc particles for 24 hours at room temperature. The amine groups on the surfaces of the glass slide and acrylamide hydrogel microwells slowly bind with the carboxylic acid groups in the PNIPAM-*co*-AAc particles. Afterward the PNIPAM-*co*-AAc hydrogel particles are irreversibly adsorbed onto the surfaces. After this surface treatment, we are able to form 3D colloidal clusters of PS spheres in the middle of the microwells. Without the surface treatment, PS spheres form 2D crystallites on the boundaries of the microwells.

Sample preparation. Once the microwells are prepared and functionalized, we load them with the PS/PNIPAM suspension described in Section 2.3.1. The hydrogel microwell plate and glass slides are first rinsed with about 100 μL PS/PNIPAM suspension at least five times, so that the hydrogel plate has the same ionic and surfactant concentration as the suspension. After the last rinse, the wells are filled with the suspension, and the microwell plate and glass slide are sealed with epoxy (Devcon 5 Minute Epoxy) around the edges of the cover slip. We find that the number of particles per well is

randomly distributed with a mean of about ten. Before putting the sample on the optical microscope for observation and counting, we wait 24 hours for the system to reach equilibrium at 22.0 ± 1.0 °C. Because the hydrogel microwells tend to deform ten days after sample preparation, the observations and data collection are done within seven days of fabrication, and the sample is discarded afterward.

Assisted assembly of clusters by optical tweezers

In the optical tweezer method, we start with a slide of dilute colloidal suspension and assemble a cluster one particle at a time while observing the system with an optical microscope. The microscope is equipped with an optical trap formed by an 830 nm laser (Sanyo DL-8142-201, with Thorlabs TCM1000T temperature controller and LD1255 current controller) focused through a 60X, 1.2 NA Plan Apo water immersion objective (Nikon). To start building a cluster, we bring two PS particles into the optical trap, where they form a depletion bond. Then we add particles one-by-one to the cluster until we reach the desired N, as illustrated in Figure 2.1(c). Starting with individual particles ensures that none of the particles in the clusters are previously bonded or fused irreversibly. Once each particle is attached to the cluster by at least one bond, we turn the optical tweezer off. At this point, the cluster can explore its configurational space, independent of any external potential.

2.3.3 Optical methods for observation

Optical microscopy

We use an inverted optical microscope (Eclipse TE-2000, Nikon Corp.) equipped with 40X dry (NA=0.9) and 100X oil-immersion (NA=1.4) objectives, Nomarski differential interference contrast, and epi-fluorescence to observe the structures of the colloidal clusters in microwells and the bulk phase behavior. A thermally insulated, temperature controlled microscope stage (HSC-60, Instec Inc., with $\pm$0.1 °C temperature stability) controls the temperature of the sample during observation. The im-

ages and videos are recorded by digital cameras (2560×1920, Digital Sight DS-5Mc, Nikon Corp. for still images; and 720 × 720, 40 frames per second, EO-0312C, Edmund Optics for movies) onto a personal computer. For the colloidal clusters, we scan sequentially through the microwells and record videos of clusters in each before analyzing the data.

We resolve the 3D structures of colloidal clusters by scanning through the recorded videos frame by frame. Although the microscope captures a 2D image with narrow depth of field, the rotational motion of the clusters allows us to see all of the particles over time. We map the nearest neighbors for each particle by looking at the 2D image and following it as the structure rotates in 3D space. We then compare this data to the contact matrices or computer renderings of different finite sphere packings identified in theoretical work.[32]

All of the micrographs shown in this chapter have been subjected to linear post-processing (brightness and contrast adjustments) to maximize clarity.

Digital holographic microscopy

To quantitatively image the 3D dynamics of the clusters, we use digital holographic microscopy, a fast 3D imaging technique. Our apparatus consists of a Nikon Eclipse TE2000 inverted microscope modified to use a 660 nm laser (Opnext HL6545MG with Stanford Research Systems LDC501 laser diode current and temperature controller) for illumination, as shown in Figure 2.4a. Two lenses expand and shape the laser beam so that a broad plane wave illuminates the sample as shown in Figure 2.4a and b. The typical laser power is around 50 mW. The light then scatters from a colloidal cluster in the sample cell (Figure 2.4(b)). The interference pattern of the scattered light and transmitted beam is imaged by a 60X, 1.2 NA Plan Apo water immersion objective (Nikon) and magnified by a tube lens before being recorded on a Photon Focus MVD-1024E-160-CL-12 monochrome CMOS camera. In contrast to bright field microscopy techniques, the objective is intentionally defocused so that the focal plane lies 20 to 40 μm downstream of the object of interest. This allows us to better resolve the fringes in

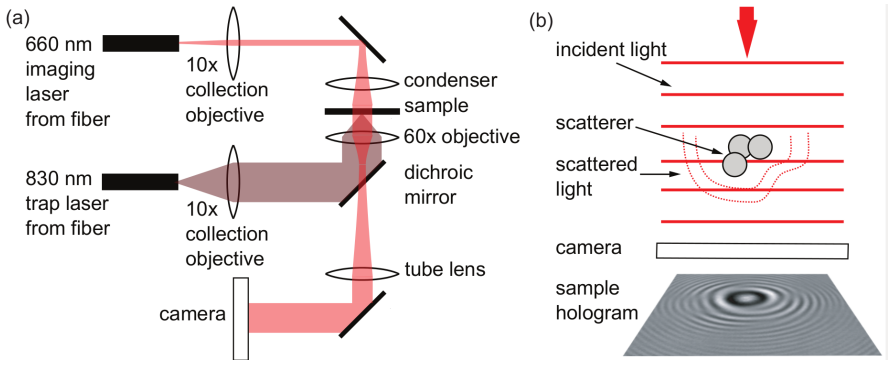

Figure 2.4: Digital holographic microscopy measures the 3D positions of each particle in a cluster. (a) Schematic of apparatus. A 660 nm imaging laser illuminates the sample with a plane wave. A counter-propagating 830 nm laser creates an optical trap which is used to assemble the cluster and is turned off during a dynamical measurement. (b) Diagram of hologram formation. A portion of the incident light scatters from a cluster of particles and interferes with the transmitted beam, producing a hologram that is captured by the camera.

the interference pattern. We record the interference patterns at a rate of 100 frames per second with an exposure time of 15 microseconds for each frame. The images from the camera are sent through CameraLink cable to an EPIX PIXCI E4 frame grabber in a desktop personal computer, where they are recorded to disk.

As illustrated in Figure 2.4(b), each 256×256-pixel interference pattern (or hologram) represents the scattering from all objects in a sample volume of approximately $30\times30\times130\,\mu$m, centered above the objective. To remove the effects of irregularities on the slide or optics, we record a background image with no spheres in the field of view, normalize both it and the hologram images to have a mean value of one, and divide the holograms by the background. The normalization procedure allows us to compare our data to calculated holograms, which we also normalize to one. Background division removes irrelevant features from the data, making the interference fringes clearer.

Once the background is removed, we fit an exact scattering model to the holograms to determine the positions of the particles, following a technique originally developed for single spheres by Ovryn and Izen[57,58] (also implemented by Lee *et al.*[59,60]) and later extended to multiple spheres by Fung *et al.*.[61,62] We use a full multisphere scattering code, SCSMFO, that accounts for interference between

the scattered waves, near-field coupling, and multiple scattering.[63] This allows us to correctly fit clusters with particles separated by less than a wavelength. We fit our data using the open-source software package HoloPy[64] (https://github.com/manoharan-lab/holopy), developed in our research group. HoloPy uses the Levenberg-Marquardt algorithm to minimize the sum of the squared residuals between a recorded hologram and a hologram calculated from the scattering model.

In our procedure, we assume nothing about the cluster geometry; instead, we fit for all $3N$ particle coordinates, plus an intensity scaling factor that accounts for variations in laser power from frame to frame. To reduce the number of free parameters in the fit, we assume a uniform particle size and refractive index. We use the particle diameter given by the manufacturer of the colloids, $1.3\,\mu\text{m}$, and a refractive index of 1.585[65] along with a small but nonzero imaginary part of the refractive index, $0.0001i$, to ensure that the scattering calculations converge. Once we determine the coordinates of all of the spheres by fitting, we classify the geometry of the cluster through 3D visualization or by calculating its second moment.

With $3N+1$ parameters, the minimization problem is computationally complex. The algorithm will not converge to the actual particle positions unless we choose an initial guess for the particle positions that is close to the actual particle locations. We use two methods to generate initial guesses. The most convenient method is to use the particle positions found for the preceding or subsequent frame. This method works well at the high frame rates of our experiments, which ensure that the particles do not move far between frames. But in some cases, such as the first frame of a data series, we must guess the particle positions without any prior information. Thus we use a second method in which we determine approximate particle positions from a numerical reconstruction of a hologram.[66] Although near-field effects prevent reconstructions from providing accurate positions of particles spaced less than a wavelength apart,[67] reconstructing a hologram of a lone cluster still produces an image that resembles a bright field micrograph of the cluster. By reconstructing to various planes within the sample volume, we find a plane in which the particles are approximately in focus. From this image we can

estimate the relative positions and connectivity of particles in the cluster, as described in Section 2.3.3. This procedure generally yields a sufficiently precise initial guess for our fitting algorithm to converge. The resulting coordinates are then used to initialize the fit for the next frame.

To prevent the Levenberg-Marquardt algorithm from getting trapped in local minima, we allow small overlaps between particles. The algorithm either does not converge or converges to poor solutions when we impose a hard no-overlap condition. Instead, we allow the algorithm to place particles in positions that overlap up to 100 nm without any penalty. Allowing slight overlaps likely helps the fitting algorithm avoid local minima that are due to "jammed" states, in which the most direct way for a particle to move to its true position is through another particle. Although the SCSMFO scattering calculations are not strictly defined for overlapping spheres, they nonetheless converge to within our desired numerical accuracy. When the algorithm attempts to place the spheres in positions with greater than 100 nm overlap, we calculate holograms of particles with reduced diameters such that the overlaps are entirely removed. Using holograms that assume the particles are smaller than their true size leads to a larger value of the objective function, effectively penalizing configurations with large overlaps. Allowing overlaps may also compensate for our assumption that the spheres are all exactly the same size.

2.4 Results and Discussion

2.4.1 Interactions

If the interactions between particles are irreversible, kinetics rather than thermodynamics will govern the structures of the clusters that assemble. Because our goal is to understand the statistical mechanics and dynamics of clusters near equilibrium conditions, we first demonstrate that the interactions between clusters are reversible and well-controlled, a necessary prerequisite to further studies.

We first examine the bulk phase behavior of PS particles at a volume fraction of 4×10^{-3} and a

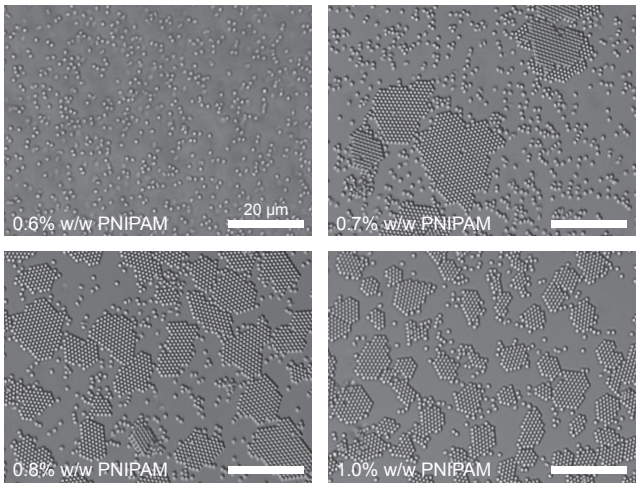

Figure 2.5: Optical micrographs of 1.0 μm PS colloidal particles mixed with varying concentrations of PNIPAM particles (not visible under optical microscopy). All samples are at 20 °C. PS particles form a gas phase at low PNIPAM concentration and a crystalline phase at higher PNIPAM concentration. Scale bar, 20 μm.

constant temperature of 20 °C. At low concentrations of PNIPAM particles, 0.6% w/w and smaller, the PS particles remain dispersed in a gas phase, and no aggregates or crystallites form even after two weeks. As the concentration of PNIPAM increases above 0.7% w/w, we observe quasi-2D crystals forming on the glass substrates, as shown in the optical micrographs in Figure 2.5. The formation of quasi-2D crystals is likely due to the depletion attraction between PS particles and the planar surface, which, unlike our microwell devices, is not treated with a layer of PNIPAM-*co*-AAc particles. When the surface is treated to prevent binding between the PS and the glass, we observe gelation in the bulk at a concentration of 1% w/w PNIPAM. The concentration dependence of the bulk phase behavior confirms that the PS particles attract one another through the depletion forces induced by the PNIPAM particles, and that the interaction can be tuned by changing the concentration of PNIPAM depletants.

At a constant concentration of PNIPAM particles, 0.8% w/w, we find that varying the temperature from 20 to 26 °C causes the crystals to sublimate, as shown in Figure 2.6. The process is reversible: after the sample is cooled to room temperature, the crystals reform. The temperature dependence

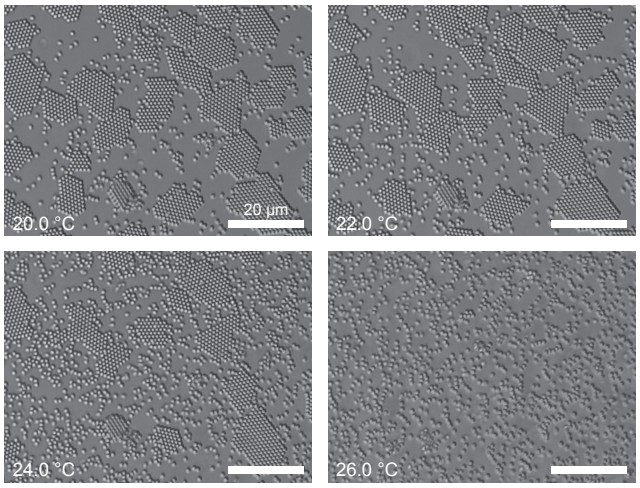

Figure 2.6: Optical micrographs of a mixture of 1.0 µm PS colloidal particles and 80 nm PNIPAM (0.8% w/w) particles at different temperatures. The PS particles form a crystal phase at low temperature and a gas at higher temperature. Scale bar, 20 µm.

is due to the change in depletant diameter on approaching the lower critical solution temperature (LCST) of the PNIPAM polymer. As shown in Equation 2.2, the magnitude of the depletion potential depends quadratically on the size of the depletants, $U \propto a_S^2$ for constant number density ρ_s. Since the PNIPAM hydrogel particles change their sizes from $a_S = 40$ nm at 20 °C to 20 nm at 40 °C, the corresponding depletion potential decreases by about a factor of four over the same range. The quadratic dependence of the depletion potential on the PNIPAM size means that a relatively small change in the depletant diameter can have a large effect on the potential and can easily shift the system out of the gas-solid coexistence regime.

We also observe that the transition temperature increases with the concentration of PNIPAM hydrogel particles, in qualitative agreement with Equation 2.2: higher concentrations of PNIPAM increase the depletion depth, placing the system deeper into the two-phase regime, so that a larger decrease in the depletant diameter is necessary to force sublimation. Similar sublimation behavior has been observed in other systems in which the depletant size varies with temperature[40]. These bulk phase behavior results show that the attraction between PS particles can be controlled over a range of

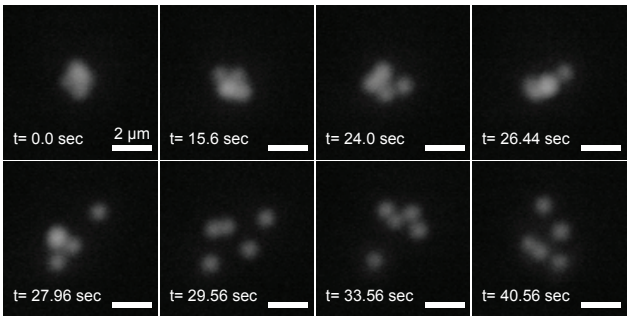

Figure 2.7: Optical video microscopy snapshots of a triangular dipyramidal ($N = 5$) colloidal cluster during a sublimation transition as the temperature increases from 20 °C to 30 °C . Scale bar, $2.0\,\mu$m.

a few k_BT by changing either the concentration of PNIPAM or the temperature.

The key to achieving this kind of reversible interaction is control over the electrostatic repulsion between the PS and PNIPAM particles. At low salt concentrations, 5 mM NaCl, we find that the PS particles remain dispersed as singlets even at 1.4% w/w PNIPAM and 10^{-2} volume fraction PS particles. At high salt concentration, 100 mM NaCl, we observe irreversible aggregation of the PS spheres.

We also confirm that the interactions between PS particles are reversible and well-controlled when they are placed in the microwells, where we use a lower PS volume fraction. We find that at a PNIPAM concentration of 1.0% w/w and a PS volume fraction of 10^{-5}, the PS particles form clusters in the middle of the microwells, with no particles stuck to the walls. As shown in Figure 2.7, the clusters sublimate if the temperature is increased from 25 °C to 30 °C, indicating that the PS particles in the colloidal clusters are not trapped by van der Waals forces.

Forming clusters in the microwells requires a delicate balance of the PNIPAM and PS concentrations. We choose the PS concentration to obtain the desired average number of particles per well, which is set by the microwell dimensions. Because the PS concentration is low, the PNIPAM concentration must be made high enough to overcome the tendency of the system to sublimate. Indeed, if we reduce the PNIPAM concentration slightly, to a value of 0.9% w/w, clusters no longer form. But if

the PNIPAM concentration is too high, the probabilities of formation of particular structures are biased, as shown in Figure 2.8. Here we plot the probability of finding a particular cluster structure, the octahedron ($N = 6$), as a function of PNIPAM concentration. The probability of forming an octahedron decreases systematically with the PNIPAM concentration (note that the error bars, calculated using the Wilson score interval method,[68] represent 95% confidence intervals rather than standard errors on the mean). One possible source of this bias could be the variation in the depletion potential as a function of depletant concentration: a previous study showed a secondary repulsive barrier in the depletion potential at higher depletant concentrations.[69] The other possibility is that the formation probabilities become kinetically dominated at higher PNIPAM concentration, which corresponds to a deeper depletion well. The conditions we ultimately choose – 1.0% w/w PNIPAM, 10^{-5} volume fraction of PS particles, and 15 mM NaCl – manage to satisfy all constraints to ensure equilibrium assembly conditions.

For the dynamics experiments shown in Section 2.4.3, we demonstrate an alternative method of making clusters that works directly in the gas phase and does not require delicately balancing all concentrations. In these experiments we use SDS micelles instead of PNIPAM particles as the depletant, and we assemble clusters using an optical tweezer. We work at very low PS concentration (volume fraction 10^{-6}) and use an SDS concentration that is sufficiently large to induce an attraction, but not large enough to cause phase separation. We test for reversible interactions by building dimers and measuring how long it takes for them to break apart. To check that the bond angles can change, we build small clusters such as bent, two-bond trimers and look for fluctuations in geometry over time. We find that 40 mM SDS and 5 mM NaCl allow us to assemble pairs of particles that remain bound for tens of seconds after the optical tweezer is turned off. This timescale is long enough to observe structural transitions in larger clusters. Under the same conditions the bond angle in a trimer can fluctuate from 180°to 60°, corresponding to a rigid triangle. In contrast, we do not see bonds break in systems with no salt (40-50 mM SDS, 0 mM NaCl) or too much SDS (250 mM SDS, 5 mM NaCl). In such systems,

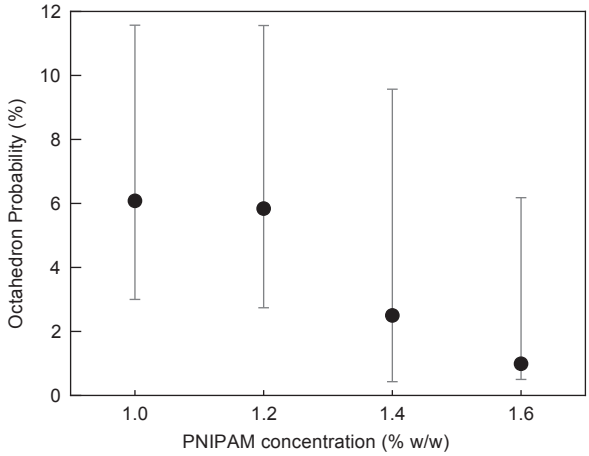

Figure 2.8: Probability of observing a 6-particle octahedral cluster (black circular dots) as a function of PNIPAM depletant concentration. Error bars represent the lower and upper limits of the 95% confidence interval, as determined by the Wilson score interval method.[68]

rigid clusters form and are stable for more than a few minutes.

2.4.2 Structures

Structures of small colloidal clusters

The clusters that assemble in the microwells take on a variety of morphologies, depending on N. In general we find that the number of structures at each N increases rapidly with N for $N > 6$. For each $N < 6$ we observe only one structure. We observe dimers for $N = 2$, triangles for $N = 3$, tetrahedra for $N = 4$, and triangular dipyramids for $N = 5$. Following the convention in Hoy *et al.*[45], we refer to these structures as "Barlow packings," since all of them are subsets of either a face-centered cubic (FCC) or a hexagonally close-packed (HCP) lattice.

At $N = 6$, we observe two structures, an octahedron (point group O_h) and a "polytetrahedron" (point group C_{2v}), which is a triangular dipyramid capped with a third tetrahedron. Optical micrographs and computer renderings in Figure 2.9 show the structure of these two clusters. Whereas the

octahedron is a Barlow packing, the polytetrahedron is incompatible with a close-packed lattice. This is the smallest N at which a non-Barlow packing occurs.

Most of the structures at $N = 7$ are non-Barlow packings. We observe at least five different structures, as shown in Figure 2.9. In one case, we are not able to determine from the optical micrographs whether the symmetry is C_{2v} or D_{5h} (a pentagonal dipyramid). For our 1 μm particles, these two structures differ only in the location of a small gap of approximately 50 nm. Two of the other structures are chiral enantiomers, both of which we observe in the measurements. Of all of these six clusters, only one, the capped octahedron with symmetry group C_{3v}, is a Barlow packing.

At $N = 8$, we observe at least eight different structures; again, in one case we cannot determine the symmetry, which could take on at least six possible point groups (Figure 2.10). All of the six possible structures are variants on the pentagonal dipyramid motif seen at $N = 7$. Only two of the observed structures are Barlow packings, and both of these are derivatives of an octahedron.

All of the structures that we observe in the experiments correspond to mechanically-stable packings of hard spheres with infinitesimally short-ranged attractions. The set of all such structures up to $N = 9$ was enumerated by Arkus and coworkers.[32] This enumeration was later extended to $N = 10$ by both Arkus and coworkers[33] and Hoy and O'Hern[46] and recently to $N = 11$ by Hoy and coworkers.[45] The enumerated packings correspond to the the minima of the potential-energy landscape as a function of N. Interestingly, up to $N = 9$ all of these idealized packings are degenerate: they contain the same number of contacts between spheres and hence the same potential energy. The theoretical packings are shown in the renderings in Figures 2.9 and 2.10.

Three of the possible structures at $N = 8$ are not observed in any of the approximately 1000 microwells we examine. These structures are annotated as "$P_{exp} = 0\%$" in Figure 2.10. One of them, the gyroelongated square dipyramid (point group D_{3d}) corresponds to a Barlow packing. It is also a derivative of an octahedron.

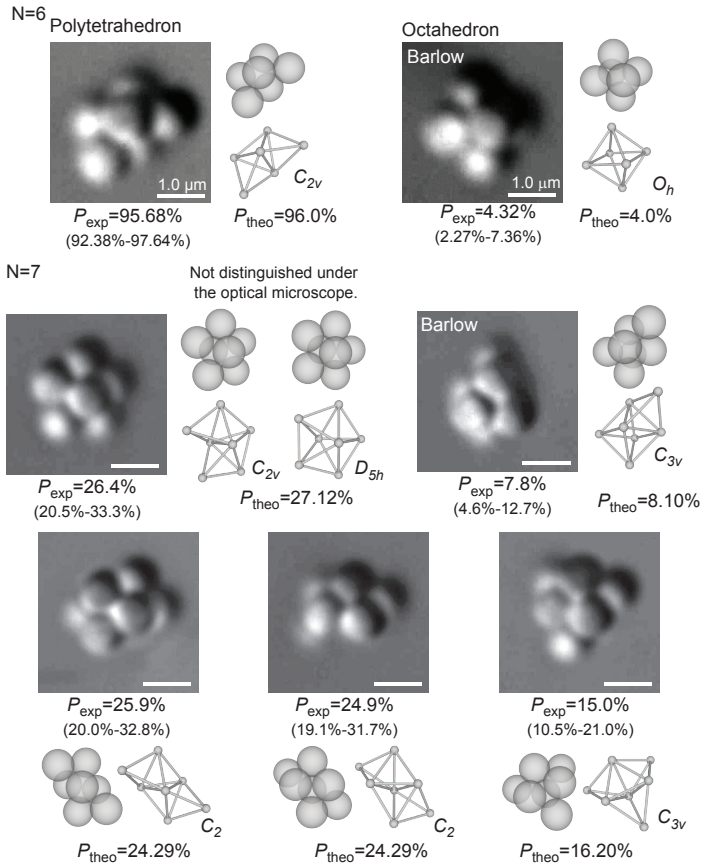

Figure 2.9: Optical micrographs and renderings of colloidal clusters for $N = 6, 7$, with point groups indicated in Schönflies notation. The measured (with the lower and upper limits of the 95% confidence interval determined by the Wilson score interval method[68]) and calculated probabilities are listed below each structure. Annotations above renderings indicate the clusters that cannot be distinguished under bright field microscopy. Structures that are compatible with crystalline lattices are marked with "Barlow". Scale bar, 1.0 μm.

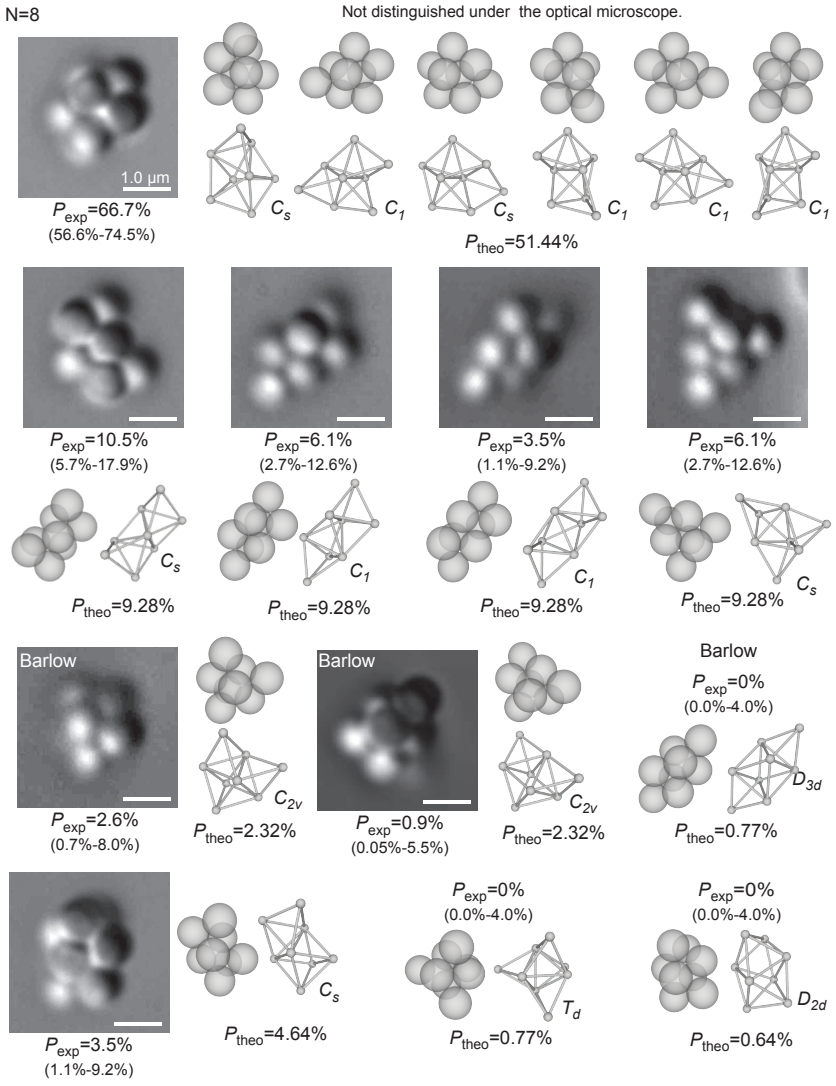

Figure 2.10: Optical micrographs and renderings of colloidal clusters for $N = 8$, with point groups indicated in Schönflies notation. The measured (with the lower and upper limits of the 95% confidence interval determined by the Wilson score interval method [68]) and calculated probabilities are listed below each structure. Annotations above renderings indicate the clusters that cannot be distinguished under bright field microscopy. Structures that are compatible with crystalline lattices are marked with "Barlow". Scale bar, 1.0 μm.

Probabilities and free energies

We measure the free energy of each of the cluster structures simply by counting the number of occurrences of each cluster on the microwell plate. If the clusters are in equilibrium, the distribution of cluster structures should follow the Boltzmann distribution, $F_i \propto -k_B T \ln(P_i)$, where P_i is the probability of observing structure i. For example, at $N = 6$, we observe about 4% octahedra and 96% polytetrahedra, implying that the free energy of a polytetrahedron is about $3k_BT$ lower than that of an octahedron. This difference can be attributed only to entropy, since the two structures have the same number of contacts between particles – or "bonds" – and hence the same potential energy. The measured probabilities for each structure are shown in Figures 2.9 and 2.10. Where it is not possible to determine the particular symmetry group of a cluster from the micrographs, we add together the probabilities of all possible structures.

As we showed in previous work,[16] all the measured probabilities agree well with theoretical calculations for the rotational and vibrational entropies. Both sets of probabilities are shown in Figures 2.9 and 2.10. The dominant contribution to the free energy comes from the rotational entropy: structures with higher rotational symmetry are much less likely to form than less-symmetric structures. This is because the symmetry number of a structure is inversely related to the number of permutations of particles that do not change the structure.[50] Each permutation corresponds to a different pathway to the same structure, and in equilibrium, all such pathways are equally probable.[36] We note that at $N = 8$, the three structures we do not observe have high symmetry, and thus low probability ($P_{theo} < 1.0\%$) of formation.

In terms of nucleation, the most striking feature of the results up to $N = 8$ is the low probability of forming a structure compatible with a close-packed lattice. The total probability of all possible Barlow packings is about 4% for $N = 6$, 8% for $N = 7$, and 5% for $N = 8$. The most likely structures are the least symmetric ones, which in general correspond to packings based on a polytetrahedral

motif.[70] Hoy *et al.*[45] found similar probabilities in their theoretical study.

The situation becomes more complicated when there are more than 9 particles in a cluster: at $N = 9$, clusters with soft modes first appear, and at $N = 10$ clusters with greater than $3N - 6$ bonds can form. These structures, many of which are Barlow packings, occur frequently in the experiments, as shown in Figure 2.11. This result is qualitatively in agreement with theory: vibrational entropy associated with soft modes stabilizes the non-rigid clusters, while the potential energy associated with the extra bond stabilizes the clusters with $3N - 5$ bonds. Quantitative agreement is more difficult to obtain, since an accurate theoretical calculation of the free energy of the non-rigid clusters requires detailed knowledge of the pair potential. This is because the soft modes dominate the vibrational entropy, and the amplitude of these modes depends on the curvature of the potential near its minimum. Since the probabilities of the non-rigid clusters are non-negligible, any error will also affect a calculation of the probability of forming a cluster with extra bonds.

If at larger N there is a similar correlation between Barlow packings and extra bonds or soft modes – as we expect there might be, since structures with extra bonds and soft modes tend to contain both octahedral and tetrahedral subunits,[33] a necessary precondition for an FCC or HCP substructure – then there could be a significant implication for nucleation in similar kinds of short-range attractive systems: the probability of forming a Barlow cluster would depend not only on the potential depth, but also on the curvature of the potential, or its spring constant.

2.4.3 Dynamics

The microwell experiments highlight the low probabilities of forming Barlow packings at low N. Even for $N \geq 9$ the probabilities do not exceed 25%, although, as we have noted, these results may depend on the details of the potential. Connecting these results to nucleation barriers in bulk systems requires understanding the internal dynamics of the clusters. As Crocker noted[36] about Meng *et al.*'s original experiments,[16] our "clusters can equilibrate at leisure in complete isolation, [whereas] the clusters in

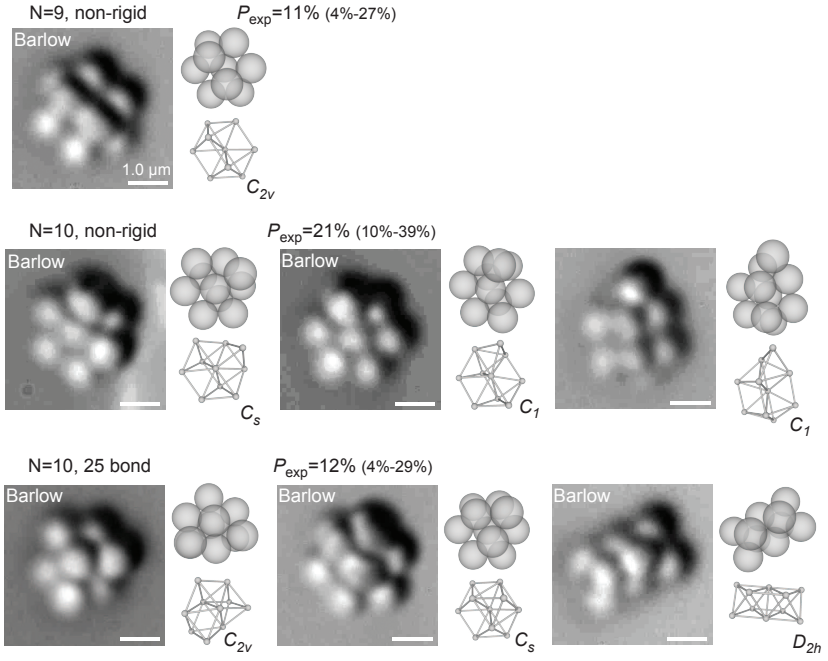

Figure 2.11: Optical micrographs and renderings of special colloidal clusters for $N = 9$ and $N = 10$, with point groups indicated in Schönflies notation. The measured (with the lower and upper limits of the 95% confidence interval determined by the Wilson score interval method [68]) probabilities are listed above the categories. Structures that are compatible with crystalline lattices are marked with "Barlow". Scale bar, 1.0 μm.

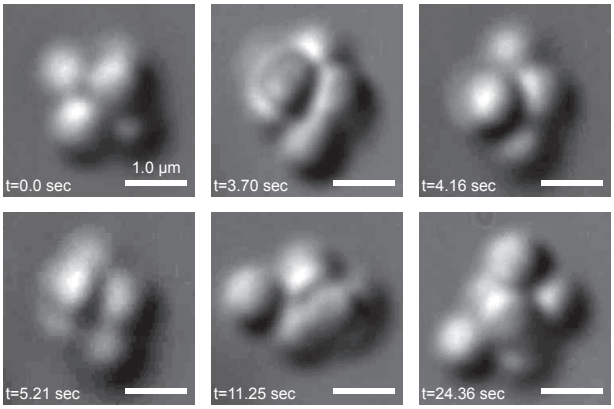

Figure 2.12: A transition between an octahedral and polytetrahedral cluster in a microwell, captured using optical microscopy. Scale bar, 1.0 μm.

an unbounded fluid are continuously bombarded by and grow by absorbing smaller clusters..., all of which may frustrate the equilibration of internal modes." While growth has been well characterized,[71] little is known about the second process, internal equilibration. The rate-limiting step for equilibration is rearrangement between cluster structures, an activated process that requires breaking at least one bond. Here we examine the dynamics of rearrangements in real space.

Dynamics of transitions under bright field microscopy

We find that our clusters can and do transition between different structures after formation. For the PNIPAM system, we find that a six particle cluster changes its structure from a polytetrahedron to an octahedron and back every few minutes to tens of minutes. A typical transition as viewed through optical microscopy is shown in Figure 2.12. The transition itself occurs on a timescale of seconds. We observe similar transitions at larger N.

The short timescale of the transition makes it difficult to determine the structure of the transition state. When a cluster is in an energy minimum, we can infer the relative positions of all the particles because the rotational Brownian motion of the cluster eventually brings all the particles within view.

In contrast, the lifetime of a transition state is significantly shorter than the timescale of rotational motion, so we can only obtain qualitative data on the transition-state structures. For example, the micrographs in Figure 2.12 appear to show that one of the twelve bonds breaks, and a new bond forms between different particles, but we cannot confirm this without quantitative measurements of the 3D positions of all six particles, accurate to 100 nm or better. Further complicating measurements of the dynamics is the long lifetime of the minima relative to that of transition states. Transitions are therefore rare events, and capturing just one of them may require recording tens of thousands of frames.

We therefore use a different experimental technique and, at the same time, modify our system to make it possible to study the dynamics of the clusters. To image the clusters we use holographic microscopy instead of optical microscopy. Holographic techniques can resolve the positions of all the particles in a cluster with at least 100 nm precision and 10 ms temporal resolution. We also change the depletant from PNIPAM particles to SDS micelles, and we assemble clusters directly in the gas phase using an optical tweezer. Although the clusters obtained in this way are thermodynamically unstable after the tweezer is turned off, they survive long enough to allow us to study transitions, as noted in Section 2.4.1. Also, the rate of transitions is higher than in the PNIPAM-microwell system. The reasons for this are not clear, but the simplest explanation may be that the potential well is not as deep. In the microwell system we must use a deep potential well to force the particles to aggregate at low concentration. In experiments where we manually concentrate particles using an optical tweezer, we are free to tune the depletant concentration to optimize the kinetics. SDS micelles are more convenient than PNIPAM particles for this purpose because they are much simpler to make and mix. They also lead to a similar "sticky" depletion potential, in which the range of the attraction is much smaller than the diameter of the PS particles.

Validation of holographic microscopy technique

Because holographic microscopy has not previously been used to study dynamics of clusters larger than two particles, we first show that our fitting method yields realistic and accurate particle positions. Since a hologram is a 2D encoding of a 3D system and not simply a projection, we cannot verify the calculated particle coordinates by overlaying them on top of a real-space image, as one might do in standard particle tracking techniques based on optical microscopy.[21] Instead, we verify the calculated coordinates by numerically comparing measured holograms to ones obtained by fitting a scattering solution to the data ("best-fit holograms"). We also compare numerical reconstructions of the measured and best-fit holograms.

An example of the results obtained from our method is shown in Figure 2.13a for one of the more complicated holograms to fit, one taken of a six-particle cluster that has formed an octahedron. Qualitatively, the data and the hologram calculated from the fit appear identical: the interference rings are in the same locations, and the deviations from circular symmetry are in the same places. Quantitatively, the model fits the data well. The mean of the squared residuals across all pixels, $\chi^2 \approx 4 \times 10^{-4}$, is within a factor of 10 of the noise floor for the measured holograms, 5×10^{-5}. This corresponds to an uncertainty in the particle positions of 30–45 nm in x, y, and z, consistent with previous findings[61].

To further verify the accuracy of the fit, we reconstruct both the measured and best-fit hologram, as shown in Figure 2.13(b). To generate these reconstructions we numerically propagate light through the hologram to the midpoint of the cluster, as determined by the fit. Although the reconstructions do not account for coupling between the scattered fields of the particles, they nonetheless reveal an approximate image of the cluster. The cluster structure and orientation suggested by the reconstructions agree well with those computed from the fit, as shown in Figure 2.13(c).

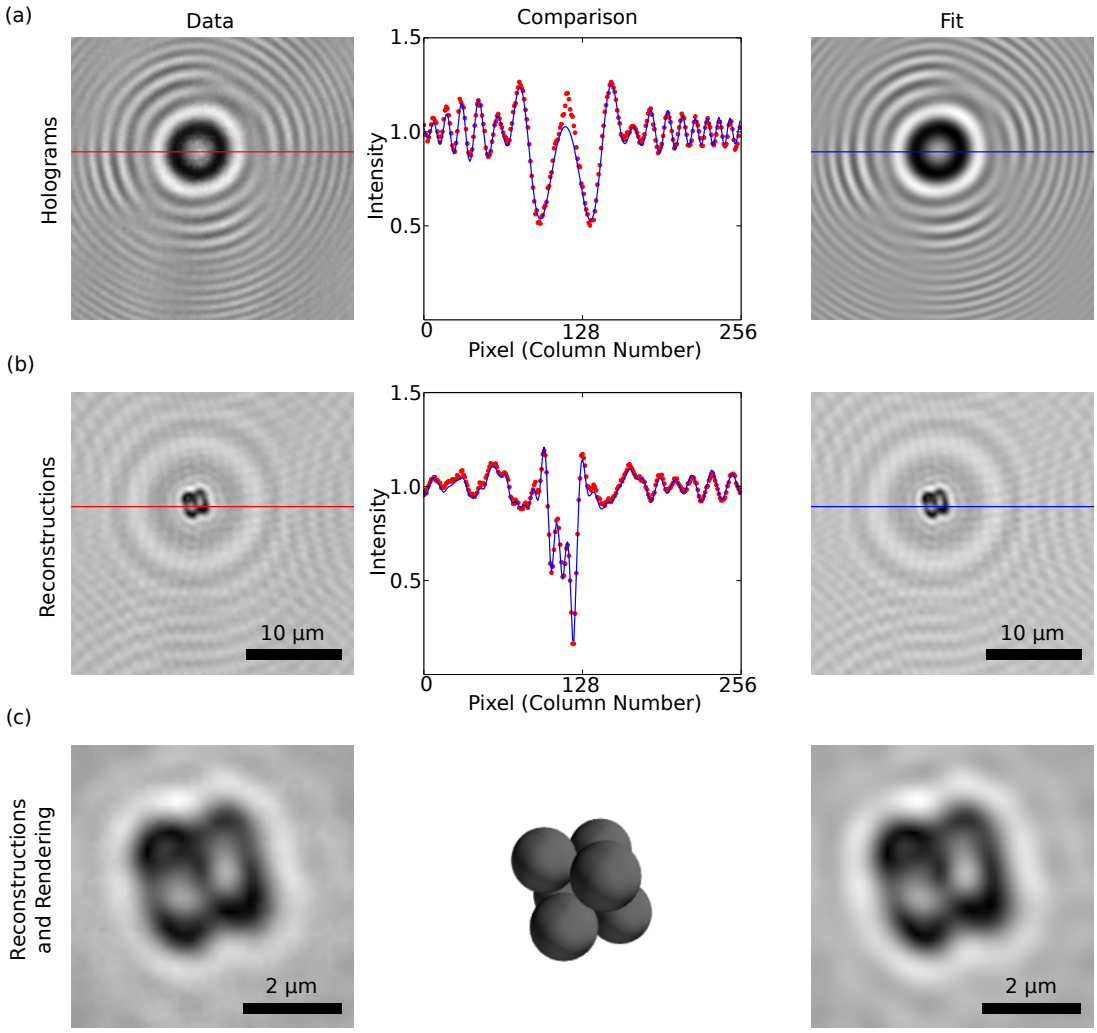

Figure 2.13: Fitting an exact scattering model to holographic microscopy data reveals the locations of all particles in 3D. (a) A frame of raw holographic data for a 6-particle cluster (left) and the hologram calculated from the best-fit positions of the particles (right). Middle plot shows a comparison between the intensities of the two holograms along the linear cross-sections shown in the images. Dotted line corresponds to the measured hologram and solid line to the best-fit hologram. (b) Holographic reconstructions of the raw data (left) and of the best-fit hologram (right), both propagated back 28.5 µm from the plane of the hologram to the cluster's center of mass as given by the fit result. As above, middle plot shows a comparison between intensities of the two images across a linear cross-section. Scale bars, 10 µm. (c) Close-ups of the two reconstructions along with a rendering of the octahedral cluster generated from the fitted particle locations, showing that the fit agrees qualitatively with the reconstructed images. Scale bars, 2 µm. Graphs corrected from print version of manuscript to display intensities along the lines indicated in the holograms instead of intensities along orthogonal vertical lines.

Dynamics of small clusters

Having demonstrated that fitting exact scattering solutions to holograms reveals accurate cluster structures, we now examine the measurements of cluster dynamics obtained from time-series of holograms. We fit for all $3N$ particle coordinates as a function of time, but for simplicity we characterize the cluster structure by an order parameter M_2, the second moment of the mass distribution[72]:

$$M_2 = a_{\text{eff}}^{-2} \sum_{i=1}^{N} |\mathbf{q}_i - \mathbf{q}_0|^2 \tag{2.3}$$

$\mathbf{q}_i$ is the location of the i^{th} sphere, $\mathbf{q}_0$ the center of mass of the cluster, and a_{eff} the effective radius of the particles, or half the distance from the center of one particle, across the depletion zone, to the center of a neighboring particle. We take $a_{\text{eff}} \approx a_l + a_s/2$ and $a_s \approx 15$ nm for an SDS micelle.

The variation in cluster structure with time, as characterized by M_2 and real-space renderings of the cluster coordinates, is shown in Figure 2.14 for 2-, 3-, and 4-particle clusters. Although such clusters have only a single free-energy minimum, as discussed in Section 2.4.2, they show transitions between rigid and non-rigid states as well as rotational and translational Brownian motion. We see a dimer ($N = 2$) break apart, a trimer ($N = 3$) assemble itself into a rigid triangle from a hinge-like excited state, and a tetramer ($N = 4$) transition from a tetrahedron to a planar diamond and back to a tetrahedron. Interestingly, the tetrameric transition is an inversion: labeling the particles shows that the handedness of the tetrahedron changes from the beginning to the end of the measured trajectory (see color renderings in Figure 2.14). Similar types of tetrahedron-diamond-tetrahedron transitions may occur in larger clusters, where they could represent a mechanism for isomerization between different polytetrahedral configurations.

The data show that the lifetime of a non-rigid state mediating a transition is on the order of seconds. To understand this lifetime we estimate the timescale for the tetrahedron-diamond-tetrahedron

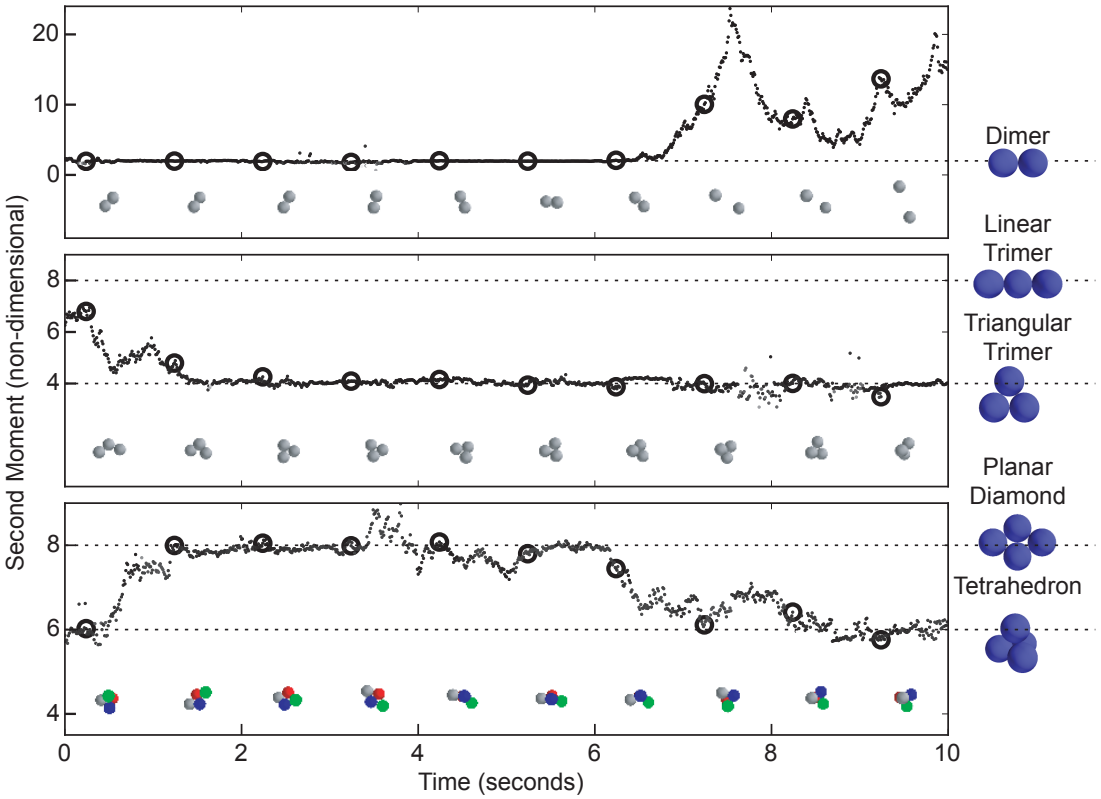

Figure 2.14: Cluster dynamics as determined by holographic microscopy for 2-, 3-, and 4-particle clusters. Plots show the second moment M_2 (Equation 2.3) as a function of time. The intensity of the data points indicates the relative value of the goodness-of-fit parameter χ^2 (black represents the lowest χ^2). Dotted lines show M_2 for the reference geometries at right (dimer = 2, linear trimer = 8, triangle = 4, planar diamond = 8, tetrahedron = 6). Renderings within each plot show the cluster configurations corresponding to the nearest circled data points.

inversion. In this transition, one of the particles must break a bond and traverse an arc length of approximately 220° to flip around to the opposite side of the cluster. Neglecting translations of the center of mass and global rotations, the path length this particle must travel is $\frac{220}{180}\pi\sqrt{3}a_l = 4.3\,\mu\text{m}$, since its center is $\sqrt{3}a_l$ from the rotation axis. Using the diffusion coefficient for a single particle, $D = 3.1 \times 10^{-13}\text{m}^2/\text{s}$, which we measure in a separate experiment by holographically tracking an unbound particle, we estimate that the mean time to complete an inversion is about 10 s,* which is close to the lifetime we observe. The diffusion coefficient may be slightly smaller owing to additional drag from the proximity of other spheres (Chapter 3), which would make the anticipated inversion time longer. For example, reducing the diffusion coefficeint by 30% results in an estimated mean inversion time of around 15 s. The consistency between the calculation and data, along with the fluctuations of M_2 in the excited states (Figure 2.14), shows that the lifetime of the non-rigid state is likely diffusion-limited.

Dynamics of a transition between two free energy minima

As described in Section 2.4.2, a six particle cluster is the smallest cluster that can transition between two rigid energy minima: an octahedron, which is a Barlow packing, and a polytetrahedron, which is not. Using holographic microscopy, we observe a six particle cluster form a polytetrahedron and transition to an octahedron. The results, summarized in Figure 2.15, contain far more detail than can be obtained from the bright field micrographs in Figure 2.12.

The ball-and-stick renderings of Figure 2.15 show the bonds that form and break during the transition. Initially, there are only 10 bonds between the six particles. Four of the particles, shown in gray, are bound in a rigid tetrahedron. Shortly after $t = 2$ s, the particle labeled in blue bonds to the

*To estimate the inversion time, we calculate the mean time to capture for a particle placed randomly between two adsorbing boundaries: $L^2/(12D)$[73] and then double the value to account for the particle moving away from one boundary to a random mid-point and from the random mid-point to the other boundary. We confirm that this is the correct expression with simulations of one-dimensional Brownian motion.

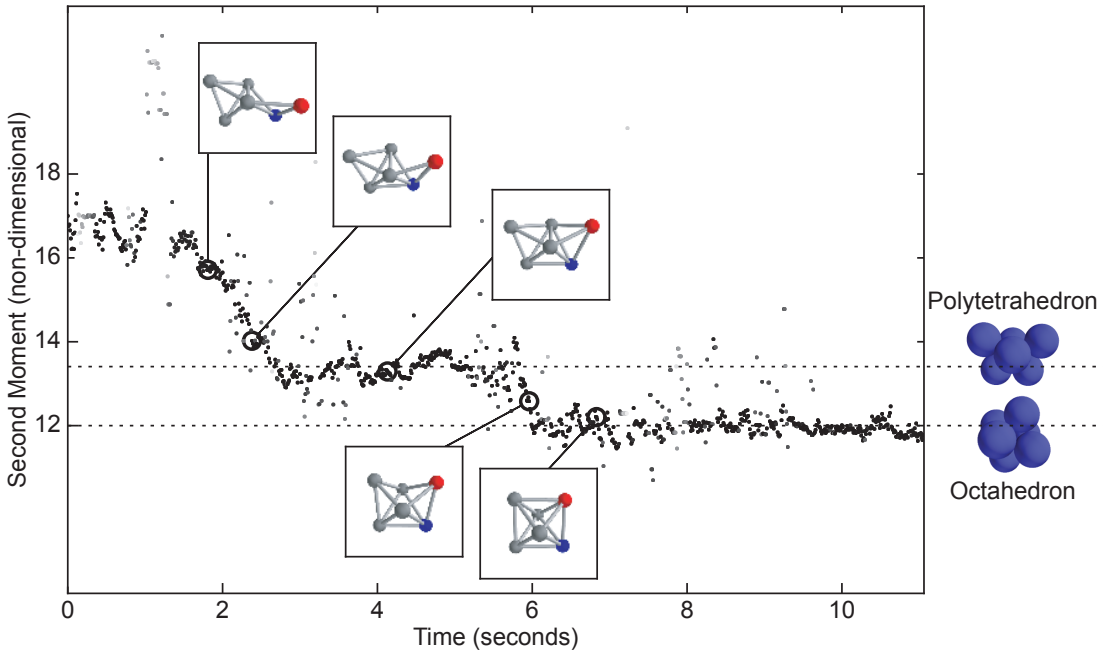

Figure 2.15: Transition from polytetrahedron to octahedron in a 6-particle cluster, as measured by holographic microscopy. Plot shows evolution of the second moment M_2 as a function of time, and ball-and-stick insets show the cluster geometry. The insets are oriented to clearly show the cluster structure and do not represent the actual spatial orientation of the clusters. Dashed lines indicate the second moments of the polytetrahedron ($13\frac{11}{27}$) and the octahedron (12).

tetrahedron to form a trigonal dipyramid. Then an additional particle, shown in red, bonds to the dipyramid to complete the formation of a polytetrahedron at around $t = 3$ s. Just before $t = 6$ s, a bond breaks, and the cluster rapidly transitions to an octahedron, which persists until the end of the data set.

The observed timescale for this transition, which transforms the cluster from a structure inconsistent with crystallinity to a Barlow packing, is close to the timescale expected from single-particle diffusion. This transition requires two particles to move from $3\frac{1}{3}$ radii apart to 2 radii apart. For simplicity, we consider only the time it takes one particle to diffuse a linear distance of $4a_l/3 = 13/30\,\mu$m between two adsorbing boundaries. For a single particle diffusivity between 2 and 3 μm^2/s, this should take approximately 0.5 s, consistent with our observations.

We can estimate the rate of transitions from the observed structure lifetime, which is also on the order of 1 second. We assume that it is equally likely for any of the 12 bonds in the polytetrahedron to break. Only one of these breakages can lead to the formation of an octahedron; the other 11 will result in tetrahedron-diamond-tetrahedron transitions that do not change the structure. Thus we expect that transitions from polytetrahedra to octahedra should in general happen on timescales of tens of seconds; presumably we were fortunate to be able to capture, in our short data set, the breaking of the one bond that would allow an octahedron to form. For comparison we estimate the growth rate as a function of the volume fraction, assuming diffusion-limited conditions. At 10^{-6} volume fraction, new particles arrive at the cluster every hour, at 10^{-4} every few minutes, and at 10^{-2} every few seconds, which is comparable to the time between structural transitions.

The $N = 6$ cluster is the smallest system in which growth can lead to two different outcomes: Barlow packing or polytetrahedral order. A new particle that attaches to an octahedron produces another Barlow packing, while one that attaches to a polytetrahedron produces an $N = 7$ polytetrahedron. At higher volume fractions, when the growth rate is comparable to the transition rate, we might expect that the system has a greater tendency to develop polytetrahedral order, which is incompatible

with crystal nucleation. Given the low free energy of the $N = 6$ polytetrahedron relative to that of the octahedron, the prospects for successful nucleation of a crystal from an $N = 6$ embryo seem bleak. However, at higher volume fraction the initial clusters that form may be much larger than six particles, so the $N = 6$ case may not in general represent a nucleation "bottleneck." Further studies of transitions in larger systems, where extra bonds and soft modes are possible, are necessary to more rigorously relate the cluster dynamics to nucleation probabilities.

2.5 Conclusions

The work we have shown here represents the first steps toward understanding nucleation through analysis of the thermodynamics and dynamics of colloidal clusters. Much remains to be done on both the experimental and theoretical fronts, particularly for larger clusters. Also, although we have measured transition rates for a few small clusters, we need much more data on both small and large clusters to obtain statistically significant estimates of the transition state lifetimes and transition pathways, which are the key elements missing from the free-energy landscape model of short-range attractive spheres.[16,50] † Such studies require consideration of the interaction potential: as we have shown, the rearrangement timescales for systems with different depletants can vary by orders of magnitude, presumably because of differences in the well depth and width; also, the probabilities of obtaining clusters with soft modes, many of which are Barlow packings, depend on the curvature of the potential and not just the well depth. Rather than measure these features directly, which requries resolving the separation between two colloidal particles to nanometer-scale precision,[61,10] we show in Chapter 3 an alternative route to measure the impact of the interaction potential through a "sticky parameter."[49]

Although the connection to nucleation barriers remains tenuous at this stage, our work demonstrates that the study of colloidal clusters stands to reveal new insights into processes that are key to

† Recent experiments on 2D clusters provide these measurements (Chapter 3).

understanding nucleation, including the formation of clusters and their structural transitions. Modern experimental techniques such as soft lithography and holographic microscopy make it possible to measure all the thermodynamic and dynamical information about a cluster, including its structure, free energy, and fluctuations about free-energy minima. We know of no other experimental system that can be probed in such detail. The main goal for future experiments is to systematically explore the dynamics as a function of N and to obtain, from that wealth of detail, a more complete model of the free-energy landscape that governs nucleation.

Acknowledgements

We thank Jesse Collins, Miranda Holmes-Cerfon, Zorana Zeravcic, Natalie Arkus, Michael Brenner, and Robert Hoy for helpful discussions. Rebecca W. Perry and Thomas G. Dimiduk acknowledge the support of National Science Foundation (NSF) Graduate Research Fellowships. This work was funded by the NSF through CAREER grant no. CBET-0747625 and through the Harvard MRSEC, grant no. DMR-0820484. Computations were performed on the Odyssey cluster, managed by the Harvard FAS Sciences Division Research Computing Group. Microwell device fabrication was performed in part at the Center for Nanoscale Systems (CNS), a member of the National Nanotechnology Infrastructure Network (NNIN), which is supported by the NSF under award no. ECS-0335765. CNS is part of Harvard University.

3

2D Clusters of Colloidal Spheres: Ground States, Excited States, and Structural Rearrangements

In this chapter, we study experimentally what is arguably the simplest yet non-trivial colloidal system: two-dimensional clusters of six spherical particles bound by depletion interactions. These clusters have multiple, degenerate ground states whose equilibrium distribution is determined by entropic factors, principally the symmetry. We observe the equilibrium rearrangements between ground states as well as all of the low-lying excited states. In contrast to the ground states, the excited states have soft

Reprinted manuscript with permission from R. W. Perry, M. C. Holmes-Cerfon, M. P. Brenner, and V. N. Manoharan, *Phys. Rev. Lett.*, (in press) (2015).

modes and low symmetry, and their occupation probabilities depend on the size of the configuration space reached through internal degrees of freedom, as well as a single "sticky parameter" encapsulating the depth and curvature of the potential. Using a geometrical model that accounts for the entropy of the soft modes and the diffusion rates along them, we accurately reproduce the measured rearrangement rates. The success of this model, which requires no fitting parameters or measurements of the potential, shows that the free-energy landscape of colloidal systems and the dynamics it governs can be understood geometrically.

3.1 Introduction

Colloidal clusters containing a few particles bound together by weak attractive interactions are among the simplest, non-trivial systems for investigating collective phenomena in condensed matter. Such clusters can equilibrate on experimental timescales and display complex dynamics, yet are small enough that the ground states can be enumerated theoretically, and the positions and motions of all the particles can be measured experimentally. Theoretical and experimental work on isolated 3D colloidal clusters of monodisperse particles has shown how the number of ground states changes with the number of particles N [32,33,46,45,47,48] and how the free energies of the rigid states are related to entropy-reducing symmetry effects and entropy-enhancing vibrational modes.[16,44,50]. The importance of entropy in colloidal clusters stands in stark contrast to the case of atomic clusters, where potential energy effects dominate. The entropically-favored clusters are important clues to understanding nucleation barriers in bulk colloidal fluids [36,45] and the local structure of gels. [38]

However, the excited states and structural rearrangements in such clusters have not yet been studied experimentally. In bulk materials, local structural rearrangements are important to a variety of dynamical phenomena, including the glass transition, [74] aging, [75,76] epitaxial growth, [24] and the jamming transition.[77] A better understanding of the internal dynamics in colloidal clusters could reveal local

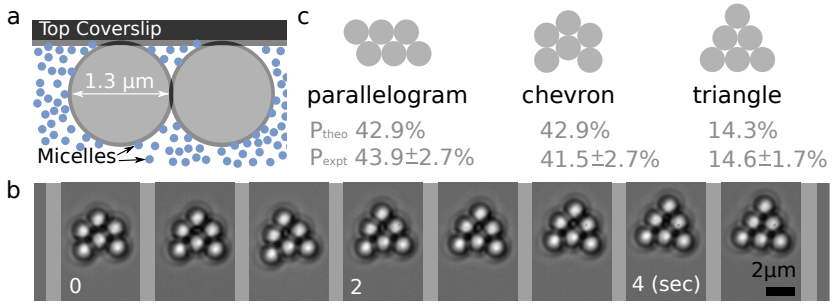

Figure 3.1: (a) SDS micelles induce a short-range depletion attraction between polystyrene microspheres and between the microspheres and the nearby glass coverslip. (b) Time-lapse images demonstrate a transition. (c) The three rigid ground states and their theoretical and experimental probabilities with 95% confidence intervals (Appendix C) (the probabilities for the parallelogram include both chiral enantiomers).

mechanisms underpinning these bulk phenomena. Only a few experimental studies have explored internal dynamics in colloidal clusters: Perry and coworkers examined transitions between two states of a 3D 6-particle cluster of spherical particles;[17] Yunker and coworkers studied relations between the vibrational mode structure and the contact network in disordered, 2D clusters of polydisperse particles as a function of N[78,79]; and Chen and coworkers examined the interconversion and aggregation pathways in clusters of particles with directional attractions.[14] As yet, however, a quantitative understanding of the rearrangement rates and the pathways through the excited states remains challenging. Transition-state models,[80,81,82,34] which relate dynamics to the heights of saddle points on the energy landscape, are not easily applied to colloids because the fluid surrounding the particles damps and hydrodynamically couples their motions, and the short-ranged interactions typical of colloidal particles are not easily measured, making the topography of the landscape difficult to accurately compute. Indeed, as we shall show, the excited state occupation probabilities and the transition rates are sensitive to fine details of the potential, which are not easily measured.

We study experimentally the excited states and rearrangement rates in perhaps the simplest type of colloidal cluster: isostatic arrangements of equal-sized, spherical colloidal particles, constrained to lie on a plane and held together by well-controlled, short-range attractions a few times the thermal en-

ergy k_BT in depth (Figure 3.1a). Because the clusters are isostatic, all excited states have zero-frequency modes, or soft modes, in their vibrational spectra (Figure 3.1b and Section A.0.4). By tracking the particles over long times, we quantify the equilibrium probability of each excited state and the motions of the particles within each soft mode. Surprisingly, the dynamics that emerge from this landscape can be quantitatively described by a simple geometric model involving only two parameters, a "sticky parameter" that characterizes both the depth and curvature of the attraction, and a diffusion coefficient, which we find to be insensitive to the mode. Both parameters can be easily measured. Therefore, no detailed knowledge of the interactions or hydrodynamics is required to reproduce the rates of rearrangement between ground states.

3.2 Experimental Methods

To make clusters, we first load an aqueous suspension of 1.3 μm-diameter sulfate polystyrene microspheres into a cell made from two plasma-cleaned glass coverslips separated by 35 μm DuPont Mylar® A spacers (Appendix B). The only additional component in the suspension is sodium dodecyl sulfate (SDS), a surfactant that forms negatively charged micelles in solution. The micelles create a weak depletion interaction[5,6,27] between the particles and a stronger depletion interaction between the particles and coverslip,[29,83] as illustrated in Figure 3.1a. At 33.4 mM SDS, we observe that 2D clusters bound to a coverslip frequently transition between states but rarely split apart or merge (Section A.0.5). At this concentration, the sodium counterions from the surfactant reduce the Debye length to 2.85 nm, setting the effective hard-sphere depletion range of the micelles to 30 nm, just 2.3% of the particle diameter.[26,27] As a result, the electrostatic and depletion interactions between the particles are short-ranged. There is likely also a short-range van der Waals attraction, which we estimate tapers off to k_BT when the particle surfaces are 145 nm apart.[25]

At the beginning of the experiment, we assemble clusters at the top of the sample cell using optical

tweezers. We then turn off the tweezers and record digital micrographs for the remainder of the experiment. The clusters, which would normally sediment, remain at the underside of the upper coverslip, confirming the depletion attraction. We use particle tracking algorithms to locate the particles,[21] link the locations into trajectories through time, and automatically identify the cluster configurations.

To collect images, we use a Nikon Eclipse TI-E inverted microscope with a Photon Focus camera, a CameraLink cable, and an Epix frame grabber connected to a desktop PC. We use a combination of a 60X water immersion objective (Nikon CFI Plan Apo VC, NA 1.2) and a 1.5X tube lens. We choose a slow frame rate of 3 frames per second to efficiently capture many transitions while still collecting a few frames during each transition. This frame rate is high enough to allow particle tracking as described below.

By establishing four clusters of six particles in the field of view ($59\,\mu\text{m} \times 59\,\mu\text{m}$), we can theoretically capture four hours of cluster data from a typical one hour experiment. In reality, 10 of our 44 clusters produced data for the entire duration of the data acquisition. The data series from the other 34 clusters were truncated during post-processing for one of four reasons: the cluster diffused to the edge of the frame (7 of 44); a particle permanently broke away from the cluster (7 of 44); the cluster came less than one particle diameter from merging with another cluster (7 of 44); or the particle locating or tracking algorithm failed because, for example, the optical system drifted out of focus (13 of 44). From 10.2 hours of raw video, we were able to obtain 25.6 hours of 6-particle cluster time series out of a theoretical maximum of 40.7 hours, a 63% recovery rate. While we do lose track of many of our clusters over time, this approach to data acquisition requires little supervision and produces twice as much usable data per hour as compared to watching over and tending to a single cluster.

Our post-processing routines are written in Python using the SciPy ecosystem.[84] We locate the particles, identify the clusters they belong to, and track the particles from frame to frame. To locate the particles, we first divide each image by a background image captured with no particles in the field of view to remove static artifacts. We then use the Crocker and Grier centroiding method[21] to locate

the particles with better than 20 nm precision, as determined by tracking single particles diffusing in two dimensions at 500 frames per second, and then measuring the deviation from linearity of the mean-square displacements at the smallest lag times. After locating each of the particles, we identify the cluster that each particle belongs to by computing the distance to the four clusters' centers in the preceding frame and selecting the cluster with the shortest distance. We then subtract off the cluster's center of mass from each of the particle locations before linking them into trajectories using the proximity between locations in consecutive images. Subtracting off the cluster center of mass reduces the apparent distance moved by the particles between frames by removing rigid-body translations. For our close-packed particles that occasionally diffuse distances greater than a full particle radius between frames, subtracting off the cluster center of mass prevents multiple particles from being linked to a single particle in the next frame. Alternative approaches to tracking a collection of close-packed particles include the optimization scheme of Crocker and Grier[21] and using strict proximity at a sufficiently high frame rate, where diffusing more than a particle radius between frames is extremely unlikely.

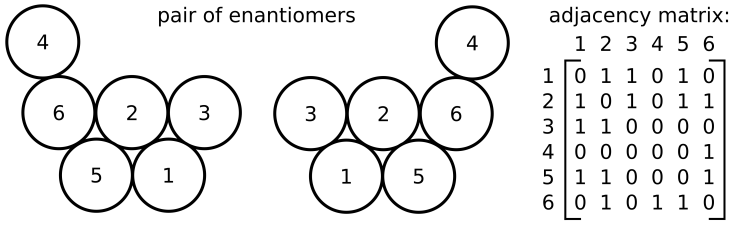

Figure 3.2: An adjacency matrix is a graph-theoretical representation of the connectivity of a cluster. Each element in the matrix relates a pair of particles identified by the row number and column number; a value of 1 signifies bound, and 0 signifies unbound. The adjacency matrix does not distinguish between chiral enantiomers such as the pair of 8-bond excited state shown here with their adjacency matrix.

Once all the particles are found, assigned to clusters, and tracked, we determine the configuration of each cluster in each frame by computing the cluster's adjacency matrix[33] (Figure 3.2). The adjacency matrix determines the cluster configuration, including the particular permutation of particles, from our library of configurations with 9-bonds, 8-bonds, 7-bonds, and "other" for clusters with

fewer bonds. Such adjacency matrices do not distinguish between chiral enantiomers, which we pair together as single configurations. To determine when particles are bound or unbound, we set a cutoff distance of $1.4\,\mu$m, which is determined from the histogram in Figure 3.3. We find that the occupation probabilities are insensitive to the choice of cutoff distance.

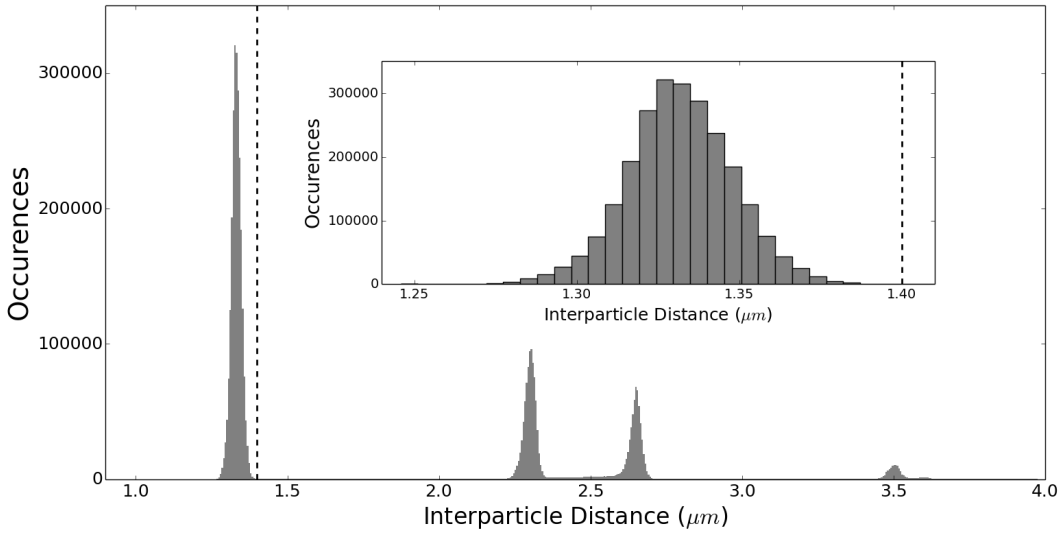

Figure 3.3: Distances between all particles within all 6-particle clusters at all times. The first peak (shown in inset) represents bound particles at distance $d_0 \approx 1.33\,\mu$m. The other peaks are at $\sqrt{3}d_0$, $2d_0$, and $\sqrt{7}d_0$ as expected for close-packed spheres on a plane. The width of the peaks comes from a combination of the particle polydispersity, the width of the interaction potential, and the precision of the particle locating algorithm.

3.3 Results

We focus on 6-particle clusters because this is the smallest system with multiple ground states (Section 1.3). Because these clusters are bound by short-range interactions, the potential energy is proportional to the number of contacts or "bonds" between particles. The 6-particle clusters adopt three ground states with nine bonds each (Figure 3.1c): the parallelogram (which has two enantiomers), chevron, and triangle. In aggregate, the clusters occupy the parallelogram and chevron states for equal

Table 3.1: Comparison of the components factoring into the probabilities of the three ground states for 2D clusters of six particles. I_s is the moment of inertia about an axis running through the cluster's center of mass and perpendicular to the plane of the cluster, χ_s is the chirality, σ_s is the symmetry number. These three components determine the rotational partition function, $Q_{rot,s} = \chi_s\sqrt{I_s}/\sigma_s$. The vibrational partition function, $Q_{vib,s}$ is calculated from the normal mode frequencies. More explaination is provided in Chapter 4.

	Parallelogram	Chevron	Triangle
$\sqrt{I_s}$	$\sqrt{5\frac{1}{2}}$	$\sqrt{4\frac{5}{6}}$	$\sqrt{5}$
χ_s	2	1	1
σ_s	2	1	3
$Q_{rot,s}$	$\sqrt{5\frac{1}{2}}$	$\sqrt{4\frac{5}{6}}$	$\frac{1}{3}\sqrt{5}$
$Q_{vib,s}$	$\frac{8}{27}\sqrt{\frac{2}{11}}$	$\frac{8}{27}\sqrt{\frac{6}{29}}$	$\frac{8}{27}\sqrt{\frac{1}{5}}$
Probability	$\frac{3}{7}$	$\frac{3}{7}$	$\frac{1}{7}$

amounts of time but spend only one third as much time in the triangle state (Figure 3.1c). The measured occupation probabilities agree with the expectation for a statistical mechanics ensemble in equilibrium. To calculate the probabilities, we assume that the translational, rotational, and vibrational degrees of freedom are independent, the vibrational modes are harmonic, and the translational contributions and potential energy differ negligibly among the 3 states (Chapter 4). As seen previously in 3D clusters, the differences in occupation probabilities are primarily due to symmetry, which enters into the rotational contribution (Table 3.1).[16,36]

The excited states of the system have more complex and interesting structures. All of them have zero-frequency modes. The modes we see at the 8-bond energy level have either hinge-like joints or diamond-square-diamond[85] flexibility (Figure 3.4). Although the 7-bond energy level has twice as many states, nearly all of the zero-frequency modes are simply combinations of these two types of motion (Figure 3.4). The exceptions are a state with a flexible ring of five spheres and a state with a single sphere detached from the cluster. We do not include this disconnected state in our 7-bond probability calculations because it is not a true 6-sphere cluster.

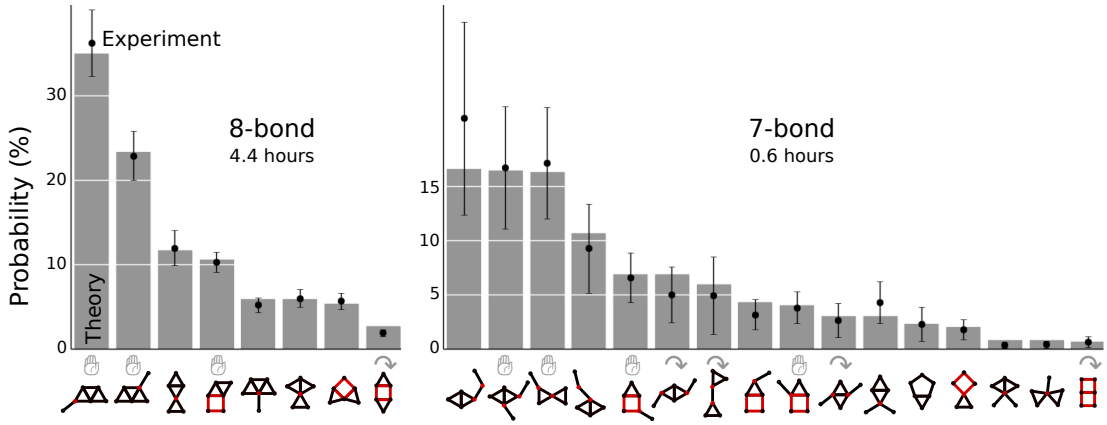

Figure 3.4: Theoretical (bars) and experimental (points) probability distributions of the 8- and 7-bond excited states. Each bar-point pair is labeled by a connectivity diagram of the excited state, with hinge-like joints and non-rigid squares labeled in red. Hand symbols mark the chiral states, and curved arrows mark the states with 2-fold rotational symmetry (in 2D the only accessible symmetry axis is perpendicular to the plane of confinement). The total observation time is 25.6 hours; for comparison, the clusters spend 19.5 hours in the 9-bond states. Error bars represent 95% confidence intervals (Appendix C).

The fraction of time the clusters spend in the excited energy levels depends on the surfactant concentration. At a concentration of 33.4 mM SDS, the clusters spend 95.5% of the time in states with 7 or more bonds. Of this time, 79.6% is spent in ground states, 18.0% in 8-bond excited states, and 2.4% in 7-bond excited states. As we decrease the surfactant concentration, the distribution shifts toward the excited energy levels. Qualitatively, this shift makes sense, since decreasing surfactant concentration corresponds to decreasing depletion strength. To understand the energy level occupation probabilities quantitatively, we must consider the entropy of the soft modes. We return to this point later.

Despite the wide variety of structures in the excited states, few have any symmetry. Surprisingly, the few symmetric states do not occur as infrequently as we might expect, given the dominant role symmetry—more specifically, permutational entropy[16,86]—plays in the probabilities of 6-sphere ground states in both 2D and 3D. Furthermore, the asymmetric states have a highly non-uniform distribution that is only partially explained by the increased probability of states that are pairs of chiral

Table 3.2: Structural rearrangement rates between each of the ground states: (P)arallelogram, (C)hevron, and (T)riangle. In total, we observed 820 transitions in 25.6 hours of data from 44 clusters. Measured values used in postfactor: $D = 0.065\,\mu\text{m}^2/\text{s}$ ($234\,\mu\text{m}^2/\text{h}$), $\kappa = 30.5$ and $d = 1.3\,\mu\text{m}$.

		Theory							Experiment		
		(nondimensional)				(per hour)			(per hour)		
		end state									
start state		P	C	T		P	C	T	P	C	T
	P	1.17	1.43	0.67		5.3	6.5	3.0	4.4	5.5	2.5
	C	1.43	2.31	0.56	$\times \frac{D}{\kappa d^2} =$	6.5	10.5	2.5	5.4	7.7	1.9
	T	0.67	0.56	0		3.0	2.5	0.00	2.5	2.2	0.04

enantiomers (Figure 3.4). These observations suggest that the variation in probabilities arises from entropic factors other than the permutational contribution.

We also measure the rate of rearrangements between ground states and find that the matrix of rearrangements per unit time is symmetric (Table 3.2), as expected in equilibrium. Most of these rearrangements involve a single bond breaking, followed by the cluster diffusing along the soft mode in its excited state and finally forming a new bond to arrive at a ground state (Figure 3.5).

3.4 Analysis

Understanding the excited state probabilities and rearrangement rates requires us to consider the entropy of the soft modes and the dynamics along the resulting free-energy landscape. In contrast to typical molecular-scale transitions, in which the potential energy varies along the entire reaction coordinate, our clusters first break out of a narrow attractive well and then freely diffuse in soft modes at constant potential energy under only an entropic driving force. We therefore expect the transition rates to depend on the entropy along the modes, the hydrodynamic drag, and the distance to diffuse in the soft modes.

To calculate the entropy, we use the geometrical model of Holmes-Cerfon, Gortler, and Brenner.[49] In this model, the potential energy landscape is represented as a collection of manifolds, each at

constant potential energy. The dimension of each manifold equals the number of internal degrees of freedom of the cluster: for example, the ground states are 0-dimensional manifolds (points), and the 8-bond states live on 1-dimensional manifolds (lines). To compute the partition function, we numerically parametrize each manifold and integrate the vibrational and rotational entropies over its entire volume. This calculation of the entropy is purely geometrical and requires no knowledge of the actual pair potential; the only assumption is that the harmonic vibrational degrees of freedom equilibrate quickly compared to motion along the soft modes.

The model reproduces our experimental measurements of the excited state probabilities within experimental error (Figure 3.4). The agreement validates the model's assumption and shows that for the excited states, the entropy associated with the soft modes dominates the permutational entropy associated with asymmetry. In particular, the entropy of the zero-frequency modes explains the surprisingly high probability of 7-bond structures with 2-fold symmetry.

To understand the relative populations of the excited-state energy levels (8-bond versus 7-bond), we must consider the interparticle potential. Measuring the potential well is difficult because the interaction is short-ranged—only a few tens of nanometers for the depletion component[27] and similarly ranged for the electrostatic and van der Waals contributions. However, the short range makes it possible to use a "sticky sphere" approximation, in which a single parameter κ, called the "sticky parameter," characterizes the interaction. κ is the partition function for a single bond and as such is proportional to the amount of time two particles are bound versus separated. In the limit where the potential becomes both infinitely narrow and infinitely deep,[49]

$$\kappa = \frac{e^{-\beta U_0}}{d\sqrt{\frac{2}{\pi}\beta U_0''}} \tag{3.1}$$

where $\beta = \frac{1}{k_B T}$, U_0 is the depth of the potential well, d is the microsphere diameter, and U_0'' is the curvature at the potential minimum. The advantage of this approximation is that we need only

measure κ, and not the full potential.

3.4.1 Measuring the sticky parameter

We measure κ from ratios of occupation probabilities of ground and excited energy levels. The total time t_n for which a cluster has n bonds is proportional to $Q_n \kappa^n$, where Q_n is the sum of the partition functions of the n-bond manifolds. By taking ratios of the time spent at different energy levels and calculating the Q_n we obtain a measurement of the sticky parameter as $\kappa = \frac{t_{n+1}}{t_n} \frac{Q_n}{Q_{n+1}}$.

To compute the sticky parameter using this approach, we need to know the total geometrical partition function, Q_n, for manifolds with n bonds, for at least two different values of n. The "geometrical" partition function is the part which comes from integrating the rotational and vibrational partition functions; this is geometrical because it depends only on the locations, shapes, and sizes of the particles, and not on the potential energy or temperature.

The total geometrical partition function is

$$Q_n = \sum_i z_i^{(n)}, \tag{3.2}$$

where $z_i^{(n)}$ is the geometrical partition function for a single manifold with n bonds, and the index i runs over all manifolds with n bonds. The geometrical partition function for a single manifold $\Omega_i^{(n)}$ is

$$z_i^{(n)} = \int_{\Omega_i^{(n)}} h_i^{(n)}(y) I_i^{(n)}(y) d\sigma_{\Omega_i^{(n)}}(y), \tag{3.3}$$

where $d\sigma_{\Omega_i^{(n)}}(y)$ is the volume element on the manifold, $I_i^{(n)}(y)$ is the rotational partition function, and $h_i^{(n)}(y)$ is the "geometrical" part of the vibrational partition function. The latter equals $\prod_j \lambda_j^{-1/2}$, where λ_j are the non-zero eigenvalues of the Hessian of the potential energy, in the harmonic approximation with the spring constant set to 1.

To compute Equation (3.3) numerically, we parameterize each manifold and use a finite-element method to compute the integral. The supplemental information of Holmes-Cerfon, Gortler, and Brenner[49] contains more details on how to compute the parameterization and volume element. Table 3.3 lists the numerically computed values of the total geometric partition function for the 0, 1, and 2-dimensional manifolds.

Table 3.3: The following geometrical partition functions are generated by applying the methods from Holmes-Cerfon, Gortler, and Brenner[49] to 2D clusters. Note: clusters with a single disconnected sphere are not included in these calculations.

N	Q_{2N-3}	Q_{2N-4}	Q_{2N-5}
3	0.770	4.19	–
4	4.00	23.4	60.2
5	37.0	231	763
6	498	3320	11900

We use observations of smaller clusters to determine κ independently of our 6-particle data. For 3-particle clusters, with 3-bond and 2-bond energy levels, we find $\kappa = 29.3$. We make two more measurements of κ using 4-particle clusters: a comparison of 5-bond to 4-bond energy levels yields $\kappa = 26.8$, and that of 4-bond to 3-bond levels yields $\kappa = 35.3$. Using the mean of these measurements (30.5) in the n-bond partition function $Q_n\kappa^n$, normalized by $\sum_{n=7}^{9} Q_n\kappa^n$ where $[Q_7, Q_8, Q_9] = [11900, 3320, 498]$, we predict 6-particle occupation probabilities of $p_7 = 2.1 \pm 0.6\%$, $p_8 = 17.6 \pm 2.0\%$, and $p_9 = 80.3 \pm 2.5\%$, where the uncertainties are based on the range of measured κ values. The calculations agree with our measured occupation probabilities.

The transition rates are calculated using Transition Path Theory (TPT).[87,49] To simplify the calculations we suppose that each transition occurs by a single bond breaking, followed by the cluster diffusing along a 1-dimensional path and forming another bond. We calculate the flux of probability along each path and from this extract the non-dimensional rates, exactly as in reference.[49] The dimensional rates are obtained by multiplying by $D/\kappa d^2$, where D is the average diffusion coefficient and

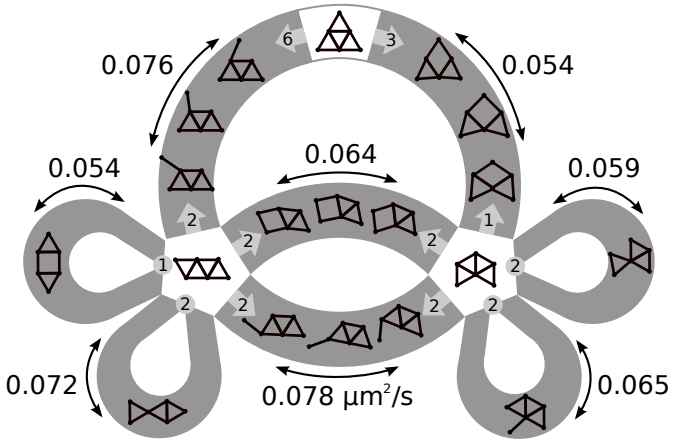

Figure 3.5: The 8-bond excited states form transition pathways (gray background) between the ground states (white background). The numbers at the edges of the ground states show the number of bonds that lead into each nearby pathway. The measured diffusion coefficients of the modes range from 0.054 to 0.078 $\mu m^2/s$ (Section 3.4.2).

d is the microsphere diameter (Table 3.2). As our implementation of the model ignores the time the clusters spend with fewer than 8 bonds, we expect it to slightly overestimate the rates.

3.4.2 Measuring the diffusion coefficients

To determine the second parameter in our model, D, we measure the mean-square displacements along each pathway. To do so, we must first parameterize each of the one-dimensional transition paths between rigid clusters. A cluster can be written as a vector $x \in \mathbb{R}^{2N}$ listing the centers of each sphere in two dimensions. We find a path $x(s)$ depending on parameter s, such that

1. $\frac{dx}{ds}$ is perpendicular to infinitesimal rotations, infinitesimal translations, and motions that change the bond lengths

2. $|\frac{dx}{ds}| = 1$.

The first is possible because the space of rotations, translations, and bond lengths is $(2N - 1)$-dimensional since there is exactly one bond "missing," so at each point along the path there is a one-

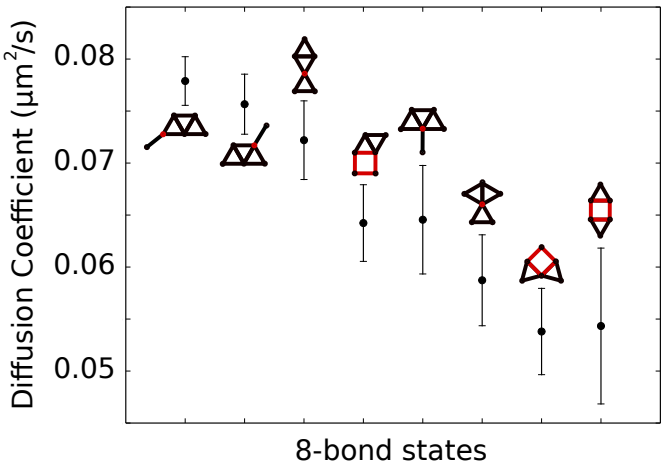

Figure 3.6: Measured diffusion coefficients for the one-dimensional soft modes of the 8-bond states. Hinge-like joints and non-rigid squares are labeled in red. The error bars are 95% confidence intervals.

dimensional tangent space spanned by unit vector t_s. The second is possible because the space we are parameterizing is one-dimensional, so we can always find an arc-length parameterization.

We store the path as a discrete set of clusters $x_{s_0}, x_{s_1}, \ldots, x_{s_m}$, where $s_k = k\Delta s$ for fixed step size Δs. Each $x_{s_{i+1}}$ is found from x_{s_i} by taking a step of size Δs in the direction of the unit tangent t_{s_i}, and then orthogonally projecting back to the manifold of constraints: $x_{s_{i+1}} = P(x_{s_i} + t_{s_i}\Delta s)$, where P is an orthogonal projection operator. The details of P are provided by Holmes-Cerfon, Gortler, and Brenner.[49].

We next analyze our data to obtain a time series of s-values along each transition path. For each data point with 8 bonds, we find its corresponding s-value by first performing an orthogonal projection onto the transition path to remove the vibrational degrees of freedom. This projection step is crucial to obtaining good statistics. Then, we identify the closest cluster in the list $\{x_{s_0}, \ldots, x_{s_m}\}$, using a Euclidean metric on the space of sorted bond distances. Finally, for each pair of consecutive points that lie on the same transition path with s-values $\hat{s}_1, \hat{s}_2$, we compute the change in s-values $\Delta = \hat{s}_2 - \hat{s}_1$.

The result is a sequence of increments $\Delta_1, \Delta_2, \ldots, \Delta_M$ associated with each transition path. Close to the ends of the manifolds, the allowed sizes of steps taken towards the end become more and more restricted by the end of the manifold. To avoid biasing due to the non-Gaussian distributions of Δ near the ends of the manifolds, we only analyze steps towards the center of the manifold. Since the velocity correlation time is much shorter than the time between measurements, the cluster performs Brownian motion along the transition path, so the average diffusion coefficient along a path can be estimated as $D = a^2 \frac{1}{2\Delta t} \frac{1}{M} \sum_{i=1}^{M} (\Delta_i^2)$. Here Δt is the time between measurements, and the average is with respect to the stationary distribution along each path. The square of the interparticle spacing, a^2, is the conversion factor between diffusion in the parameterized space and in real space. The values we arrive at are between 0.054 and $0.078\,\mu\text{m}^2/\text{s}$ with a mean of $0.065\,\mu\text{m}^2/\text{s}$ as shown in Figure 3.6. The error bars on the measured diffusion coefficients are smaller than the variation in these values between the different modes. Thus the variation is likely due to differences in hydrodynamic friction factors between these modes, and not measurement error.

Despite measuring different diffusion coefficients for the different 8-bond modes, the dimensional transition rates predicted from a simple model using a single, average diffusion coefficient agree with the measured rates, as shown in Table 3.2. Using different diffusion coefficients for each pathway yields values that agree equally well, though not better, with the data. This shows that the variation in diffusion coefficients among the different modes is not significant compared to the error in the measured transition rates. However, it also raises the question of why the diffusion coefficients for different pathways vary by only about 20% from the mean value. To understand this variation, we measure the diffusion coefficient for a rearrangement in a 3-sphere cluster and find a value of $D = 0.070\,\mu\text{m}^2/\text{s}$, close to the average value for the 6-sphere rearrangement pathways. This agreement, along with the fact that these diffusion coefficients are all lower than that for a single sphere diffusing on the plane ($D = 0.10\,\mu\text{m}^2/\text{s}$), suggests that the hydrodynamic friction factor along each pathway is dominated by flows between those spheres that must slide or roll past one another (as in the 3-sphere

cluster), rather than by hydrodynamic interactions between larger moving subunits of the clusters. This would explain why the diffusion coefficients are similar for both diamond-square-diamond and hinge-like modes.

3.5 Conclusion

Taken together, these results shed new light on the free-energy landscape, and the dynamics along it, in colloidal systems. As in 3D clusters, the short-range interaction in our 2D system leads to degeneracy in both the ground and excited states. Whereas the occupation probabilities of the ground states are determined primarily by symmetry (permutational entropy), those of the excited states are determined primarily by the entropy of the soft modes. The agreement between the measured probabilities of the excited states and those predicted from our geometrical model shows that the harmonic vibrational modes equilibrate quickly compared to motion along the soft modes. This separation of timescales is another consequence of the short-range interactions. From our geometrical model of the free-energies, we can reproduce the measured rearrangement rates between ground states by incorporating only a single diffusion coefficient and the partition function of a single bond, both of which are easily measured.

Our model easily extends to 3D clusters. Its success in describing the 2D experimental data suggests that, at least near the isostatic limit, it may be possible to use similar geometrically-inspired models to understand the free-energy landscape and predict dynamics in more complex systems with soft modes, such as bulk colloidal phases. Indeed, such models are beginning to be developed.[88]

Acknowledgements

We thank Guangnan Meng, Jonathan Goodman, and David Wales for helpful discussions. Rebecca W. Perry acknowledges the support of a National Science Foundation (NSF) Graduate Research Fel-

lowship. This work was funded by the NSF through grant no. DMR-1306410 and by the Harvard MRSEC through grant no. DMR-0820484.

4

The Partition Function of Colloidal Clusters

The partition function is at the core of statistical mechanics. It has practical utility in calculating thermodynamic variables, but its intrinsic value lies simply in its ability to tell us how likely we are to find a system in a particular macrostate. Most often, partition functions are computed for systems of atoms or subatomic particles. In this chapter, we explain how to calculate a partition function for clusters of colloidal microspheres and highlight a finding that allows us to rewrite the standard inertial component as separate mass-dependent and configuration-dependent terms, even for clusters composed of particles with different masses.

In the following, we derive the classical partition function[89] of an N-particle cluster of colloidal spheres in two different coordinate systems.[90] We compare the two resulting forms of the partition

function to understand the probability distributions of heterogeneous clusters. We were inspired to pursue this research direction after reading a commentary by Professor Cates in which he raised the question of whether the moment of inertia belongs in the partition function for a low Reynolds number system, such as our colloidal clusters, where inertia is commonly neglected.[91,16] Cates suggested that the moment of inertia might be replaced with a "moment of volume" that would not depend on mass. We find that while the inertial mass does appear in the partition function, the value of the partition function does not depend on it – regardless of the Reynolds number.

4.1 Partition Functions: from Atoms to Colloids

Typical colloidal particles are around a micrometer in diameter, or 10,000 times the diameter of a hydrogen atom, and so are purely classical objects. Each particle is distinguishable in principal by its unique arrangement of atoms. Even though colloidal spheres are orders of magnitude larger than single atoms, they are still small enough to be Brownian and to reach thermal equilibrium on experimental timescales. Thus they can be analyzed using the formalism of classical statistical mechanics. The partition function we derive is for isostatic clusters of colloidal spheres with weak, isotropic, short-range interactions at constant temperature. We make the assumption that the interparticle interactions are harmonic.

4.2 Partition Function in Particle Coordinates

Unlike the case for atoms, rotations of a spherical colloidal particle are in principal distinguishable. Therefore, each particle has 12 degrees of freedom: 3 translational, 3 linear momenta, 3 rotational, and 3 angular momenta. The most general form of the canonical partition function of a macrostate s

corresponding to a particular cluster geometry is

$$Q_s = \frac{1}{h^{6N}} \int e^{-\beta H(\mathbb{Q},\mathbb{P},\theta,\mathbb{L})} d\mathbb{Q}\, d\mathbb{P}\, d\theta\, d\mathbb{L}, \tag{4.1}$$

where N is the number of particles, and H is the Hamiltonian of the cluster. The integral is over all allowed values of the particle positions $\mathbb{Q}$, linear momenta $\mathbb{P}$, rotations θ, and angular momenta $\mathbb{L}$. The probability of a given state s is proportional to its partition function. Because the rotations of the individual particles are assumed to be uncoupled, they are identical for all states and cannot affect the probabilities. We can therefore ignore the rotational coordinates θ and angular momenta $\mathbb{L}$. The partition function becomes

$$Q_s = \frac{1}{h^{3N}} \int e^{-\beta H(\mathbb{P},\mathbb{Q})} d\mathbb{P}\, d\mathbb{Q} \tag{4.2}$$

In the Hamiltonian for our colloidal clusters, the kinetic energy depends only on the momenta, and the potential energy depends only on the positions. We can therefore separate Q_s into two integrals: one over momenta and the other over positions.

$$Q_s = \frac{1}{h^{3N}} \int e^{-\beta(K(\mathbb{P})+U(\mathbb{Q}))} d\mathbb{P}\, d\mathbb{Q} = \frac{1}{h^{3N}} \int e^{-\beta K(\mathbb{P})} d\mathbb{P} \int e^{-\beta U(\mathbb{Q})} d\mathbb{Q} \tag{4.3}$$

The kinetic energy is $\sum_{i=1}^{N} \frac{p_{ix}^2+p_{iy}^2+p_{iz}^2}{2m_i}$. This term is the only place mass enters into the partition function when working in particle coordinates. The momentum integral is Gaussian and can be integrated analytically:

$$\begin{aligned} Q_s &= \frac{1}{h^{3N}} \int_{-\infty}^{\infty} e^{-\beta \sum_{i=1}^{N} \frac{p_{ix}^2+p_{iy}^2+p_{iz}^2}{2m_i}} d\mathbb{P} \int e^{-\beta U(\mathbb{Q})} d\mathbb{Q} \\ &= \prod_{i=1}^{N} \left(\sqrt{\frac{2\pi m_i}{h^2 \beta}} \right)^3 \int e^{-\beta U(\mathbb{Q})} d\mathbb{Q} \end{aligned} \tag{4.4}$$

This expression contains the thermal de Broglie wavelength of each particle i, which we will call λ_i:

$$Q_s = \prod_{i=1}^{N} \frac{1}{\lambda_i^3} \int e^{-\beta U(\mathbb{Q})} d\mathbb{Q} \tag{4.5}$$

The remaining integral depends only on the particle positions and not their masses. This integral is aptly named the configurational integral, Z.[89]

$$\boxed{Q_s = Z \prod_{i=1}^{N} \frac{1}{\lambda_i^3}} \tag{4.6}$$

Unfortunately, the configurational integral is not easily solved in the particle coordinates. But we can gain insight by comparing Equation 4.6 to the partition function derived using center-of-mass coordinates.

4.3 Partition Function in Center-of-Mass Coordinates

To make the calculation of the entire partition function Q_s (Equation 4.2) tractable, we choose to switch from particle coordinates to center-of-mass coordinates. The kinetic and potential energies are as follows (parameters labeled in Table 4.1),

$$K(\mathbb{P}) = \sum_{t=x,y,z} \frac{p_t^2}{2M} + \sum_{j=1}^{3} \frac{L_j^2}{2I_j} + \sum_{i=1}^{3N-6} \frac{p_i^2}{2\mu_i} \tag{4.7}$$

$$U(\mathbb{Q}) = \sum_{i=1}^{3N-6} \frac{1}{2} k_i q_i^2 + U_0 \tag{4.8}$$

In writing equations 4.7 and 4.8 we have assumed that vibrations are harmonic and that there is no coupling between translational, vibrational, and rotational modes. This is sometimes called the "rigid ro-

Table 4.1: Parameters used in the center of mass coordinates starting with Equation 4.7

Rigid body coordinates and parameters:

p_t	momentum of center of mass in direction t
q_t	position of center of mass along coordinate t
L_j	angular momentum about the j^{th} principal axis
I_j	moment of inertia about the j^{th} principal axis
α	angle about an axis within the cluster
θ, ϕ	spherical coordinates
M	total mass of the cluster, $\sum m_i$

.

Vibrational coordinates and parameters:

p_i	momentum of normal mode i
q_i	normal-mode coordinate
k_i	effective spring constant of normal mode i
μ_i	effective mass of normal mode i

tor harmonic oscillator" approximation.[90] The partition function must be integrated over 6N degrees of freedom: 3 center-of-mass momenta, 3 center-of-mass positions, 3 angular momenta, 3 rigid-body rotations, 3N-6 vibrational displacement coordinates, and 3N-6 vibrational momenta. We group these together into translations, rotations, and vibrations:

$$\underbrace{dp_x\, dp_y\, dp_z\, dq_x\, dq_y\, dq_z}_{\text{rigid-body translation}}\ \underbrace{dL_1\, dL_2\, dL_3\, d\alpha\, \sin\theta d\theta\, d\phi}_{\text{rigid-body rotation}}\ \underbrace{dp_1 \ldots dp_{3N-6}\, dq_1 \ldots dq_{3N-6}}_{\text{internal vibration}} \tag{4.9}$$

Working in this set of coordinates divides the partition function into three independent contributions, one each from translations, rotations, and vibrations. We now derive each of these contributions.

4.3.1 Translation

The translational contribution is the integral over rigid-body coordinates and momenta:

$$Q_{trans} = \frac{1}{h^3} \int_V dq_x \, dq_y \, dq_z \int_{-\infty}^{\infty} e^{-\beta \sum_t \frac{p_t^2}{2M}} dp_x \, dp_y \, dp_z \tag{4.10}$$

The first of the two integrals in Equation 4.10 is independent of both the kinetic and potential energies and is equal to the volume accessible by the cluster. For small clusters in dilute suspensions, the accessible volume, or "free volume," is approximately the volume, V, of the surrounding container. For an analysis of this approximation, see Section 4.5.3. The second integral is the product of three identical Gaussian integrals:

$$\begin{aligned} Q_{trans} &= \frac{V}{h^3} \left(\int_{-\infty}^{\infty} e^{-\beta \frac{p^2}{2M}} dp \right)^3 \\ &= V \left(\sqrt{\frac{2\pi M}{h^2 \beta}} \right)^3 \end{aligned} \tag{4.11}$$

This expression contains a length scale λ_M which is the thermal de Broglie wavelength of the cluster:

$$Q_{trans} = \frac{V}{\lambda_M^3} \tag{4.12}$$

4.3.2 Rotation

The first rotational integral in Equation 4.13 is over angles of rigid-body rotation[92,93] and is independent of energy. It counts the unique states accessible via rigid body rotation.[89] If the particles are not distinguished, we must include a symmetry number, σ, to correct for overcounting. We write this integral using an axis-angle representation of rigid body rotation, but with the position of the axis spec-

ified in spherical coordinates instead of the standard Cartesian coordinates. Following the approach of Pitzer,[92] we establish an angle of rotation, α, about an arbitrarily chosen axis in the cluster and let this angle vary from 0 to 2π. We then "tilt" this axis through all possible angles by integrating over the surface of a sphere using spherical coordinates and the differential area element $dA = \sin\theta d\theta d\phi$:

$$Q_{rot} = \frac{1}{h^3}\frac{1}{\sigma}\int_0^{2\pi}\int_0^{\pi}\int_0^{2\pi}\sin\theta d\alpha\, d\theta\, d\phi \int_{-\infty}^{\infty} e^{-\beta\sum_{j=1}^{3}\frac{L_j^2}{2I_j}}\, dL_1\, dL_2\, dL_3 \tag{4.13}$$

The integral over the angles yields $8\pi^2$, while the momentum integral is the product of three Gaussian integrals:

$$\begin{aligned} Q_{rot} &= \frac{1}{h^3}\frac{8\pi^2}{\sigma}\prod_{j=1}^{3}\left(\sqrt{\frac{2\pi I_j}{\beta}}\right) \\ &= \frac{1}{\pi\hbar^3\sigma}\sqrt{\frac{8\pi^3 I_1 I_2 I_3}{\beta^3}} \\ &= \frac{2\sqrt{2\pi}}{\hbar^3\beta^{3/2}}\frac{\sqrt{I_1 I_2 I_3}}{\sigma} \end{aligned} \tag{4.14}$$

4.3.3 Vibration

The vibrational integral is over all the normal modes. There are $3N-6$ modes for a 3D cluster and $2N-3$ modes for a 2D cluster. Again, the integrals are Gaussian:

$$\begin{aligned} Q_{vib} &= \frac{1}{h^{3N-6}}\int_{-\infty}^{\infty} e^{-\beta\sum_{i=1}^{3N-6}\frac{p_i^2}{2\mu_i}}\, dp_1 ... dp_{3N-6}\int_{-\infty}^{\infty} e^{-\beta\sum_{i=1}^{3N-6}\frac{1}{2}k_i q_i^2}\, dq_1 ... dq_{3N-6} \\ &= \prod_{i=1}^{3N-6}\frac{1}{h}\sqrt{\frac{2\pi\mu_i}{\beta}}\sqrt{\frac{2\pi}{\beta k_i}} \end{aligned} \tag{4.15}$$

We can write Q_{vib} in terms of the vibrational frequencies $\omega_i = \sqrt{\frac{k_i}{\mu_i}}$:

$$Q_{vib} = \prod_{i=1}^{3N-6} \frac{1}{\beta\hbar}\sqrt{\frac{\mu_i}{k_i}} = \prod_{i=1}^{3N-6} \frac{1}{\beta\hbar\omega} \tag{4.16}$$

Thus, the vibrational partition function is inversely proportional to the product of the vibrational frequencies.

4.3.4 Complete Partition Function

Putting these three components together, we have

$$\boxed{Q_s = Q_{trans}Q_{rot}Q_{vib} = \frac{V}{\lambda_M^3}\frac{2\sqrt{2\pi}}{\hbar^3\beta^{3/2}}\frac{\sqrt{I_1 I_2 I_3}}{\sigma}\prod_{i=1}^{3N-6}\frac{1}{\beta\hbar\omega_i}} \tag{4.17}$$

which is the same as the result obtained by Herschbach, Johnston, and Rapp.[90] In this form of the partition function, the masses enter into the thermal wavelength, the moments of inertia, and the vibrational frequencies. The equivalent equation for 2D clusters is

$$Q_s = Q_{trans}Q_{rot}Q_{vib} = \frac{A}{\lambda_M^2}\frac{\sqrt{2\pi}}{\hbar\sqrt{\beta}}\frac{\sqrt{I_1}}{\sigma}\prod_{i=1}^{3N-6}\frac{1}{\beta\hbar\omega_i}. \tag{4.18}$$

4.4 Mass in the Partition Function

We now have two forms of the partition function, which together give us deeper insight into the role of mass. We equate the two boxed forms of the partition function derived for different coordinate systems (Equations 4.6 and 4.18), being careful to note that the λ_i's are thermal wavelengths of the

particles and λ_M is the thermal wavelength of the entire cluster:

$$Z\prod_{i=1}^{N}\frac{1}{\lambda_i^3}=\frac{V}{\lambda_M^3}\frac{2\sqrt{2\pi}}{\hbar^3\beta^{3/2}}\frac{\sqrt{I_1I_2I_3}}{\sigma}\prod_{i=1}^{3N-6}\frac{1}{\beta\hbar\omega_i} \tag{4.19}$$

On the left-hand side, the masses are contained to the product of de Broglie wavelengths, but the configurational integral Z remains a mystery. On the right-hand side, the calculation is complete, but mass has entered the equation in multiple places: the de Broglie wavelength, the moments of inertia, and the vibrational frequencies. To isolate the functional form of the mass-dependence on both sides, we group the other parameters into two functions, f (unknown) and g (known):

$$f(h,\beta,q,\sigma,V,k)\prod_{i=1}^{N}\frac{1}{\lambda_i^3}=g(h,\beta,\sigma,V)\frac{\sqrt{I_1I_2I_3}}{\lambda_M^3}\prod_{i=1}^{3N-6}\frac{1}{\omega_i} \tag{4.20}$$

Here q's are the positions of the particles and k's are the spring constants of the interparticle potentials. Next we extract the individual particle masses m_i and the cluster's total mass M from the de Broglie wavelengths and merge the other contributions to the de Broglie wavelengths with functions f and g to form functions F and G:

$$F(h,\beta,q,\sigma,V,k)\prod_{i=1}^{N}m_i^{3/2}=G(h,\beta,\sigma,V)M^{3/2}\sqrt{I_1I_2I_3}\prod_{i=1}^{3N-6}\frac{1}{\omega_i} \tag{4.21}$$

$$F(h,\beta,q,\sigma,V,k)\prod_{i=1}^{N}m_i^{3/2}=G(h,\beta,\sigma,V)(\sum_{i=1}^{N}m_i)^{3/2}\sqrt{I_1I_2I_3}\prod_{i=1}^{3N-6}\frac{1}{\omega_i} \tag{4.22}$$

Because each side of the equation should depend on the mass in the same way, we can determine the mass-dependence of the product of the moments of inertia and the vibrational frequencies:

$$\sqrt{I_1 I_2 I_3} \prod_{i=1}^{3N-6} \frac{1}{\omega_i} = j(h, \beta, q, \sigma, V, k) \frac{\prod_{i=1}^{N} m_i^{3/2}}{(\sum_{i=1}^{N} m_i)^{3/2}} \tag{4.23}$$

In 2D clusters, which have one rotational degree of freedom and two translational degrees of freedom:

$$\sqrt{I_1} \prod_{i=1}^{2N-3} \frac{1}{\omega_i} = j(h, \beta, q, \sigma, V, k) \frac{\prod_{i=1}^{N} m_i}{\sum_{i=1}^{N} m_i} \tag{4.24}$$

This result shows that the cluster partition function (Equation 4.18) is the product of two terms, one of which (the function j) depends on the particle positions but not the masses, and the other of which depends only on the masses. It therefore follows that in a heterogeneous cluster, swapping the positions of spheres with different masses does not change the partition function. Thus, the probabilities of different arrangements do not depend on the positions of spheres of different masses.

The possibility of separating the partition function into two such terms is not obvious from Equation 4.18 alone. In the general case of particles with non-identical masses, neither the moments of inertia nor the vibrational frequencies can be written as a product of terms depending separately on the masses and the particle positions. Only by considering the moments of inertia and the vibrational frequencies together are we able to separate the mass-dependence and the position-dependence into two terms.

4.5 Calculating Partition Functions for Colloidal Clusters

Although we have derived an analytical solution to the partition function (Equation 4.18), calculating its value for a cluster of interest still requires some work. This section serves as a guide to computing the translational, rotational, and vibrational components of the partition function for 2D and 3D clusters of spheres with short-range interactions. To illustrate each calculation we use small 2D clusters as examples.

4.5.1 Rotational Contribution

The rotational partition function accounts for the number of unique rotational microstates:

$$Q_{rot} = \chi \frac{\sqrt{2\pi}}{\hbar\sqrt{\beta}} \frac{N!\sqrt{I}}{\sigma}, \tag{4.25}$$

where $\frac{N!}{\sigma} = Q_{perm}$ is the permutational partition function, χ is the chirality ($\chi = 2$ for a state representing two chiral enantiomers and 1 otherwise), and I is the determinant of the moment of inertia tensor of the cluster (the product of the moments of inertia about the principal axes). $N!$ enters this equation for the most general case of distinguishable particles. The chirality enters this equation because we might choose to group pairs of chiral enantiomers together.

The permutational partition function is proportional to the number of ways to arrange distinguishable particles into a given cluster such that the resulting configurations are distinguishable even when rotations are allowed. To show the relationship between rotational symmetry and unique permutations, we examine the 3-particle ground state. Figure 4.1 shows the six possible permutations of distinguishable particles, where color is used as a label. If the clusters are free to rotate about an axis perpendicular to the page, the three clusters in the top row are indistinguishable from one another, as are the three clusters in the bottom row. This collapse of the six possible permutations into just two

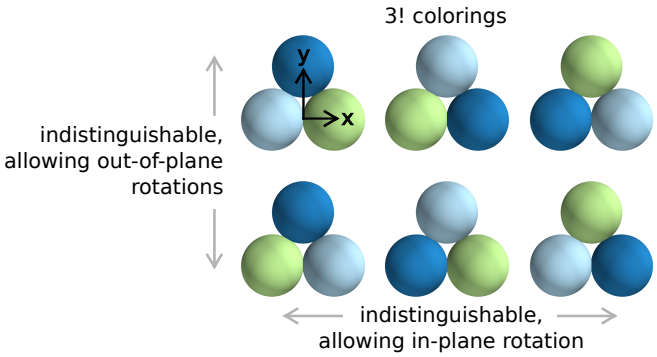

Figure 4.1: These clusters show the six possible permutations of particles in a 3-particle cluster. Colors label the particles. If rotations in the plane are allowed, the clusters in the top row are indistinguishable from one another, and similarly in the bottom row. If rotations out of the plane of the page are allowed, all of the colorings become indistinguishable. The axes give us a reference frame to work with in Section 4.5.2.

distinguishable states is the result of the 3-fold symmetry axis ($\sigma = 3$). If the clusters can rotate about any axis, the two groups of colorings collapse into just one, a result of the additional 2-fold symmetry axis in three dimensions. Larger clusters have too many permutations to show here, but we list the components of Q_{rot} for the 6-particle ground states in two dimensions in Table 3.1. Because we choose not to distinguish particles in our experiments, we divide by $N!$, and we write $Q_{perm} \propto \frac{1}{\sigma}$, as is stated by Meng *et al.*[16] In Section 5.4, we show how to calculate permutations for clusters composed of different types of spheres.

The final contribution to the rotational partition function is the determinant of the moment-of-inertia tensor. In two dimensions, I is the moment of inertia about the single rotational axis perpendicular to the plane of the cluster and running through the cluster's center of mass, $\mathbf{q}_0$:

$$I = \sum_{i=1}^{N} \mid \mathbf{q}_i - \mathbf{q}_0 \mid^2 m_i \tag{4.26}$$

When all the particles have the same mass m, I is proportional to m. Carrying out this calculation for a 3-particle triangle in which each sphere lies at a distance of $\frac{\sqrt{3}}{3}d$ from the center and has mass m, we

find the moment of inertia to be d^2m.

Combining the number of permutations and the moment of inertia, we find that the complete rotational partition function $Q_{rot} = \frac{\sqrt{2\pi}}{\hbar\sqrt{\beta}} \frac{d\sqrt{m}}{3}$ for the triangle, which is not chiral and has a symmetry number of 3. Table 3.1 illustrates how Q_{rot} varies among the 2D 6-particle ground states, affecting the states' probabilities.

4.5.2 Vibrational Contribution

The vibrational contribution is the most computationally intensive component of the partition function to calculate. Each 2D ground state has 2N-3 vibrational modes, and each 3D ground state has 3N-6 vibrational modes. The vibrational partition function depends on the product of these vibrational frequencies:

$$Q_{vib} = \prod_i \frac{1}{\beta\hbar\omega_i(k,m,q)} \tag{4.27}$$

The vibrational frequencies are the square roots of the non-zero eigenvalues of the Hessian, which is the matrix of second derivatives of the potential energy. We will illustrate the calculation of the normal modes using the 3-particle ground state and following the methods of Tuzun and coworkers[94] and Eyal and coworkers.[95]

The triangle has three vibrational modes in both two and three dimensions. To simplify the calculation, we ignore the z-component of the particle coordinates. The potential energy in the harmonic approximation (Equation 4.8) is

$$\begin{aligned} U = \quad & \tfrac{1}{2}k_{12}(\sqrt{(x_1-x_2)^2+(y_1-y_2)^2} - d_0)^2 + \\ & \tfrac{1}{2}k_{13}(\sqrt{(x_1-x_3)^2+(y_1-y_3)^2} - d_0)^2 + \\ & \tfrac{1}{2}k_{23}(\sqrt{(x_2-x_3)^2+(y_2-y_3)^2} - d_0)^2 + U_0 \end{aligned} \tag{4.28}$$

where d_0 is the equilibrium distance between sphere centers and $k_{ij} = U''_{ij}$ is the spring constant of

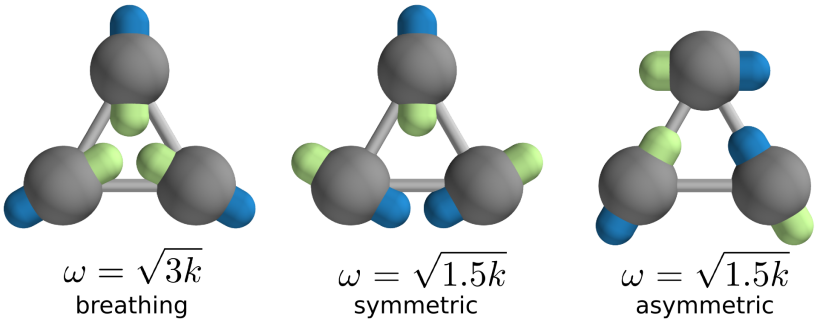

Figure 4.2: These depictions of the normal modes show the cluster in its equilibrium position (gray spheres) as well as its motion in both halves of its oscillation cycle (towards the blue end or towards the green end). The 3-particle cluster has a breathing mode, a symmetric mode, and an asymmetric mode. The normal modes for the 6-particle ground states in two dimensions are given in Appendix D.

the potential between particles i and j. In this case the Hessian is a 6x6 matrix which can be subdivided into a 3x3 grid of super-elements, each characterizing the interaction between a pair of particles:

$$H = \left[\begin{array}{c|c|c} H_{11} & H_{12} & H_{13} \\ \hline H_{21} & H_{22} & H_{23} \\ \hline H_{31} & H_{32} & H_{33} \end{array}\right]. \tag{4.29}$$

Each super-element is proportional to the normalized outer product of displacement vectors:

$$H_{ij} = \begin{bmatrix} \frac{\partial^2 U}{\partial x_i \partial x_j} & \frac{\partial^2 U}{\partial x_i \partial y_j} \\ \frac{\partial^2 U}{\partial y_i \partial x_j} & \frac{\partial^2 U}{\partial y_i \partial y_j} \end{bmatrix} = -k_{ij} \frac{(\vec{r_i} - \vec{r_j}) \otimes (\vec{r_i} - \vec{r_j})}{(\vec{r_i} - \vec{r_j}) \cdot (\vec{r_i} - \vec{r_j})} = -\frac{k_{ij}}{d_0} (\vec{r_i} - \vec{r_j}) \otimes (\vec{r_i} - \vec{r_j}). \tag{4.30}$$

If a particular pair of particles is not bound, the superelement is a zero matrix. Because the Hessian is symmetric and the super-elements along the diagonal can be computed from the other super-elements

of the same row, we need only to compute a triangular matrix, which we can do with outer products:

$$H = \frac{1}{d_0}\left[\begin{array}{c|c|c} -\sum_{j|j\neq 1} H_{1j} & -k_{12}(\vec{r_1}-\vec{r_2})\otimes(\vec{r_1}-\vec{r_2}) & -k_{13}(\vec{r_1}-\vec{r_3})\otimes(\vec{r_1}-\vec{r_3}) \\ \hline H_{12} & -\sum_{j|j\neq 2} H_{2j} & -k_{23}(\vec{r_2}-\vec{r_3})\otimes(\vec{r_2}-\vec{r_3}) \\ \hline H_{13} & H_{23} & -\sum_{j|j\neq 3} H_{3j} \end{array}\right] \tag{4.31}$$

Carrying out the calculation of the Hessian for the 3-particle triangle with identical spring constants k, in the coordinate system given in Figure 4.1, we find:

$$H(k_{ij}=k) = k\left[\begin{array}{cc|cc|cc} \frac{5}{4} & \frac{\sqrt{3}}{4} & -1 & 0 & \frac{-1}{4} & \frac{-\sqrt{3}}{4} \\ \frac{\sqrt{3}}{4} & \frac{3}{4} & 0 & 0 & \frac{-\sqrt{3}}{4} & \frac{-3}{4} \\ \hline -1 & 0 & \frac{5}{4} & \frac{-\sqrt{3}}{4} & \frac{-1}{4} & \frac{\sqrt{3}}{4} \\ 0 & 0 & \frac{-\sqrt{3}}{4} & \frac{3}{4} & \frac{\sqrt{3}}{4} & \frac{-3}{4} \\ \hline \frac{-1}{4} & \frac{-\sqrt{3}}{4} & \frac{-1}{4} & \frac{\sqrt{3}}{4} & \frac{1}{2} & 0 \\ \frac{-\sqrt{3}}{4} & \frac{-3}{4} & \frac{\sqrt{3}}{4} & \frac{-3}{4} & 0 & \frac{3}{2} \end{array}\right] \tag{4.32}$$

The super-element for H_{12} has only one non-zero element because particles 1 and 2 both lie on one coordinate axis. The eigenvalues of H are the squared normal mode frequencies which depend only on the spring constants and the positions of the particles. Using the scientific programming package NumPy[96] to find the eigenvectors and eigenvalues of H, we obtain the vibrational modes and frequencies shown in Figure 4.2. To calculate the vibrational frequencies, which additionally depend on the masses of the particles, we must incorporate the masses by mass-weighting the coordinates. Each

super-element H_{ij} is divided by $\sqrt{m_i m_j}$:

$$H_m(k_{ij}=k) = k \left[\begin{array}{cc|cc|cc} \frac{5}{4m_1} & \frac{\sqrt{3}}{4m_1} & \frac{-1}{\sqrt{m_1 m_2}} & 0 & \frac{-1}{4\sqrt{m_1 m_3}} & \frac{-\sqrt{3}}{4\sqrt{m_1 m_3}} \\ \frac{\sqrt{3}}{4m_1} & \frac{3}{4m_1} & 0 & 0 & \frac{-\sqrt{3}}{4\sqrt{m_1 m3}} & \frac{-3}{4\sqrt{m_1 m_3}} \\ \hline \frac{-1}{\sqrt{m_1 m_2}} & 0 & \frac{5}{4m_2} & \frac{-\sqrt{3}}{4m_2} & \frac{-1}{4\sqrt{m_2 m_3}} & \frac{\sqrt{3}}{4\sqrt{m_2 m_3}} \\ 0 & 0 & \frac{-\sqrt{3}}{4m_2} & \frac{3}{4m_2} & \frac{\sqrt{3}}{4\sqrt{m_2 m_3}} & \frac{-3}{4\sqrt{m_2 m_3}} \\ \hline \frac{-1}{4\sqrt{m_1 m_3}} & \frac{-\sqrt{3}}{4\sqrt{m_1 m_3}} & \frac{-1}{4\sqrt{m_2 m_3}} & \frac{\sqrt{3}}{4\sqrt{m_2 m_3}} & \frac{1}{2m_3} & 0 \\ \frac{-\sqrt{3}}{4\sqrt{m_1 m_3}} & \frac{-3}{4\sqrt{m_1 m_3}} & \frac{\sqrt{3}}{4\sqrt{m_2 m_3}} & \frac{-3}{4\sqrt{m_2 m_3}} & 0 & \frac{3}{2m_3} \end{array}\right] \tag{4.33}$$

The eigenvalues for identical springs and masses are $\omega^2 = [\frac{3k}{m}, \frac{1.5k}{m}, \frac{1.5k}{m}]$, so the vibrational contribution is

$$Q_{vib} = \prod_i \frac{1}{\beta\hbar\omega_i(k,m,q)} = \frac{1}{\beta^3\hbar^3}\frac{1}{(\sqrt{k})^3}\frac{\sqrt{m}^3}{\sqrt{3\times 1.5\times 1.5}}. \tag{4.34}$$

We notice that the spring constants come into the vibrational partition function as a prefactor. After numerically calculating the vibrational partition function for different 2D and 3D structures with different combinations of k_{ij}'s and m_i's, we noticed that we could always include the spring constants as a prefactor, but that this was not true for the masses. We do not have a proof for this as of yet, but Holmes-Cerfon and collaborators found the same spring-constant-dependence in the limit of very short-range interactions.[49] We write Q_{vib} in terms of the spring constants and the frequencies calculated for unit spring constants:

$$Q_{vib} = \prod_i \frac{1}{\beta\hbar\omega_i(k,m,q)} = \prod_j \frac{1}{\sqrt{k_j}} \prod_i \frac{1}{\beta\hbar\omega_i(k=1,m,q)} \tag{4.35}$$

The small triangular cluster was used as an example because the Hessian matrices quickly become too large to display for larger N, and seeing the larger Hessians provides little additional insight. However, because there is only one ground state for the 3-particle cluster, we have no probabilities to predict

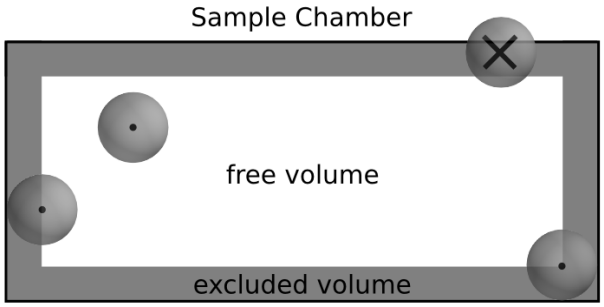

Figure 4.3: Spherical particles can be anywhere in the sample chamber except for the excluded volume extending one particle radius in from the chamber walls. Positions within the excluded volume, such as the position of the particle marked with an "X," are not allowed because they require that a particle breaches a chamber wall.

using the vibrational contributions. We have carried out the same computation for 4- and 6-particle clusters. The results of the 4-particle calculations are given in 4.6.2, and the 6-particle results can be found in Table 3.1. Diagrams of the 6-particle modes can be found in Appendix D.

4.5.3 Translational Contribution

The translational component of the partition function accounts for the microstates accessed by translation of the cluster center of mass throughout a sample volume. The accessible volume, called the free volume, depends on a cluster's size and shape. Individual hard spherical particles can access a free volume equal to the sample volume minus the volume of a one-radius-thick shell lining the sample chamber as shown in Figure 4.3. The center of the sphere cannot enter this shell, called the excluded volume, because the sphere cannot overlap with the walls of the chamber. For anisotropic particles such as clusters of spheres, the free volume depends on the cluster geometry. However, we can ignore the difference in free volume when the size of the sample chamber is much larger than the size of the excluded volume. Below we show conditions under which we can assume Q_{trans} differs negligably for different clusters.

While it is certainly safe to make this assumption when the size of the container is large compared to the size of the cluster, it is additionally safe to make this assumption whenever the free volumes

of different anisotropic particles are each affected similarly by the edges of the container, as we will explain. For anisotropic particles, the width of the excluded region near a chamber wall depends on the orientation of the cluster. The free volume must take into account the translation of the cluster at all possible orientations. To calculate the 3D free volume V_f or the 2D free area A_f, we integrate not only over the 3D or 2D sample chamber but also over the orientations of the cluster[97]:

$$\begin{aligned} \text{3D:} \quad Q_{trans} \propto V_f &= \int 1_E(\mathbf{q}, \alpha, \theta, \phi)\, \mathrm{d}^3\mathbf{q}\, \mathrm{d}\alpha\, \sin\theta \mathrm{d}\theta\, \mathrm{d}\phi \\ \text{2D:} \quad Q_{trans} \propto A_f &= \int 1_E(\mathbf{q}, \alpha)\, \mathrm{d}^2\mathbf{q}\, \mathrm{d}\alpha \end{aligned} \tag{4.36}$$

where 1_E (the indicator function) is 0 when the position $\mathbf{r}$ and orientation α, θ, ϕ of the cluster result in overlaps with the chamber boundary and 1 otherwise.

To illustrate the impact of the boundary on a set of degenerate ground states, we consider 2D 6-particle clusters in a square container. We calculate the accessible orientations as a function of distance from the wall by numerically evaluating the indicator function from Equation 4.36 near a flat boundary. We specify the position of a cluster by the center of a circumscribing circle. This center position differs from the center of mass only for the case of the chevron, which would have a more complex curve, but identical integral, if we worked in a center-of-mass frame. In the interior of the large square chamber shown in Figure 4.4 all three ground states can rotate and translate freely, but as they approach the edges, their orientations become restricted at distances equal to the radii of their circumscribing circles. The triangle's accessible rotation falls off smoothly with the distance to the wall because the distance from the triangle's center to each of its edges is identical. The chevron and parallelogram both have two length scales, which add kinks to their accessible rotation curves. The distances for each of the distinctive features in the chevron's accessible rotation curve are illustrated in Figure 4.4. The accessible orientation curves all fall from 2π to 0 over a distance of less than a particle diameter.

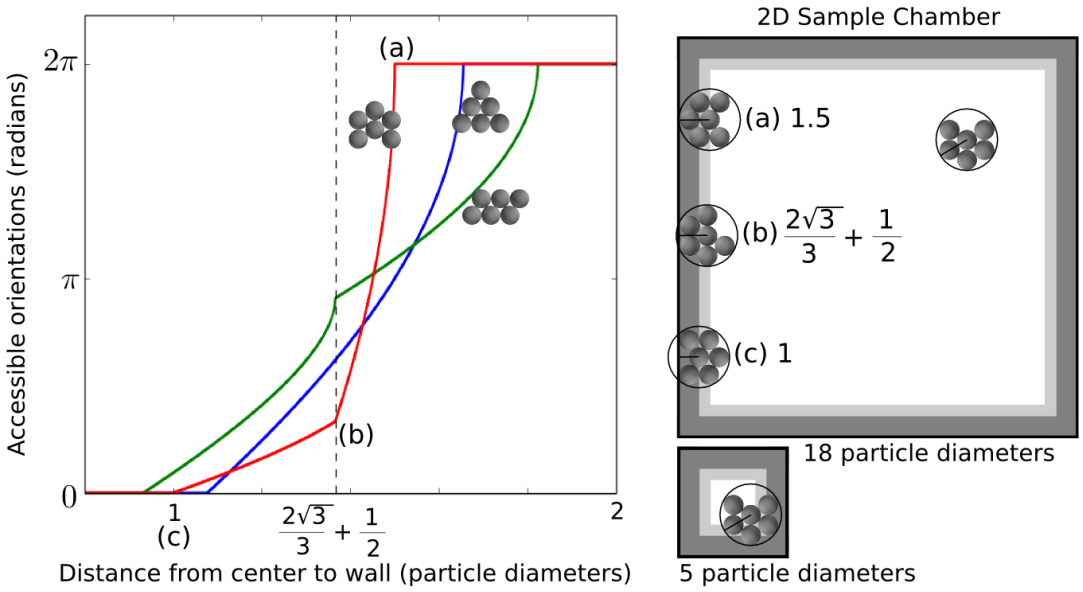

Figure 4.4: A cluster's allowed orientations become restricted as the cluster gets closer to the wall. The functional form of this restriction depends on the geometry of the cluster. The chevron is first restricted by the wall (a) when the center of a circumscribing circle is 1.5 particle diameters from the wall. The closest approach that four of the edges can make occurs at (b), $2\sqrt{3}/3 + 1/2$ where a kink occurs in the accessible orientation curve. No orientations of the chevron are allowed at distances below (c). This distance of closest approach is 1 particle diameter. The light gray border is the area in which the cluster can rotate over an angle less than 2π. The dark gray border is the excluded area for all orientations. The area with restricted rotations and the excluded area become more significant in small sample chambers.

The integrals of the functions plotted in Figure 4.4 determine the free volume. Although the functions are different for the triangle and the parallelogram, their integrals are almost identical, so the boundary has little effect on the relative probability of observing a triangle or parallelogram. The chevron, however, has slightly more free volume near the boundary. In a 18×18 particle-diameter microwell, the chevron will have 1% more free volume. In a 5×5 particle-diameter microwell, the difference increases to 7%. These cases are illustrated in Figure 4.4. The calculation does not double count the corners, but also does not account for their excluded volume precisely. In the small microwell, the corners will likely influence the probability of different clusters

The experiments in this thesis are all performed in sample chambers that are thousands of particle diameters wide and long and tens of particle diameters deep. Thus, in our experiments, we can assume Q_{trans} to be the same for different clusters. To produce a 2% change in the probability of the chevron relative to the triangle, we would need a microwell of 5-10 particle diameters. Again, this calculation does not accurately account for the excluded volume in the corners. Nonetheless, the calculation suggests that it is possible to observe the effect of Q_{trans} on different clusters in an experimentally realizable system.

4.6 Evidence for the Irrelevance of Mass Distribution

Now that we have the tools for calculating partition functions for any rigid cluster, we can return to the effect of mass. We calculate the partition functions of 3- and 4-particle clusters to verify the mass dependence of $\sqrt{I}/\prod \omega_i$ found in Section 4.4. We use SymPy[98] to analytically calculate the eigenvalues for the vibrational modes. We expect that this part of the partition function scales as

$$\frac{\prod_{i=1}^{N} m_i}{\sum_{i=1}^{N} m_i} \times \frac{1}{\prod_{i=1}^{2N-3} \sqrt{k_i}} \tag{4.37}$$

For identical masses m_0 and springs k_0, the scaling reduces to:

$$\frac{m_0^{N-1}}{k_0^{(2N-3)/2}} \tag{4.38}$$

4.6.1 3-PARTICLE CLUSTER

We have already calculated the moment of inertia and the vibrational frequencies of a triangular cluster of three particles each with $d = 1$ in Sections 4.5.1 and 4.5.2 . We combine the two terms here:

$$I = m_0 \tag{4.39}$$

$$\omega^2 = \left[\frac{3k_0}{m_0}, \frac{3k_0}{2m_0}, \frac{3k_0}{2m_0}\right], \tag{4.40}$$

$$\prod_{i=1}^{3} \frac{1}{\omega_i} = \frac{2m_0^{3/2}}{3\sqrt{3}k_0^{3/2}}, \tag{4.41}$$

$$\text{and} \qquad \frac{\sqrt{I}}{\prod \omega_i} = \frac{2m_0^2}{3\sqrt{3}k_0^{3/2}} \tag{4.42}$$

Equation 4.42 agrees with Equation 4.38.

4.6.2 4-PARTICLE CLUSTER

For a 2D cluster of four particles of identical mass m_0 and identical particle diameter 1 (Figure 4.5a),

$$I = 2m_0 \tag{4.43}$$

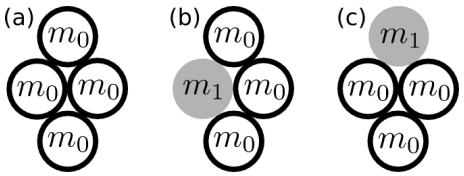

Figure 4.5: (a) The 2D cluster of four particles is a diamond. When one particle has a different mass, m_1, the cluster can form two configurations: (b) the different mass is on the short axis, or (c) the different mass is on the long axis.

$$\omega^2 = \left[\frac{k_0}{m_0}, \frac{k_0}{m_0}, \frac{2k_0}{m_0}, \frac{3k_0}{m_0}, \frac{3k_0}{m_0}\right], \tag{4.44}$$

$$\prod_{i=1}^{5} \frac{1}{\omega_i} = \frac{m_0^{5/2}}{\sqrt{18}k_0^{5/2}}, \tag{4.45}$$

$$\text{and} \qquad \frac{\sqrt{I}}{\prod \omega_i} = \frac{m_0^3}{3k_0^{5/2}}, \tag{4.46}$$

in agreement with Equation 4.38.

Now we change the mass of one of the particles to compare the resulting two configurations. We first consider the configuration shown in Figure 4.5b, a 4-particle diamond with one particle of mass m_1 on the short axis:

$$I = \frac{m_0(5m_0 + 3m_1)}{3m_0 + m_1} \tag{4.47}$$

$$\omega^2 = \left[\frac{k_0}{m_0}, \frac{3k_0m_0+5k_0m_1 \pm k_0\sqrt{9m_0^2-6m_0m_1+13m_1^2}}{4m_0m_1}, \frac{3k_0m_0+7k_0m_1 \pm k_0\sqrt{9m_0^2-18m_0m_1+13m_1^2}}{4m_0m_1}\right] \tag{4.48}$$

$$\prod_{i=1}^{5} \frac{1}{\omega_i} = \frac{4m_0^{5/2}m_1}{3k_0^{5/2}\sqrt{(5m_0 + 3m_1)(3m_0 + m_1)}}, \tag{4.49}$$

$$\text{and} \qquad \begin{aligned} \frac{\sqrt{I}}{\prod \omega_i} &= \sqrt{\frac{m_0(5m_0+3m_1)}{3m_0+m_1}} \frac{4m_0^{5/2}m_1}{3k_0^{5/2}\sqrt{(5m_0+3m_1)(3m_0+m_1)}} \\ &= \frac{4m_0^3 m_1}{3k_0^{5/2}(3m_0+m_1)} \end{aligned} \tag{4.50}$$

Repeating the calculation, but with the configuration shown in Figure 4.5c where the different particle is on the long axis:

$$I = \frac{m_0(3m_0+5m_1)}{3m_0+m_1} \tag{4.51}$$

$$\omega^2 = \left[\frac{3k_0}{m_0}, \frac{k_0 m_0 + 5k_0 m_1 \pm k_0\sqrt{m_0^2 - 2m_0m_1 + 5m_1^2}}{4m_0m_1}, \frac{3k_0 m_0 + 5k_0 m_1 \pm k_0\sqrt{9m_0^2 - 6m_0m_1 + 13m_1^2}}{4m_0m_1} \right] \tag{4.52}$$

$$\prod_{i=1}^{5} \frac{1}{\omega_i} = \frac{4m_0^{5/2}m_1}{3k_0^{5/2}\sqrt{(3m_0+5m_1)(3m_0+m_1)}}, \tag{4.53}$$

$$\text{and} \qquad \begin{aligned} \frac{\sqrt{I}}{\prod \omega_i} &= \sqrt{\frac{m_0(3m_0+5m_1)}{3m_0+m_1}} \frac{4m_0^{5/2}m_1}{3k_0^{5/2}\sqrt{(3m_0+5m_1)(3m_0+m_1)}} \\ &= \frac{4m_0^3 m_1}{3k_0^{5/2}(3m_0+m_1)} \end{aligned} \tag{4.54}$$

As expected, Equation 4.54 equals Equation 4.50. The two expressions are equal regardless of the values chosen for m_0 and m_1. With these examples, we have verified that mass has no bearing on the probabilities of configurations of heterogeneous clusters.

4.7 Discussion

We have shown that the partition function does not depend on which particles in the cluster have which masses. It depends only on the sum and product of the masses. This result is valid for *any* classical system within the harmonic approximation.

To round out this discussion, we present one more result that stems from the previous results. Not only can we derive the mass- and spring-constant-dependence of the $\sqrt{I}/\prod\omega$ term, we can also derive its full form. To do so, we derive the function $j(h,\beta,q,\sigma,k)$ from Equation 4.23. We first separate the k-dependence and rewrite the equation in terms of a new unknown function J:

$$\sqrt{I_1 I_2 I_3}\prod_{i=1}^{3N-6}\frac{1}{\omega_i} = J(h,\beta,q,\sigma)\times\frac{\prod_{i=1}^{N} m_i^{3/2}}{\sum_{i=1}^{N} m_i^{3/2}}\times\frac{1}{\prod_{i=1}^{3N-6}\sqrt{k_i}} \tag{4.55}$$

We consider the case where $m_i = 1$ and $k_i = 1$:

$$\sqrt{I_1(m_i=1)I_2(m_i=1)I_3(m_i=1)}\prod_{i=1}^{3N-6}\frac{1}{\omega_i(m_i=k_i=1)} = J(h,\beta,q,\sigma)\times\frac{1}{N}. \tag{4.56}$$

It is clear that, at least in this case,

$$J(h,\beta,q,\sigma) = N\sqrt{I_1(m_i=1)I_2(m_i=1)I_3(m_i=1)}\prod_{i=1}^{3N-6}\frac{1}{\omega_i(m_i=k_i=1)} \tag{4.57}$$

Because J does not depend on the masses or the spring constants, we know that this is also the form of J in general. Finally, we can write $\sqrt{I}/\prod\omega$ as the product of three terms that depend independently on the particle coordinates, the particle masses, and the spring constants:

$$\sqrt{I_1 I_2 I_3}\prod_{i=1}^{3N-6}\frac{1}{\omega_i} = \frac{\sqrt{I_1(m=1)I_2(m=1)I_3(m-1)}}{\prod\omega_i(k=1,m=1)}\times\frac{N\prod_{i=1}^{N} m_i^{3/2}}{\sum_{i=1}^{N} m_i^{3/2}}\times\frac{1}{\prod_{i=1}^{3N-6}\sqrt{k_i}} \tag{4.58}$$

We can use Equations 4.18 and 4.58 to determine the configurational integral, Z, which we were

unable to calculate at the beginning of the chapter (Equation 4.6)!

$$Q_s = Z\prod_{i=1}^{N}\frac{1}{\lambda_i^3} =$$

$$\frac{V}{\lambda^3}\frac{2\sqrt{2\pi}}{\hbar^3\beta^{3/2}}\frac{1}{\sigma\hbar^{3N-6}\beta^{3N-6}}\frac{\sqrt{I_1(m=1)I_2(m=1)I_3(m=1)}}{\prod\omega_i(k=1,m=1)}\frac{N\prod_{i=1}^{N}m_i^{3/2}}{\sum_{i=1}^{N}m_i^{3/2}}\frac{1}{\prod_{i=1}^{3N-6}\sqrt{k_i}} \tag{4.59}$$

All that remains to be done is to cancel the explicit mass dependences on both sides while being careful to keep track of powers of 2, π, h, and β. The "moment of volume," which is the moment of inertia term calculated for unit masses, proposed by Cates,[91] does appear in our expression. Each of the principal moments of inertia calculated for unit masses ($I_i(m=1)$) is equal to NR_{g_i} where R_{g_i} is the radius of gyration about the i^{th} principal axis. In addition, we see that the frequencies of the stiffness matrix (Equation 4.32) appear instead of the frequencies of the dynamical matrix (Equation 4.33). Solving equation 4.59, we arrive at the configurational integral:

$$Z = \frac{(2\pi)^{3N/2-1}}{\beta^{3N/2-3}}\frac{2NV\sqrt{N^3R_{g_1}R_{g_2}R_{g_3}}}{\sigma}\prod_{i=1}^{3N-6}\frac{1}{\omega_i(k=1,m=1)}\prod_{i=1}^{3N-6}\frac{1}{\sqrt{k_i}} \tag{4.60}$$

Our final form of the classical partition function (Equation 4.59) is useful as a practical tool because the "moment of volume" and the vibrational frequencies need only be computed once for each geometry. They can even be stored in a table. Then, computing the partition function for any set of masses and springs involves simply determining the symmetry number and doing some products and sums.

The first time we noticed the separation of mass- and position-dependence in a partition function was while considering the experiments of Chapter 5. In those experiments, we study the systems depicted in Figure 4.6 made using a mixture of silica and polystyrene spheres, which differ by a factor

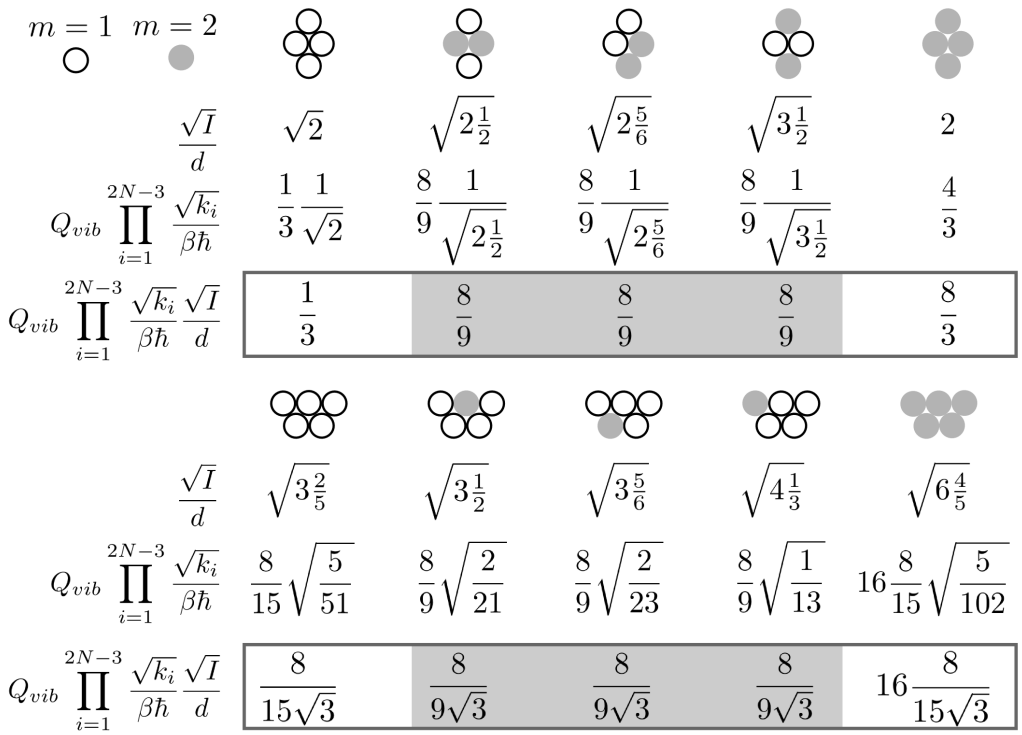

Figure 4.6: The product of the contribution of the moment of inertia from Q_{rot} and the contribution of the vibrational modes does not vary across the different configurations of light (white, $m = 1$) and heavy (gray, $m = 2$) particles. The same set of values are provided for homogeneous clusters of both types of spheres to provide context.

of two in their densities. Indeed, we were unable to see any mass effect in the probabilities of clusters with different configurations of heavy and light spheres.

5

Isotope Effects in Colloidal Molecules

5.1 Self-Assembly of Heterogeneous Colloidal Molecules

To build functional colloidal structures, one needs to put together microspheres with different conductivities, opacities, and chemistries into specific arrangements. One way to do this is to engineer attractive interactions that are specific to different kinds of particles. Clusters of heterogeneous particles have been assembled using size-dependent depletion interactions,[13,99,100] electrostatic interactions,[101,102,103] and complementary DNA sequences.[103,104] DNA-grafted patchy particles have been used to create clusters that mimic molecules made from carbon atoms.[105] The structures created using these various methods are often called "colloidal molecules."[106,107,108,109]

Here, we investigate the self-assembly of 2D colloidal molecules (hereafter simply called molecules) from a mix of monodisperse polystyrene and silica microspheres. We find that the particles of the minority component, or "dopants," preferentially segregate to certain dopant-type-dependent

positions in the molecules. A similar effect was recently observed in simulations of isotropic bidisperse particles.[110] In our study, we focus solely on molecules of fewer than 6 particles. We refer to our two species of colloidal particles as "isotopes" because they have different masses (silica is twice as dense as polystyrene) but nearly the same sizes – and thus substituting one for the other does not change the bond network. The introduction of just one additional isotope into a colloidal molecule leads to three different bond types. In our system, there are polystyrene-polystyrene, polystyrene-silica, and silica-silica bonds. We find that by manipulating these three interactions, we can maximize the yield of certain colloidal isomers.

The molecules in this study have weak bonds, a few k_BT in depth, to allow the molecules to equilibrate quickly. In an equilibrium ensemble, there is a distribution of different molecules. We provide design rules for maximizing the yield of certain isomers in an equilibrium ensemble by varying the interparticle potentials and the stoichiometric ratio of the two isotopes. We estimate maximum yields of certain isomers and highlight other isomers whose yields cannot be enhanced relative to those in a single-component system.

5.2 Experimental and Computational Methods

In our experiments, we prepare equilibrium ensembles of thousands of colloidal molecules, image them by raster-scanning, and then post-process the images to determine their sizes, compositions, and configurations.

5.2.1 Self-Assembly of Thousands of Molecules

We construct a thin sample chamber in which colloidal particles can self-assemble into 2D molecules at the bottom of the chamber through diffusion and sedimentation. The sample chamber consists of two plasma-cleaned coverslips separated by 35 μm Mylar® A spacers (sample chamber prepara-

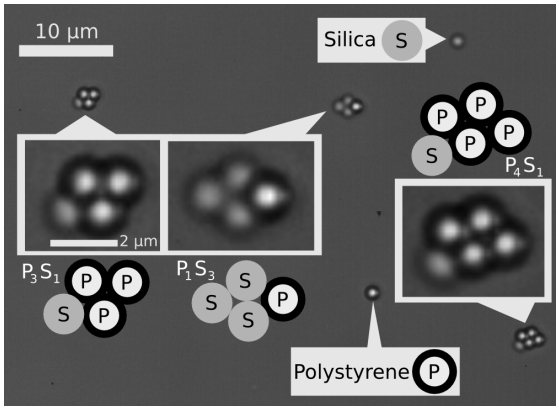

Figure 5.1: Owing to their different indices of refraction, the polystyrene (P) and silica (S) particles can be distinguished in bright-field optical micrographs. The polystyrene particles are bright and surrounded by dark rings whereas the silica particles are dimmer. This micrograph shows a single sphere of each isotope, two 4-particle molecules with different compositions, and a 5-particle molecule. Each N-particle molecule is labeled as $P_X S_{N-X}$, denoting its composition. The 10 µm scale bar applies to the background micrograph. The insets are magnified by about a factor of 3.5X.

tion protocol is provided in Appendix B). We fill the chamber with an aqueous colloidal suspension of polystyrene microspheres (1 µm sulfate latex, Molecular Probes® by Life Technologies,™ lot #1255616, batch #1169661), silica microspheres (1 µm 8000 Series Silica Particle Size Standards, Duke Standards™ from Thermo Scientific, lot #41291, batch #8100-013), and 45 mM sodium dodecyl sulfate (SDS). Microspheres that are approximately 30 nm from the bottom of the chamber are attracted by depletion to the coverslip. The depletion attraction is due to SDS micelles. The overall interaction potential is the sum of the depletion attraction, van der Waals attraction, and electrostatic repulsion (Section 1.2). After the microspheres reach the bottom of the chamber, they diffuse along the coverslip. Rarely do we see them leave the plane. When two microspheres encounter one another, they also experience a depletion attraction, but because this attraction is weaker, they can bind and unbind over periods of minutes (Section 1.2.2).

Over the course of an hour, the silica and polystyrene isotopes form isomers that transition between ground states, all of which are subunits of a triangular lattice, and excited states, which have

floppy modes. The silica and polystyrene isotopes are able to organize into triangular lattice subunits because they have nearly the same size: $1.0\,\mu$m diameter, as measured from the lattice spacing in pure crystals of each. When a bond breaks, the molecule gains an internal degree of freedom along which it can diffuse to form a different isomer or return to its initial configuration. We set the SDS concentration to 45 mM so that the clusters remain bound to the coverslip, but bonds between particles can break and reform, allowing the clusters to equilibrate quickly. Particles detach from the molecules infrequently compared to how often rearrangements within a molecule occur. Molecules also merge together infrequently because the density of microspheres on the surface is low. We therefore assume each molecule to be in equilibrium and independent of its neighbors.

To image the molecules, we use a Nikon Ti-E inverted microscope with a 60X water-immersion objective plus a 1.5X tube lens and a modified stage that allows micrometer-scale control over the in-plane position of the sample. The stage modification is a replica of a design by David Kaz: we remove the stage handle and then mount below the stage two vernier micrometer heads (Newport SM-25 with mounting hardware Newport AB-3) at orthogonal directions and aligned with actuator push blocks (Newport AB-4) also mounted below the stage. We use rubber bands to keep tension between the mounting hardware holding each micrometer head and the actuator push blocks. With these micrometer heads, we move the sample in a raster-scan pattern and capture images on a Photonfocus MV-D1024E-C021-160-CL-14 monochrome CMOS camera with a CameraLink cable connected to an EPIX PIXCI® E8 frame grabber. Each image is approximately $120\,\mu\text{m} \times 120\,\mu\text{m}$ in size. We move the stage in $150\,\mu$m increments to leave a border between frames, ensuring molecules are not double-counted as they diffuse. After translating the stage, we adjust the focus so that silica and polystyrene particles are distinguishable by eye, and then we take a picture (Figure 5.1). Repeating this process, we gather 1,765 images across 4 samples with different stoichiometric ratios of polystyrene and silica. Across the 4 samples, the total area surveyed is approximately $5\text{ mm} \times 5\text{ mm}$ and contains thousands of molecules.

5.2.2 Post-Processing: Identifying Isotopes and Isomers

We computationally analyze the images to classify the molecules and their populations. Our post-processing routine includes locating the individual particles, grouping them into molecules using a cutoff distance to distinguish bound and unbound particles, determining the type of each sphere, and finally categorizing each molecule as a specific isomer. We use Trackpy,[18] an open-source software package based on the work of Crocker and Grier,[21] to locate the particles, and we use custom algorithms for subsequent processing. To classify particles as bound or unbound we set a cutoff distance of $1.18\,\mu\text{m}$. This liberal cutoff distance categorizes molecules with a barely broken bond as the nearest rigid structure, which the molecule was very likely to have occupied just prior or just after the photograph of the cluster was captured.

We identify the molecules from the data returned by Trackpy. To determine which particles belong to a particular molecule, we calculate an $N \times N$ matrix of the distances between each pair of the N particles in a frame. Then, for each particle, we make a list of the other particles within a "molecule-sized" search radius, which we set to be $3.5\,\mu\text{m}$. This distance is sufficiently large to encompass the rigid and non-rigid configurations of molecules with up to five particles. We then assign each particle to a specific, numbered molecule. If the algorithm finds more than one way to assign particles to molecules, it generates and error code. We found zero incidences of such error codes. The list of each particle's associated molecule is then converted to a list of molecules along with a list of which particles are members of each molecule. This method has two failure modes, neither of which is significant in this study. First, two small molecules could lie within the search radius. We check for such configurations by looking at the micrographs annotated with the results. Second, the search radius could be too small and thus truncate large molecules. Such truncations would only affect molecules larger than the 4- and 5-particle molecules analyzed in this study and would result in an error code, which we do not observe.

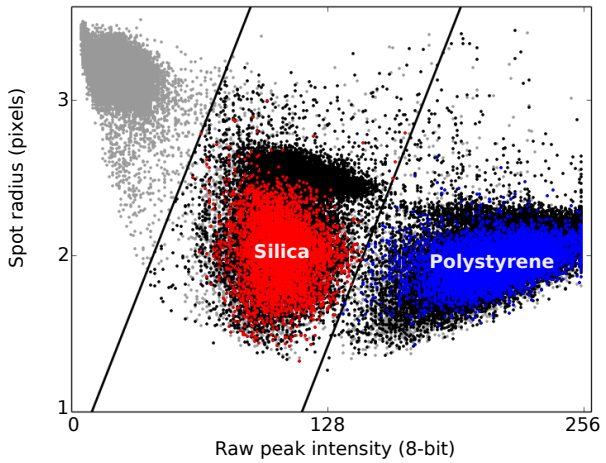

Figure 5.2: A scatter plot of particle attributes reveals found "particles" of three types: rejects (upper left), silica particles (center), and polystyrene particles (lower right). The red and blue points are the particles in rigid 4- and 5-particle molecules. The gray points are false-positives or are particles too close to the border of an image. The cluster of black points above the colored silica and polystyrene regions are single particles of each isotope that are not bound to any other particles.

The next step is to identify which particles are polystyrene and which are silica. To do this, we plot the sizes of the particles returned by Trackpy (the radii of the bright spots shown in Figure 5.1, which are not the true particle radii) versus the particles' intensity maxima in the raw images. In the plot, lines with slopes of 0.033 pixels/intensity value delineate three regions corresponding to rejects, silica particles, and polystyrene particles (Figure 5.2). We chose the positions of these lines heuristically and checked their utility by looking at micrographs annotated with the particles' determined types. In these annotated micrographs, we saw that most particles' types were identified correctly. We corrected misidentifications in our list of particles.

Finally, we classify the configuration of each molecule using a modified adjacency matrix that encodes the locations of different isotopes within a molecule. Previously, in Chapter 3, we used adjacency matrices to distinguish between molecules of different geometries. The standard adjacency matrix indicates only whether the particles are separated or bound (0 or 1). Here, to keep track of bonds, we use a 1 for an S-S bond, a 2 for an P-S bond, and a 3 for a P-P bond (Figure 5.3). To convert the adjacency

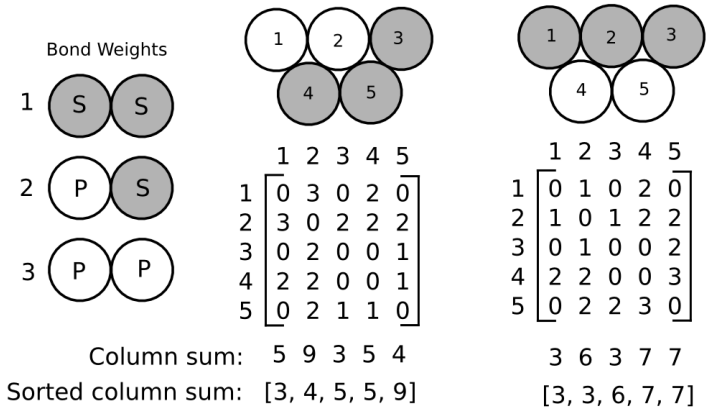

Figure 5.3: These two 5-particle molecules have identical compositions and identical numbers of bonds of each type (S-S, P-S, P-P), yet are distinct isomers. A modified adjacency matrix with 1's, 2's, and 3's indicating different bond types is converted to a sorted column sum that is a unique identifier for all rigid isomers with $N < 6$, regardless of the order in which the particles are numbered.

matrix to an isomer index, we perform a column sum and a sort the resulting list from low to high. This method yields a list of length N that is a unique identifier for each 4- and 5-particle isomer composed of 1 or 2 isotopes (enantiomers get grouped together as in Chapter 3). This approach to identifying isomers is not a general solution to labeling networks constructed from two types of nodes, but it is sufficient for our small molecules. We do not examine molecules with 6 or more particles because they have multiple ground states and require a much larger data set to investigate their isomers. Also, it is difficult to distinguish a dim silica particle surrounded by polystyrene particles from a vacancy in the larger molecules. Fluorescent markers could be used in future studies to analyze larger heterogeneous molecules.

5.3 Results

The smallest isomeric molecules provide us with the first indication that specific isomers our favored. 4-particle molecules containing three particles of one isotope and a single dopant of the other, P_3S_1 and P_1S_3, each have two isomers: the dopant can can be on the short axis or the long axis of the

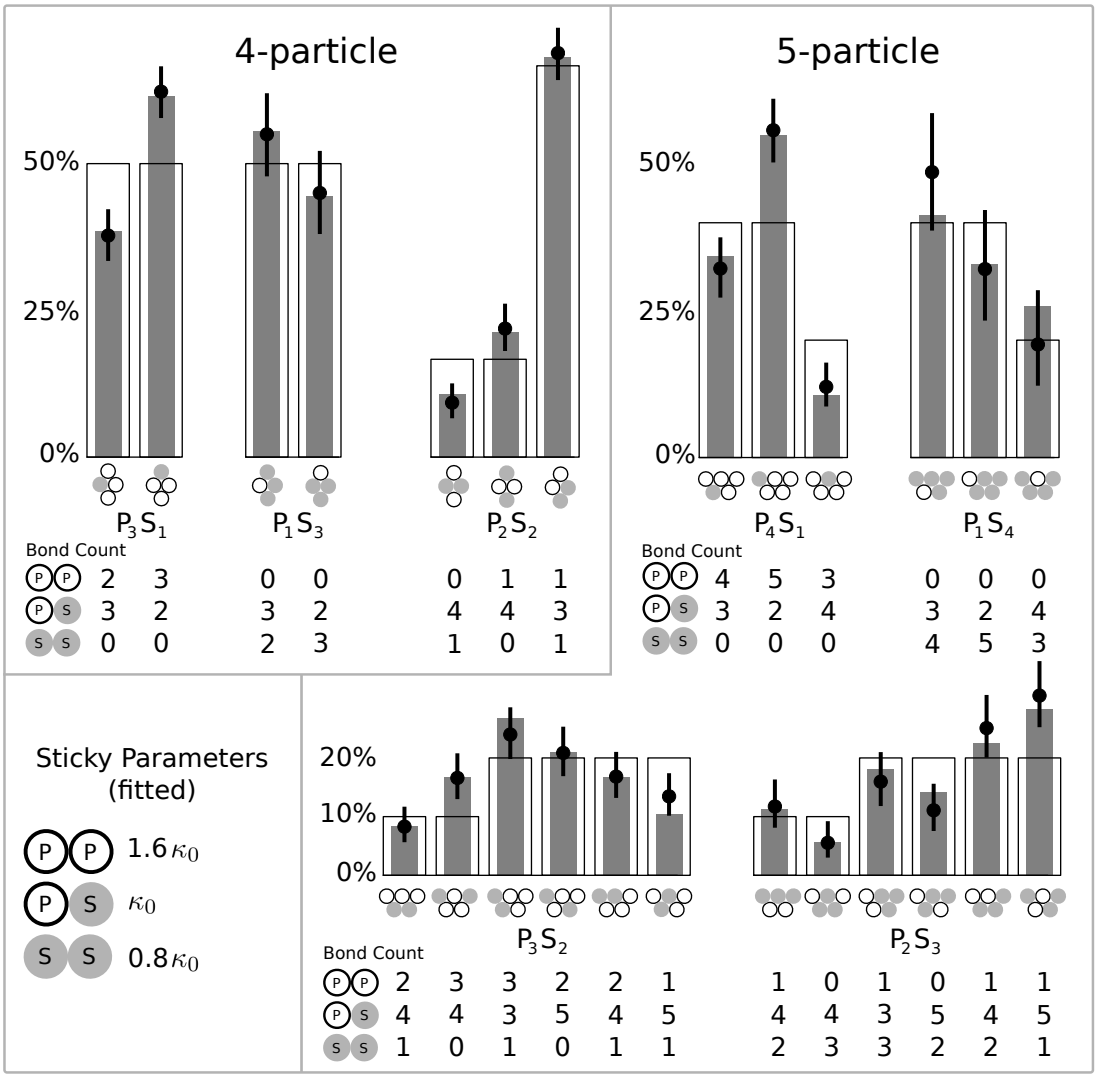

Figure 5.4: The distribution of isomers in our experiments, shown as black points, is captured by a model, shown as gray bars, that includes permutational entropy and two ratios of sticky parameters (see text). The hollow bars show the expected probabilities of isotopes with identical sticky parameters. In this case, the distribution is determined entirely by the permutational entropy. The probabilities within each set of isomers (for example, P_3S_1) sum to 100%. The error bars are 95% confidence intervals.

diamond-shaped ground state (Figure 5.4). If the dopants were randomly distributed, we would see equal numbers of both isomers. However, we find that the silica dopants in the P_3S_1 molecules selectively locate on the long axis in 62.2% of the P_3S_1 molecules. In contrast, we find that the polystyrene dopants in the P_1S_3 molecules are more often located on the short axis, but only by a small margin. These observations show that the silica and polystyrene isotopes differ in such a way as to affect the isomer populations.

The distribution of the other 4-particle isomers, which contain equal numbers of silica and polystyrene particles, also shows deviations from that predicted from random placement of isotopes. We describe the three P_2S_2 isomers in terms of where the two silica particles are located: along the short axis, along the long axis, or along an edge. If the silica particles were randomly distributed, we would expect the isomer with the silica particles along an edge to be the most common, because there are four different ways to place two indistinguishable particles along an edge. These four ways include two chiral enantiomers that we group together because they have identical bond networks. The other isomers can be constructed in only one way. In our experiments, we see that the silica spheres do appear along an edge in $68.8\% \approx 4/6$ of the molecules (Figure 5.4, P_2S_2 molecules). The two less common isomers, however, show significant differences from the random-placement probabilities. The silica particles are twice as likely to be found on the long axis as on the short axis.

The rigid 5-particle trapezoids display 18 different doped states with 1 or 2 dopants each. Particles in the trapezoid can be located at the vertices of the acute angles (2 positions), the vertices of the obtuse angles (2 positions), or on the edge (1 position). The observed probabilities of the various isomers are inconsistent with those predicted by a model that accounts only for the permutational entropy and assumes the interactions have the same strength. We show that molecules with silica dopants on the edge are suppressed and those with silica dopants at the vertices of the acute angles are enhanced. The opposite is true of polystyrene dopants.

5.4 Analysis

To understand the observed probabilities of the different isomers, we construct a statistical mechanical model incorporating permutational entropy and "sticky parameters"[49] that characterize the interactions between pairs of bound spheres (Section 3.4.1). We show that whereas the permutational entropy cannot be changed in the experiments, the sticky parameter, κ, can be tuned to produce a high yield of desired isomers.

The partition function of an isomer, which is proportional to its equilibrium probability, is (Chapter 4):

$$Q = Q_{trans}Q_{rot}Q_{vib(geom)}\prod_{i=1}^{n}\kappa_i, \qquad \text{with} \qquad \kappa_i = \frac{e^{-\beta U_{0i}}}{d\sqrt{\frac{2}{\pi}\beta U''_{0\,i}}}, \tag{5.1}$$

where we have chosen to split Q_{vib} into the purely geometrical part $Q_{vib(geom)}$ and the spring-constant-dependent part, which gets absorbed into the sticky parameter. We can greatly simplify this expression. The translational component, Q_{trans}, is the same for all isomers of a given composition because their shapes and masses are identical, so it may be ignored. Also, the product of the square root of the moment of inertia (in Q_{rot}) and the vibrational partition function is the same for all clusters of a given stoichiometry and geometry (Chapter 4). All that remains is the chirality and symmetry number from Q_{rot} and the sticky parameters, which could be different for each of the n bonds. The sticky parameter is a function of the interaction potential depth U_0, the curvature at the bottom of the interaction potential U''_0, and the microsphere diameter d. The simplified model of the probabilities is then:

$$P_s \propto Q_s \propto \frac{\chi}{\sigma}\prod_{i=1}^{n}\kappa_i \tag{5.2}$$

To apply this model to the experimental system, we calculate χ/σ, and we fit the model to the data to find the sticky parameters of the different types of bonds. We introduced a method of determining

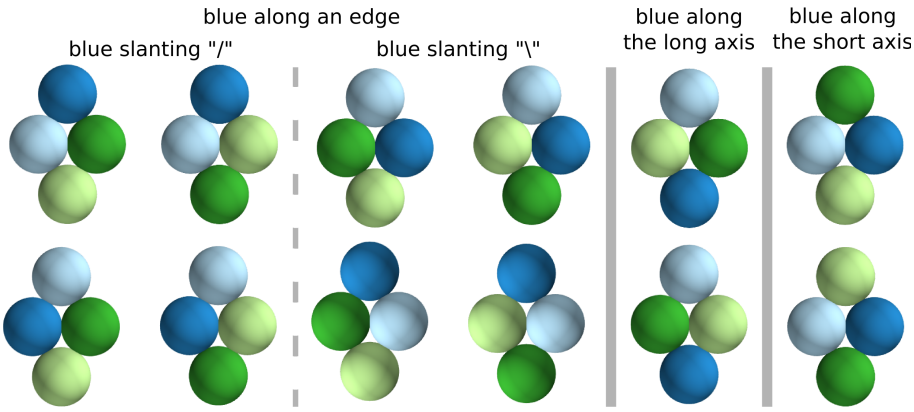

Figure 5.5: The 4! colorings of a 4-particle molecule are reduced to 12 colorings when rotation in the plane is allowed. The 12 colorings are then subdivided according to where the two blue particles are. This subdivision results in 8 configurations with the blue particles along an edge, 2 permutations with the blue particles on the long axis, and 2 permutations with the blue particles on the short axis.

χ and σ in Section 4.5.1. Here we show how that method applies to heterogeneous clusters using the set of 4-particle P_2S_2 molecules. There are 4! ways of coloring the 4-particle molecule, but its 2-fold rotational axis reduces these to the 12 distinct colorings shown in Figure 5.5. We then subdivide the colorings into groups corresponding to the three isomers (including one isomer that is a chiral pair). To do this, we assign any two of the colors to represent silica (two shades of blue in Figure 5.5). There are 8 permutations in which the pair of silica particles are along an edge, 2 permutations where they are on the long axis, and 2 permutations where they are on the short axis. These counts are proportional to the χ/σ of each isomer (along an edge: $\chi = 2, \sigma = 1$, along the long axis: $\chi = 1, \sigma = 2$, along the short axis: $\chi = 1, \sigma = 2$). Alternatively, one can use the binomial coefficient instead of starting with the total number of colorings: there are $\binom{4}{2} = 6$ ways to choose 2 of the 4 particles to be silica. These 6 permutations are then subdivided as before and yield a 4:1:1 ratio of the three isomers. The permutational partition function, χ/σ, determines the probabilities represented by the empty bars in Figure 5.4.

Although there are three sticky parameters in our experiments, P-P, S-S, and P-S, the probabilities

are sensitive only to their ratios. We choose the P-P and S-S sticky parameters as our fit parameters, and we assign the P-S sticky parameter a value κ_0. Using only these two fitting parameters, we obtain an excellent fit to the data when P-P = $1.6\kappa_0$ and S-S = $0.8\kappa_0$. This range of sticky parameters is reasonable as it corresponds to a difference of less than k_BT between the deepest and shallowest interaction potentials, assuming identical curvature U_0''. This fitting procedure shows that the polystyrene particles form stronger bonds than the silica particles do.

To independently verify the reasonableness of the fitted values, we use the *homogeneous* 3- and 4-particle molecules found in the same experimental data set, and we measure the absolute values of κ for P-P and S-S bonds using the method of Holmes-Cerfon *et al.*,[49] which we used in Chapter 3. We find that the P-P bonds have a sticky parameter of approximately 125, and the S-S bonds have a sticky parameter of approximately 50. The factor of 2.5 between these sticky parameters is close to the factor of 2 found by fitting the distributions. We take this as confirmation that the fitted relative P-P and S-S values are sensible, and we estimate that the P-S sticky parameter is between 60 and 80.

Looking back at the data, we can see that the different stickiness values affect the probability distribution in a logical way. The isomers have different numbers of each type of bond ("Bond Count" in Figure 5.4), and the most enhanced isomers have the strongly-binding polystyrene isotopes in locations where they can form the most bonds and the weakly-binding silica isotopes in locations where they can form the fewest.

The isomers with single dopants depend on a single fit parameter. The $P_{N-1}S_1$ molecules have no S-S bonds, so they depend only on the P-P/P-S ratio, while the P_1S_{N-1} molecules have no P-P bonds and depend only on the S-S/P-S ratio. From these isomers alone, we can qualitatively determine the relationships between the three sticky parameters. In the P_3S_1 molecules, the silica dopant is more frequently found with 2-bonds as opposed to 3-bonds. In other words, the P-P bond is preferred, and thus is lower energy (larger κ) than the P-S bond. Using the same logic on the P_1S_3 molecules, we learn that the P-S bond is slightly stronger than the S-S bond. This qualitative ordering of the bonds

from least-sticky to most-sticky (S-S, S-P, P-P) is consistent with the quantitative results of the fit.

The probabilities of isomers with multiple dopants depend on both P-P and S-S interactions. In the P_2S_2 molecules, the model shows us how to maximize the probabilities of any of the three isomers. Setting P-P to be weak and S-S to be strong preferentially locates the silica spheres on the short axis. Setting S-S to be strong and P-P to be weak preferentially locates the silica spheres on the long axis (as seen in our experiments). Setting both P-P and S-S to be weaker than P-S selects for the silica spheres to be located along the edge. Finally, setting both P-P and S-S to be stronger than P-S results in few isomers with silica along the edge and equal amounts of the other two isotopes. Setting the relative interaction strengths between these extremes allows for optimization of different ratios of isomers. For example, setting P-P and S-S to be $4\kappa_0$ should yield equal numbers of all three P_2S_2 isomers.

We have seen that the model with three different types of interactions fits the data well and can be useful in designing a system that spontaneously forms desired isomers. But how did three different interactions arise in the experiments when the depletion attraction should be the same between all isotopes? Our hypothesis is that while the strength of the depletion attraction is the same, the electrostatic and van der Waals forces are different in the three interactions. For example, the silica particles could have a higher surface charge density and, therefore, a stronger repulsive contribution to the interaction potential as compared to the polystyrene particles. This would account for the smaller S-S sticky parameter.

The effect that combinations of sticky parameters have on the probability distributions raises the following question: What is the maximum deviation from the random-chance probability distribution that we could reasonably achieve in an experiment? The constraints are that all the bonds need to be strong enough to make a molecule that persists for long times, yet weak enough to allow rearrangements on an experimental timescale. The transition rates scale inversely with κ.[49] Knowing this, we can estimate that κ could span a factor of 100, perhaps from 40 to 4000. For homogeneous molecules with $\kappa = 40$ a transition would occur every minute or so, and for homogeneous molecules

with $\kappa = 4000$ a transition would occur every day or so. During this time, some spheres may unbind from the coverslip, but using dense spheres would help to counteract these rare events, ensuring the clusters remain in 2D.

With more extreme values of κ than in our experiments, one could enhance single isomers to above 90% probability. In Figure 5.6a, we choose S-S as the weakest interaction and P-P as the strongest, just as in the experiments. But, we choose much more extreme values of κ, with κ_{P-P} one hundred times larger than κ_{S-S}. With these values the model predicts a distribution in which the contribution from permutational entropy is overwhelmed by that of the interaction potentials. The P-P bonds are so strongly favored that many of the preferred isomers show segregation between polystyrene and silica. Interestingly, however, one of the P_3S_2 isomers contains a polystyrene triangle but is suppressed. This is possible because the S-S bonds are much weaker than the P-S bonds.

We find that when both types of self-self bonds are stickier than the mixed-species bonds, a different combination of isomers are selected for than those in Figure 5.6a. This exercise shows that it is not possible to select for any specific isomer. For example, in the set of P_3S_2 molecules, there are two isomers with identical bond counts: 2 P-P, 4 P-S, and 1 S-S (Figure 5.4), so changes in the stickiness will affect the probabilities of these two isomers in the same way. The distribution of isomers of P_4S_1 and P_1S_4 molecules, which each have three isomers but just two types of interactions, cannot be tuned so that any isomer is enhanced. Only those isomers with the dopant at the vertex of the acute angle or along the edge can be optimized from 0-100% probability, and anywhere in between.

Though these values of κ are extreme, they correspond to experimentally realizable potentials. To construct sticky parameters spanning two orders of magnitude as in Figure 5.6a, the depths of the interaction potentials only need to have a difference of $\ln(100)\ k_BT \approx 4.6\ k_BT$ between the weakest and strongest bonds (for example, $U_{0_{S-S}} = -6.5\ k_BT$, $U_{0_{P-S}} = -10\ k_BT$, $U_{0_{P-P}} = -11.1\ k_BT$).

Having shown that engineering the stickiness of the interparticle interaction leads to selective

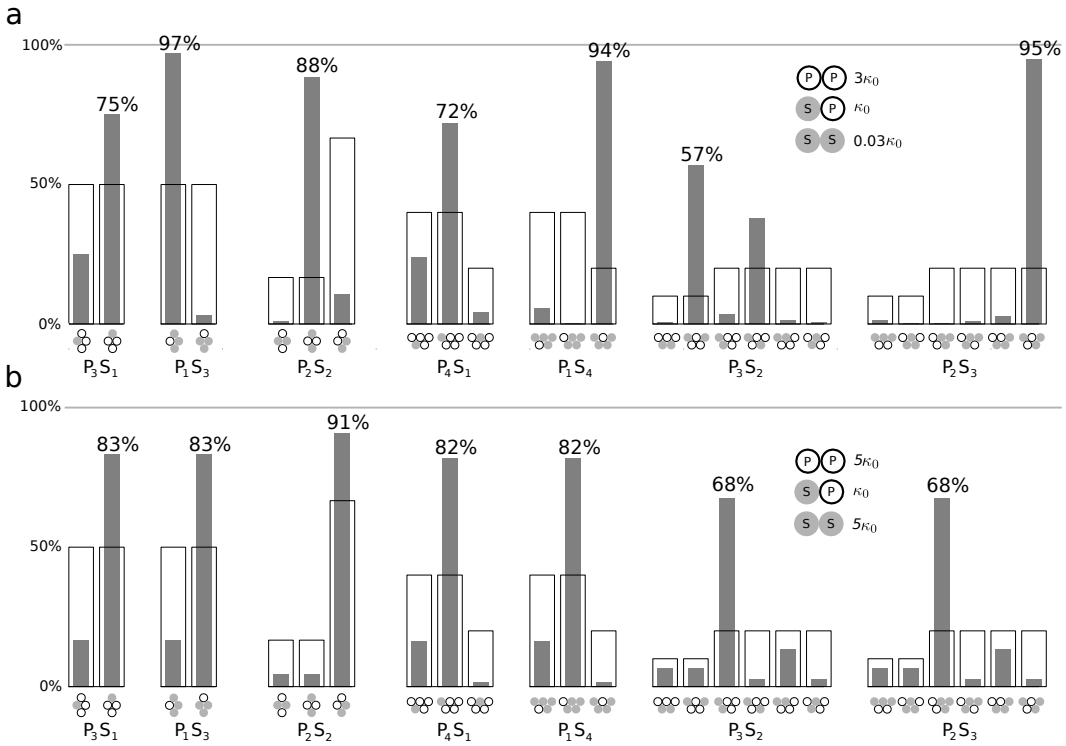

Figure 5.6: Theoretical distributions of isomers with two extreme sets of sticky parameters. In both distributions, certain isomers are enhanced above their random-placement probabilities by more than a factor of 3. Hollow bars show the permutational-entropy-dominated distribution calculated for isotopes with identical sticky parameters, for comparison.

placement of dopants, we now turn to the problem of optimizing the yield of molecules with a specific composition: $P_X S_{N-X}$. Combined, these two design criteria allow for system-wide optimization of a specific isomer.

When we vary the polystyrene fraction, we see that the distribution of compositions of both 4- and 5-particle molecules ($P_X S_{N-X}$) shifts as the total polystyrene fraction increases (Figure 5.7). We calculate the polystyrene fraction, ϕ_P, by counting all of the particles participating in 4 and 5-particle molecules. The distribution of compositions is symmetric at $\phi_P = 0.50$ and shifts to heavily favor molecules with more polystyrene at $\phi_P = 0.73$ (Figure 5.7). The largest differences are at the extrema of these probability distributions: the percentage of molecules composed purely of silica progressively shrinks with each increase in ϕ_P, while the representation of pure polystyrene molecules steadily increases to four times its value at $\phi_P = 0.50$. We see that even small changes in ϕ_P, such as going from 0.50 to 0.55, can change the distributions significantly. In the 4-particle distribution, the P_1S_3 and P_3S_1 molecules have nearly equal probabilities at $\phi_P = 0.50$, but distinctly different ones at $\phi_P = 0.55$, and similarly for the P_1S_4 and P_4S_1 molecules.

Because these molecules are formed by random aggregation in a well-mixed pool of two types of particles, it is natural to model the distribution of compositions using the weighted binomial distribution. We find that it fits the data well with no parameters. The probability that any one particle added to a cluster is polystyrene is simply the polystyrene fraction, ϕ_P. The probability of a certain molecule composition $P_X S_{N-X}$ occurring, from among all molecules of size N, is

$$P(P_X S_{N-X}|\phi_P) = \binom{N}{X} \phi_P^X (1-\phi_P)^{N-X} \tag{5.3}$$

In using this model, we are assuming that the bath of particles is large enough so that the fraction of polystyrene does not change as particles are incorporated into molecules. Note that in our system the number of molecules at a given N changes over time as molecules coalesce. We find that lots of 4- and

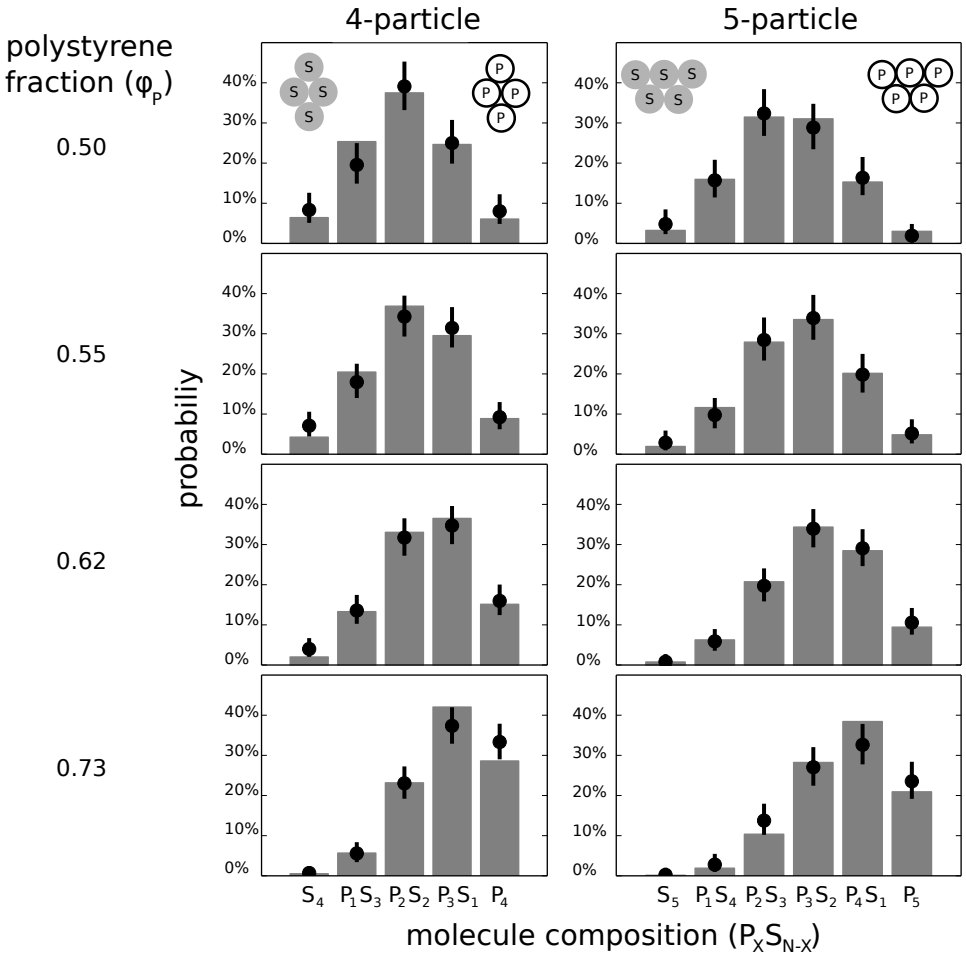

Figure 5.7: The populations of N-particle molecules consist of $N + 1$ compositions ranging from pure silica to pure polystyrene. Experimental data on 4- and 5-particle molecules (black data points with 95% confidence intervals) are modeled well by the weighted binomial distribution (gray bars). Rigid molecules are depicted for reference, but non-rigid molecules are also included in these data.

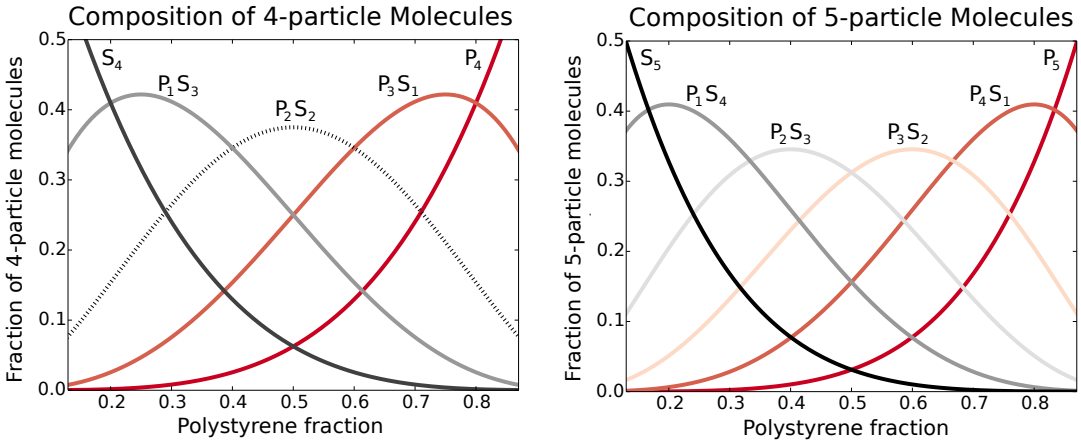

Figure 5.8: The weighted binomial distribution (Equation 5.3) predicts the population distribution as a function of the polystyrene fraction. Each composition has a single maximum. Any two compositions have equal probability at a single polystyrene fraction between 0 and 100%, indicated by where the curves intersect.

5-particle molecules can be observed within a couple of hours after sample preparation. After this, larger molecules dominate. In the future, we plan to grow the molecules in microwells to keep them from coalescing.

As shown in Figure 5.7, the weighted binomial distribution captures all the features of the data. To explore what happens at other volume fractions, we use the model (Figure 5.8). We find that it is possible to maximize any particular composition $P_X S_{N-X}$ by setting the polystyrene fraction to X/N. For example, to optimize $P_1 S_3$ molecules, one would use ϕ_P=0.25. This polystyrene fraction yields a population in which 42% of the 4-particle molecules are $P_1 S_3$. The closer the molecular composition is to $P_{N/2} S_{N/2}$, and the larger the molecule, the smaller is the theoretical maximum yield.

The binomial distribution also shows where we can expect to generate equal numbers of molecules with different compositions. For example, one might want to generate singly-doped molecules of compositions $P_1 S_{N-1}$ and $P_{N-1} S_1$. The optimal polystyrene fraction to obtain iden-

tical yields of N-particle molecules with compositions $P_X S_{N-X}$ and $P_Y S_{N-Y}$ is given by:

$$\phi_P = \frac{\binom{N}{X}^{\frac{1}{Y-X}}}{\binom{N}{X}^{\frac{1}{Y-X}} + \binom{N}{Y}^{\frac{1}{Y-X}}}. \tag{5.4}$$

5.5 Conclusion

Our experiments show that it is possible to control the distribution of self-assembled heterogeneous colloidal molecules through two mechanisms: by varying the interactions (more precisely, sticky parameter ratios) and by varying the stoichiometric ratio (polystyrene fraction). Design criteria emerge from generalizing the findings from the experiments. The models that describe our data well, Equations 5.2 and 5.3, are a guide for maximizing the probability of a particular isotope or combination of isotopes.

With design strategies in hand, we now return to our initial goal of maximizing the yield of any one particular isomer relative to all molecules, not just molecules of the same composition. For example, suppose we want to maximize the P_1S_3 isomer in which the polystyrene sphere is on the short axis. This isomer does not contain a triangular cluster of three silica spheres, which makes it a non-trivial heterogeneous molecule to build. We assume that the molecules cannot coalesce once formed, which would be the case if the experiment were done in microwells. We have four parameters to control: the total particle concentration, the stoichiometric ratio, and the interaction strengths. We would like 100% of the wells to have four particles in them, but Poisson statistics tells us that for random loading the best we can do by simply modifying the total particle concentration is 19.5%. We would like a large fraction of these wells that contain four particles to have one polystyrene particle and three silica particles, so we should use a polystyrene ratio of 0.25, yielding 42% of the four-particle molecules with the correct composition. Finally, the interaction energies must be set so that the dopant prefers to sit on the short axis of the diamond-shaped molecule. The results of Section 5.4 suggest that we can achieve

at least a 90% yield of P_1S_3 molecules with the dopant in the right place. This reasoning suggests that we may be able to construct an equilibrium system in which $19.5\% \times 42\% \times 90\% = 7.4\%$ of the molecules are the exact isomer we desire. This is three times the prevalence that would result from equal interactions and equal numbers of polystyrene and silica.

Exciting directions for future work include studying the transition states in heterogenous molecules, applying these design criteria to heterogeneous three-dimensional molecules, and using more than two kinds of isotopes. Using a combination of different sticky parameters should allow one to maximize the probability of specific types of non-rigid clusters. This could be useful for studying the hydrodynamics of diamond-square-diamond[85] and hinge-like modes (Chapter 3). We used depletion-bound silica and polystyrene microspheres in the experiments to inform our design criteria, but the model is not specific to this type of attractive interaction, nor to these particular isotopes. The model requires only that the interactions be short ranged in comparision to the particle diameter and that the molecule's internal vibrations equilibrate quickly compared to motion along soft modes in the excited states (Chapter 3).[47]

DNA-mediated interactions should allow more control over the sticky parameters and number of interactions.[111,104,112] Another intriguing direction would be to use the temperature-dependence of DNA-mediated interactions to dynamically switch the interaction strengths and modulate the distribution of isomers.[113]

6

Conclusion

Together, the experiments of this thesis show how diffusion, interaction potentials, entropy, and symmetry affect the structure and dynamics of colloidal clusters. In our experimental system we can directly observe internal rearrangement dynamics and measure cluster distributions governed by classical statistical physics. It is a rare opportunity in the study of statistical mechanics to observe these phenomena directly. It has been my great pleasure to immerse myself in the world of colloidal microspheres where particles can be trapped by light, emergent geometrical structures inspire curiosity, and random walks are a physical reality.

6.1 Future Work

6.1.1 Hydrodynamics

Many of the questions that have arisen during the course of this research are about hydrodynamics. We measured the diffusion of single particles far from an interface and depletion-bound to a glass coverslip, and we measured diffusion in soft modes of clusters (Section 3.4.2). In the course of such experiments, the following ideas for further investigation presented themselves:

- No simple model was found to calculate the diffusion of spherical particles on a surface between the lubrication limit and the regime covered by Faxén's Law.[114] Existing experimental techniques such as digital holographic microscopy could be used to make this measurement. Knowing the diffusion coefficient as a function of distance from a surface could inform the design of interaction potentials to obtain different diffusion rates across surfaces.

- While we were able to obtain a lot of information by direct observation, we were not able to observe particle rotations. How do individual microspheres rotationally diffuse when they are bound in clusters or bound to a flat surface? Do they roll, slide, or catch on each other's surfaces?

6.1.2 Collective Motion

The random-walk dynamics of a single sphere or gas of many single spheres are well understood,[19,20,73] but the collective random motion of spheres in a non-rigid cluster is much more complex. Most rearrangements can occur only through collective motion of multiple particles.

- Even a single flexible trimer could be interesting to observe in three dimensions. A flexible trimer has an internal angle ranging from 60° to 180°. If we choose a reference frame where

two of the spheres are fixed, and only the third sphere moves over the surface of the central sphere, half of the surface area it can explore is accessed at angles less than $104.5°$, and half of the area is accessed at angles greater than $104.5°$. Ignoring the geometry of the accessible area, boundary effects, and entropic effects, it seems as though a flexible trimer should have a mean angle the same as that of a water molecule. It would be interesting to do the 3D experiment and see how each of these factors impacts the distribution of angles sampled by the flexible trimer.

6.1.3 Energy Landscape

In this work, we investigated degenerate potential energy minima in the landscape as well as transition paths between minima. In particular, in Chapter 3 we studied 2D clusters of six spheres and measured the occupation probabilities of the 9-bond ground states, and 8- and 7-bond excited states. There is much more to be studied about energy landscapes of colloidal clusters.

- The portion of the energy landscape which we overtly ignored contains the higher energy configurations and configurations with the cluster broken into pieces or even into individual spheres. Ellen Klein *et al.*[115] have started looking at the higher energy portions of the landscape by making chains of particles with $N-1$ bonds in an electric field and then observing how the configuration changes. Chen *et al.*[14] have studied reaction pathways involving cluster fusion and breakup.

- We show that the free energy dictates the occupation probability distribution of excited states. The free energy should also dictate the distribution of time spent within different portions of a soft mode.[49] Our experiments in Chapter 3 did not have the sensitivity to measure this effect. To make this measurement, we would need many uncorrelated, high precision observations of a single soft mode.

- To isolate the motion in the high energy states, it could be useful to use the findings of Chapter 5 and make clusters out of particles that interact with different energies or sticky parameters. For example, the 4-particle diamond has two 4-bond excited states: a hinge-like mode with one particle sticking off of an equilateral triangle and a diamond-square-diamond[85] mode with a flexible square of four particles. The probability of the hinge-like mode could be maximized by using three particles that bind together almost permanently and one particle that binds to the cluster more weakly. This weakly-bound particle would transition between the three sides of the triangle formed by the three other particles. The probability of the diamond-square-diamond mode could be maximized by making the interspecies interactions strong and the self-self interactions weak. This would yield clusters with an A-B-A-B- square of particles that flexes, but rarely forms a central bond.

A

Supplemental Movies

A.0.4 Chapter 3, Movie 1: realtime_transitions.avi

Video segments show the 8-bond transitions between ground states. The clusters transition from the ground state pictured on the left to the ground state pictured above. Connectivity diagrams label the excited state shown in each movie. The micrographs were divided by a background to remove static artifacts and scaled to create identical background intensities. We created this compilation using the Matplotlib library.[116] Video segments are played back at the recording rate of 3 frames per second.

A.0.5 Chapter 3, Movie 2: 10xfast_fourClusters.avi

This clip of 11 minutes (2,000 frames) of raw data shows our experimental arrangement for simultaneously observing four clusters of six spheres while they rotate, translate, and rearrange. The clusters rearrange frequently, but rarely break apart. Playback is ten times faster than the recording rate.

B

Sample Preparation Protocol

We use variations of this sample preparation protocol for all of the experiments in this thesis. We use different thicknesses of Mylar® A film to create sample chambers of different depths. We found that glass slides, as opposed to glass coverslips, were prone to irreversible particle binding events even after plasma cleaning, so we primarily used coverslips. The particular specifications I give here are for the experiments of Chapter 3.

1. Prepare one small (22 mm $\times$ 22 mm) and one large (24 mm $\times$ 60 mm) glass coverslip (VWR Micro Cover Glasses, No. 1) by rinsing with deionized water, drying with high-purity compressed nitrogen, and plasma cleaning for 10 minutes in a PDC-32G Plasma Cleaner/Sterilizer (Harrick Plasma) with the RF Level set to High.

2. To make a sample chamber, center the small coverslip on the large coverslip and separate them with narrow strips of 30-μm-thick Mylar® A film (wiped cleaned with isopropanol) parallel to the long edges of the large coverslip. With the two coverslips clamped together (e.g., with binder clips), use UV-curing Norland Optical Adhesive 61 and a UV lamp to seal the two edges of the small coverslip parallel to the spacers. We find that sealing the four corners and then removing the clips before sealing the two edges works well.

3. Use a pipette to dispense well-dispersed colloidal suspension near one of the unsealed edges of the small coverslip and let capillary action fill the sample chamber. We use a microsphere volume fraction of 7.6×10^{-6}.

4. Use Devcon 5 Minute® Epoxy to seal the last two edges of the small coverslip and to go over the two previously sealed edges for extra protection against evaporation.

Acknowledgements

I thank Jerome Fung for teaching me how to make this style of sample chamber.

C

Occupation Probability Error Bars for Correlated Measurements

C.0.6 Occupation probability error bars

The empirical occupation probability of each excited state is computed by taking the total amount of time we observe its adjacency matrix, and dividing by the total time spent in all configurations with identical energy. To estimate the error bar on this statistic we need to know the number of effectively independent samples. In general this is not the same as the number of data points, since the data are correlated in time: if a cluster has a particular adjacency matrix during one time step, it is more likely to

remain in that adjacency matrix in subsequent time steps. After enough time steps, however, the data become decorrelated, and only then can new data be treated as independent. Roughly, the number of effectively independent samples is the length of the data, divided by the "correlation time" of the data.

A cluster can be thought of as a stochastic process $X_t \in \mathbb{R}^{2N}$, where X_t lists the positions of the particles. An adjacency matrix corresponds to a subset $A \subset \mathbb{R}^{2N}$ of configuration space. We would like to know the average amount of time the system spends in set A, which we write as $p_A = \mathbb{E}1_{(X_t \in A)}$.

Let's define a process $X_A(t) \equiv 1_{(X_t \in A)}$ to be the process that is 1 if $X(t) \in A$, and 0 otherwise. Then $p_A = \mathbb{E}X_A(t)$. Let $\hat{p}_A = \frac{1}{T}\int_0^T X_A(t)dt$ be an estimator for p_A. Let's suppose this estimator is Gaussian, i.e. $\hat{p}_A = p_A + \sigma_A z_A$, where σ_A is the standard deviation of the estimator, and $z_A \sim N(0,1)$ is a copy of the standard normal. Then, we can construct 95% error bars as $e = 1.96\sigma_A$.

How can we determine the standard deviation σ_A? If each observation were independent, then we would have $\sigma_A^2 = \frac{\sigma_{A,0}^2}{n}$, where $\sigma_{A,0}$ is the standard deviation of $X_A(t)$ at a single point in time (equal to $p_A(1-p_A)$ for our process since it is an indicator function), and n is the number of independent observations.

For a process that is correlated in time, a similar result holds provided we replace n with the number of "effectively" independent samples.[117] This is given by $n_{\mathit{eff}} = T/\tau$, where T is the total length of time of the sample, and τ is the correlation time. The correlation time is defined (for a stationary process) from the correlation function $C_A(t) \equiv \mathbb{E}X_A(s)X_A(s+t)$ to be

$$\tau = \frac{1}{C_A(0)}\int_{-\infty}^{\infty} C(t)dt. \tag{C.1}$$

Geometrically, this comes from taking all the area under the correlation function and forming it into a rectangle with the same height as the covariance function at $t = 0$, so the width is τ. Note that $C_A(0) = \sigma_{A,0}^2$.

The estimate for σ_A^2 is then

$$\hat{\sigma}_A^2 = \frac{\sigma_{A,0}^2}{n_{\mathit{eff}}} = \frac{1}{T}\int_{-\infty}^{\infty} C_A(t)dt. \tag{C.2}$$

We have used the fact that $\sigma_{A,0} = C_A(0)$ to rewrite the integral. This integral is calculated numerically from the data following the algorithm described in section B below.

A. Conditional probabilities

The numbers we report in manuscript Figures 3.1 and 3.4 are conditional probabilities: the probability of the cluster having a particular adjacency matrix, conditional on it having a given number of bonds. Calculating the variance of these conditional probabilities requires extra considerations.

Suppose we want to estimate the relative probability of being in set A, conditional on also being in a set B. That is, we would like to estimate $p_{A|B} = P(X(t) \in A | X(t) \in B) = \frac{P(X(t)\in A)}{P(X(t)\in B)} = \frac{\mathbb{E}1_{(X(t)\in A)}}{\mathbb{E}1_{(X(t)\in B)}}$. Let $X_B(t) = 1_{(X(t)\in B)}$. Then an estimator for $p_{A|B}$ is $\hat{p}_{A|B} = \frac{\hat{p}_A}{\hat{p}_B}$. When σ_i is small, this can be expanded as:

$$\frac{\hat{p}_A}{\hat{p}_B} = \frac{p_A + \sigma_A z_A}{p_B + \sigma_B z_B} = \frac{p_A}{p_B} + \frac{\sigma_A z_A}{p_B} - \frac{p_A \sigma_B z_B}{p_B^2} + O(\sigma_i^2).$$

The variance of this estimator for small σ_i is approximately

$$\text{var}\left(\frac{\hat{p}_A}{\hat{p}_B}\right) = \frac{\sigma_A^2}{p_B^2} + \frac{p_A^2\sigma_B^2}{p_B^2} - \frac{2p_A\sigma_A\sigma_B\mathbb{E}z_A z_B}{p_B^2} = \frac{\sigma_A^2}{p_B^2} + \frac{p_A^2\sigma_B^2}{p_B^2} - \frac{2p_A\sigma_{AB}^2}{p_B^2}. \tag{C.3}$$

We can estimate σ_A, σ_B as in the previous section. To compute the cross-correlation term $\sigma_A\sigma_B\mathbb{E}z_A z_B = \sigma_{AB}^2$, we compute the cross-correlation function $C_{AB}(t) = \mathbb{E}X_A(s)X_B(s+t)$ and determine the variance from this, as in the previous section.

B. How to compute the correlation time τ

The correlation function is very noisy at late times, so the integral to compute τ will also be very noisy. In fact, the bias as $n \to \infty$ is 0, but the variance is $O(1)$. Therefore that integral is not a consistent estimator of τ[117].

We use a windowing method to estimate τ, which integrates the correlation function up to a multiple W of the current estimate of τ. As is commonly done, we set $W = 5$. Here is the method in pseudo-code:

$\hat{\rho}_t = C(t)/C(0)$

$\tau = 1$

$t = 1$

`while(`$\tau < Wt$`) {`

$\tau = \tau + 2\hat{\rho}_t$

$t = t + 1$

`}`

This produces an estimator whose variance goes to zero as the number of samples increases, but with a small bias of size $O(e^{-W})$ (if the covariance function has exponential tails.)

C. Why this works

Here is a brief explanation for Equation (C.2). The variance of $\hat{p}_A$ is

$$\begin{aligned}\left(\frac{1}{T}\int_0^T X_A(t)dt\right)\left(\frac{1}{T}\int_0^T X_A(s)ds\right) - p_A^2 &= \frac{1}{T^2}\int_0^T\int_0^T C_A(t-s)dt\,ds \\ &= \frac{1}{2T^2}\int_{-T}^{T}\int_u^{2T-u} C_A(u)dv\,du \\ &= \frac{1}{T}\int_{-T}^{T} C_A(u)(1-\frac{u}{T})du \\ &\approx \frac{1}{T}\int_{-\infty}^{\infty} C_A(u)du.\end{aligned}$$

The last approximation is valid when T is large enough that $C_A(u)$ has decayed.

Acknowledgements

We thank Jonathan Goodman for his assistance with this calculation.

D

Vibrational Modes of 2D Clusters of Six Particles

Section 4.5.2 explains how to compute the vibrational modes of colloidal clusters. In that section the calculation of normal modes for the 3-particle cluster is provided as a worked example. Here, I present the results of the same calculation carried out for the 2D ground states of the 6-particle clusters studied in Chapter 3. As compared to Figure 4.2, the diameters of the gray spheres representing the colloidal particles have been reduced to reveal small amplitude oscillations present in some of these modes. The phases and relative amplitudes of the particle oscillations are encoded in the colors and lengths of the rods extending from the equilibrium particle positions. The particles track the blue ends of the rods during one half of an oscillation cycle and the green ends during the other half. The absolute scale of the oscillations is greatly magnified for purposes of illustration.

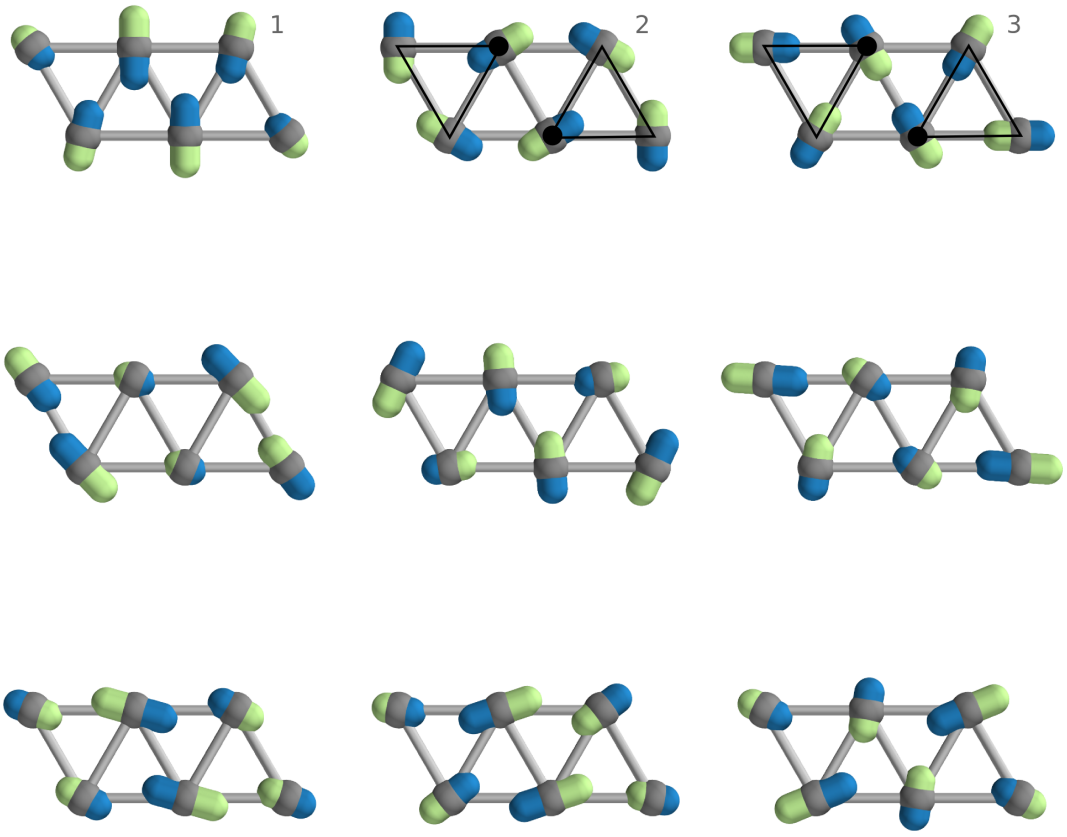

Figure D.1: Parallelogram vibrational modes. Geometrically elegant modes: Mode 1 is a non-radial breathing mode. Mode 2 contains two copies of the 3-particle symmetric mode while mode 3 contains two copies of the 3-particle asymmetric mode (Figure 4.2). Modes 2 and 3 have the same frequency: $\sqrt{1.5}$ for masses and spring constants normalized to 1, identical to the frequency of the symmetric and asymmetric modes of the 3-particle cluster.

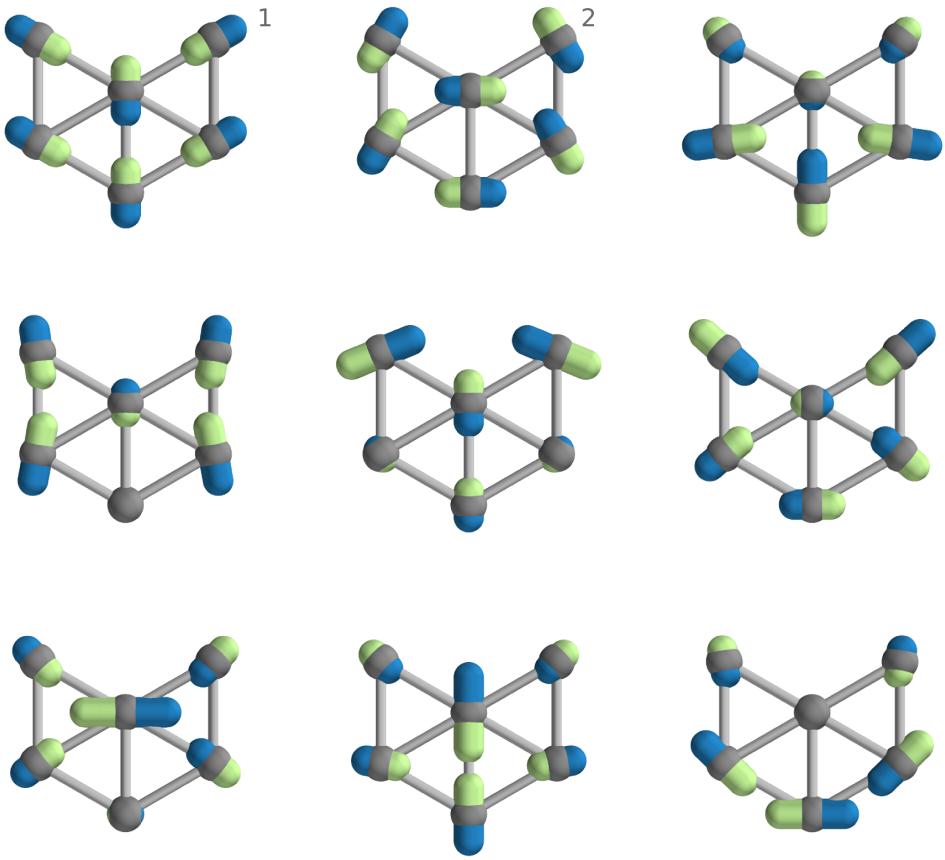

Figure D.2: Chevron vibrational modes. Geometrically elegant modes: In mode 1 all of the particles oscillate along the directions of the triangular lattice. Mode 2 is very similar to mode 1 but with each particle's oscillation direction rotated clockwise or counterclockwise by $\pi/2$. All oscillations in these two modes have equal amplitudes.

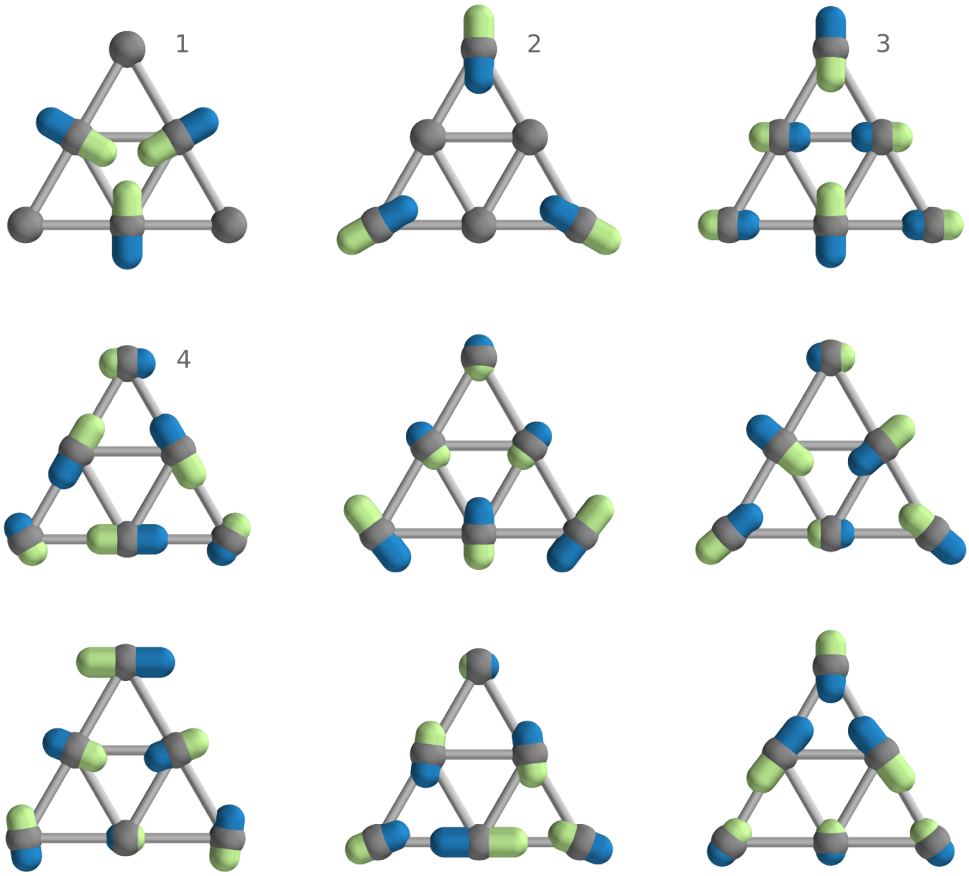

Figure D.3: Triangle vibrational modes. Geometrically elegant modes: Modes 1 and 2 both have three particles fixed in place and three particles undergoing breathing modes. With masses and spring constants normalized to 1, the frequency of mode 1 is $\sqrt{3}$, identical to the frequency of the breathing mode of a 3-particle cluster (Figure 4.2). With the same unit masses and spring constants, the frequency of mode 2 is $\sqrt{1.5}$. Mode 3 consists entirely of purely horizontal and purely vertical oscillations. Mode 4 is composed of an inner triangle and an outer triangle of particles "rotating" in opposite directions as if constrained to tangent lines of concentric circles. The amplitude of the oscillations in the inner ring is twice that of the outer ring.

References

[1] Eric Busseron, Yves Ruff, Emilie Moulin, and Nicolas Giuseppone. Supramolecular self-assemblies as functional nanomaterials. *Nanoscale*, 5(16):7098–7140, July 2013.

[2] Ebbe S. Andersen, Mingdong Dong, Morten M. Nielsen, Kasper Jahn, Ramesh Subramani, Wael Mamdouh, Monika M. Golas, Bjoern Sander, Holger Stark, Cristiano L. P. Oliveira, Jan Skov Pedersen, Victoria Birkedal, Flemming Besenbacher, Kurt V. Gothelf, and Jørgen Kjems. Self-assembly of a nanoscale DNA box with a controllable lid. *Nature*, 459(7243):73–76, May 2009.

[3] G. Yi, S. Jeon, T. Thorsen, V.N. Manoharan, S.R. Quake, D.J. Pine, and Yang S.-M. Generation of uniform photonic balls by template-assisted colloidal crystallization. *Synthetic Metals*, 139(3):803–806, October 2003.

[4] Jin-Gyu Park, Shin-Hyun Kim, Sofia Magkiriadou, Tae Min Choi, Young-Seok Kim, and Vinothan N. Manoharan. Full-spectrum photonic pigments with non-iridescent structural colors through colloidal assembly. *Angewandte Chemie*, 126(11):2943–2947, March 2014.

[5] S. Asakura and F. Oosawa. On interaction between two bodies immersed in a solution of macromolecules. *Journal of Chemical Physics*, 22(7):1255–1256, 1954.

[6] A. Vrij. Polymers at interfaces and interactions in colloidal dispersions. *Pure and Applied Chemistry*, 48(4):471–483, 1976.

[7] Paul L. Biancaniello and John C. Crocker. Line optical tweezers instrument for measuring nanoscale interactions and kinetics. *Review of Scientific Instruments*, 77(11):113702–113702–10, November 2006.

[8] Chad A. Mirkin and Robert L. Letsinger. A DNA-based method for rationally assembling nanoparticles into macroscopic materials. *Nature*, 382(6592):607–609, 1996.

[9] A. Paul Alivisatos, Kai P. Johnsson, Xiaogang Peng, Troy E. Wilson, Colin J. Loweth, Marcel P. Bruchez, and Peter G. Schultz. Organization of 'nanocrystal molecules' using DNA. *Nature*, 382(6592):609–611, August 1996.

[10] W. Benjamin Rogers and John C. Crocker. Direct measurements of DNA-mediated colloidal interactions and their quantitative modeling. *Proceedings of the National Academy of Sciences*, 108(38):15687–15692, 2011.

[11] Randall M. Erb, Hui S. Son, Bappaditya Samanta, Vincent M. Rotello, and Benjamin B. Yellen. Magnetic assembly of colloidal superstructures with multipole symmetry. *Nature*, 457(7232):999–1002, February 2009.

[12] Stefano Sacanna, Laura Rossi, and David J. Pine. Magnetic click colloidal assembly. *Journal of the American Chemical Society*, 134(14):6112–6115, April 2012.

[13] S. Sacanna, W. T. M. Irvine, P. M. Chaikin, and D. J. Pine. Lock and key colloids. *Nature*, 464(7288):575–578, March 2010.

[14] Qian Chen, Jonathan K. Whitmer, Shan Jiang, Sung Chul Bae, Erik Luijten, and Steve Granick. Supracolloidal reaction kinetics of janus spheres. *Science*, 331(6014):199–202, January 2011.

[15] Vinothan N. Manoharan, Mark T. Elsesser, and David J. Pine. Dense Packing and Symmetry in Small Clusters of Microspheres. *Science*, 301(5632):483–487, July 2003.

[16] Guangnan Meng, Natalie Arkus, Michael P. Brenner, and Vinothan N. Manoharan. The free-energy landscape of clusters of attractive hard spheres. *Science*, 327(5965):560–563, January 2010.

[17] Rebecca W. Perry, Guangnan Meng, Thomas G. Dimiduk, Jerome Fung, and Vinothan N. Manoharan. Real-space studies of the structure and dynamics of self-assembled colloidal clusters. *Faraday Discussions*, 159(1):211–234, October 2012.

[18] Daniel B. Allan, Thomas A. Caswell, and Nathan C. Keim. Trackpy v0.2 (doi: 10.5281/zenodo.9971). https://github.com/soft-matter/trackpy, 2014.

[19] Albert Einstein. Über die von der molekularkinetischen Theorie der Wärme gefordert Bewegung von in ruhenden Flüßigkeiten suspendierten Teilchen. (German) [On the molecular-kinetic theory of the movement by heat of particles suspended in liquids at rest]. *Annalen der Physik*, 17(8):549–560, 1905.

[20] Jean Perrin. Mouvement Brownien et réalité moléculaire. *Annales de Chimie et de Physique*, 18:1–114, 1909.

[21] John C. Crocker and David G. Grier. Methods of digital video microscopy for colloidal studies. *Journal of Colloid and Interface Science*, 179(1):298–310, 1996.

[22] P. N. Pusey and W. van Megen. Phase-behavior of concentrated suspensions of nearly hard colloidal spheres. *Nature*, 320(6060):340–342, 1986.

[23] Wilson Poon. Colloids as Big Atoms. *Science*, 304(5672):830–831, May 2004.

[24] Rajesh Ganapathy, Mark R. Buckley, Sharon J. Gerbode, and Itai Cohen. Direct measurements of island growth and step-edge barriers in colloidal epitaxy. *Science*, 327(5964):445–448, January 2010.

[25] Jacob N. Israelachvili. *Intermolecular and Surface Forces*. Academic Press, Burlington, MA, third edition, June 2011.

[26] Aysen Tulpar, Vivek Subramanian, and William Ducker. Decay lengths of double-layer forces in solutions of partly associated ions. *Langmuir*, 17(26):8451–8454, 2001.

[27] Tara D. Iracki, Daniel J. Beltran-Villegas, Shannon L. Eichmann, and Michael A. Bevan. Charged micelle depletion attraction and interfacial colloidal phase behavior. *Langmuir*, 26(24):18710–18717, 2010.

[28] W. B. Russel, D. A. Saville, and W. R. Schowalter. *Colloidal dispersions*. Cambridge monographs on mechanics and applied mathematics. Cambridge University Press, Cambridge ; New York, 1991.

[29] Henk N. W. Lekkerkerker and Remco Tuinier. *Colloids and the Depletion Interaction*. Springer Science+Business Media B.V., Dordrecht, 2011.

[30] Eric W. Weisstein. Spherical cap. from *MathWorld*–A Wolfram Web Resource. http://mathworld.wolfram.com/SphericalCap.html.

[31] P. D. Kaplan, Luc P. Faucheux, and Albert J. Libchaber. Direct observation of the entropic potential in a binary suspension. *Physical Review Letters*, 73(21):2793–2796, November 1994.

[32] Natalie Arkus, Vinothan N. Manoharan, and Michael P. Brenner. Minimal energy clusters of hard spheres with short range attractions. *Physical Review Letters*, 103(11):118303, 2009.

[33] Natalie Arkus, Vinothan N. Manoharan, and Michael P. Brenner. Deriving finite sphere packings. *SIAM Journal on Discrete Mathematics*, 25(4):1860–1901, 2011.

[34] John W. R. Morgan and David J. Wales. Energy landscapes of planar colloidal clusters. *Nanoscale*, 6(18):10717–10726, September 2014.

[35] J. Clerk Maxwell. On the calculation of the equilibrium and stiffness of frames. *Philosophical Magazine Series 4*, 27(182):294–299, April 1864.

[36] John C. Crocker. Turning away from high symmetry. *Science*, 327(5965):535–536, 2010.

[37] V. J. Anderson and H. N. W. Lekkerkerker. Insights into phase transition kinetics from colloid science. *Nature*, 416(6883):811–815, 2002.

[38] C. Patrick Royall, Stephen R. Williams, Takehiro Ohtsuka, and Hajime Tanaka. Direct observation of a local structural mechanism for dynamic arrest. *Nature Materials*, 7(7):556–561, July 2008.

[39] Willem K Kegel and Alfons van Blaaderen. Direct observation of dynamical heterogeneities in colloidal Hard-Sphere suspensions. *Science*, 287(5451):290–293, January 2000.

[40] J. R. Savage, D. W. Blair, A. J. Levine, R. A. Guyer, and A. D. Dinsmore. Imaging the sublimation dynamics of colloidal crystallites. *Science*, 314(5800):795–798, 2006.

[41] Peter J. Lu, Emanuela Zaccarelli, Fabio Ciulla, Andrew B. Schofield, Francesco Sciortino, and David A. Weitz. Gelation of particles with short-range attraction. *Nature*, 453(7194):499–503, 2008.

[42] U. Gasser, Eric R Weeks, Andrew Schofield, P. N Pusey, and D. A Weitz. Real-space imaging of nucleation and growth in colloidal crystallization. *Science*, 292(5515):258–262, April 2001.

[43] J. R. Savage and A. D. Dinsmore. Experimental evidence for two-step nucleation in colloidal crystallization. *Physical Review Letters*, 102(19):198302, May 2009.

[44] David J Wales. Energy landscapes of clusters bound by short-ranged potentials. *ChemPhysChem*, 11(12):2491–2494, 2010.

[45] Robert S. Hoy, Jared Harwayne-Gidansky, and Corey S. O'Hern. Structure of finite sphere packings via exact enumeration: Implications for colloidal crystal nucleation. *Physical Review E*, 85(5):051403, May 2012.

[46] Robert S. Hoy and Corey S. O'Hern. Minimal energy packings and collapse of sticky tangent hard-sphere polymers. *Physical Review Letters*, 105(6):068001, 2010.

[47] Miranda Holmes-Cerfon. Enumerating nonlinearly rigid sphere packings. *arXiv:1407.3285 [cond-mat]*, July 2014. arXiv: 1407.3285.

[48] Robert S. Hoy. Structure and dynamics of model colloidal clusters with short-range attractions. *Physical Review E*, 91(1):012303, January 2015.

[49] Miranda Holmes-Cerfon, Steven J. Gortler, and Michael P. Brenner. A geometrical approach to computing free-energy landscapes from short-ranged potentials. *Proceedings of the National Academy of Sciences*, 110(1):E5–E14, January 2013.

[50] Florent Calvo, Jonathan P. K. Doye, and David J. Wales. Energy landscapes of colloidal clusters: thermodynamics and rearrangement mechanisms. *Nanoscale*, 4(4):1085–1100, 2012.

[51] G. A Vliegenthart and P. van der Schoot. Kinetics of depletion interactions. *Europhysics Letters*, 62(4):600–606, 2003.

[52] Thierry Biben, Peter Bladon, and Daan Frenkel. Depletion effects in binary hard-sphere fluids. *Journal of Physics: Condensed Matter*, 8(50):10799–10821, December 1996.

[53] X. Wu, R. H. Pelton, A. E. Hamielec, D. R. Woods, and W. Mcphee. The kinetics of poly(n-isopropylacrylamide) microgel latex formation. *Colloid and Polymer Science*, 272(4):467–477, 1994.

[54] M. Andersson and S. L. Maunu. Structural studies of poly(n-isopropylacrylamide) microgels: Effect of SDS surfactant concentration in the microgel synthesis. *Journal of Polymer Science Part B-Polymer Physics*, 44(23):3305–3314, 2006.

[55] Douglas B. Weibel, Willow R. DiLuzio, and George M. Whitesides. Microfabrication meets microbiology. *Nature Reviews Microbiology*, 5(3):209–218, 2007.

[56] A. D. Dinsmore, A. G. Yodh, and D. J. Pine. Entropic control of particle motion using passive surface microstructures. *Nature*, 383(6597):239–242, 1996.

[57] Ben Ovryn and Steven H. Izen. Imaging of transparent spheres through a planar interface using a high-numerical-aperture optical microscope. *Journal of the Optical Society of America A*, 17(7):1202–1213, July 2000.

[58] B. Ovryn. Three-dimensional forward scattering particle image velocimetry applied to a microscopic field-of-view. *Experiments in Fluids*, 29(1):S175–S184, December 2000.

[59] Sang-Hyuk Lee, Yohai Roichman, Gi-Ra Yi, Shin-Hyun Kim, Seung-Man Yang, Alfons van Blaaderen, Peter van Oostrum, and David G. Grier. Characterizing and tracking single colloidal particles with video holographic microscopy. *Optics Express*, 15(26):18275–18282, 2007.

[60] Sang-Hyuk Lee and David G. Grier. Holographic microscopy of holographically trapped three-dimensional structures. *Optics Express*, 15(4):1505–1512, 2007.

[61] Jerome Fung, K. Eric Martin, Rebecca W. Perry, David M. Kaz, Ryan McGorty, and Vinothan N. Manoharan. Measuring translational, rotational, and vibrational dynamics in colloids with digital holographic microscopy. *Optics Express*, 19(9):8051–8065, April 2011.

[62] Jerome Fung, Rebecca W. Perry, Thomas G. Dimiduk, and Vinothan N. Manoharan. Imaging multiple colloidal particles by fitting electromagnetic scattering solutions to digital holograms. *Journal of Quantitative Spectroscopy and Radiative Transfer*, 113(18):2482–2489, December 2012.

[63] Daniel W. Mackowski and Michael I. Mishchenko. Calculation of the T matrix and the scattering matrix for ensembles of spheres. *Journal of the Optical Society of America A*, 13(11):2266–2278, November 1996.

[64] Anna Wang, Thomas G. Dimiduk, Jerome Fung, Sepideh Razavi, Ilona Kretzschmar, Kundan Chaudhary, and Vinothan N. Manoharan. Using the discrete dipole approximation and holographic microscopy to measure rotational dynamics of non-spherical colloidal particles. *Journal of Quantitative Spectroscopy and Radiative Transfer*, 146:499–509, October 2014.

[65] Stefka N. Kasarova, Nina G. Sultanova, Christo D. Ivanov, and Ivan D. Nikolov. Analysis of the dispersion of optical plastic materials. *Optical Materials*, 29(11):1481–1490, July 2007.

[66] J. Sheng, E. Malkiel, and J. Katz. Digital holographic microscope for measuring three-dimensional particle distributions and motions. *Applied Optics*, 45(16):3893–3901, 2006.

[67] Lisa Dixon, Fook C. Cheong, and David G. Grier. Holographic deconvolution microscopy for high-resolution particle tracking. *Optics Express*, 19(17):16410–16417, 2011.

[68] Robert G. Newcombe. Two-sided confidence intervals for the single proportion: comparison of seven methods. *Statistics in Medicine*, 17(8):857–872, April 1998.

[69] J. C. Crocker, J. A. Matteo, A. D. Dinsmore, and A. G. Yodh. Entropic attraction and repulsion in binary colloids probed with a line optical tweezer. *Physical Review Letters*, 82(21):4352–4355, 1999.

[70] David R. Nelson and Frans Spaepen. Polytetrahedral order in condensed matter. *Solid State Physics*, 42:1–90, 1989.

[71] T. A. Witten and L. M. Sander. Diffusion-limited aggregation, a kinetic critical phenomenon. *Physical Review Letters*, 47(19):1400–1403, November 1981.

[72] N. Sloane, R. Hardin, T. Duff, and J. Conway. Minimal-energy clusters of hard spheres. *Discrete & Computational Geometry*, 14(1):237–259, December 1995.

[73] Howard C. Berg. *Random Walks in Biology*. Princeton University Press, 1993.

[74] Eric R. Weeks and D. A. Weitz. Properties of cage rearrangements observed near the colloidal glass transition. *Physical Review Letters*, 89(9):095704, August 2002.

[75] Carolina Brito and Matthieu Wyart. Heterogeneous dynamics, marginal stability and soft modes in hard sphere glasses. *Journal of Statistical Mechanics: Theory and Experiment*, 2007(08):L08003, August 2007.

[76] Peter Yunker, Zexin Zhang, Kevin B. Aptowicz, and A. G. Yodh. Irreversible rearrangements, correlated domains, and local structure in aging glasses. *Physical Review Letters*, 103(11):115701, 2009.

[77] Gregg Lois, Jerzy Blawzdziewicz, and Corey S. O'Hern. Jamming transition and new percolation universality classes in particulate systems with attraction. *Physical Review Letters*, 100(2):028001, January 2008.

[78] Peter J. Yunker, Ke Chen, Zexin Zhang, and A. G. Yodh. Phonon spectra, nearest neighbors, and mechanical stability of disordered colloidal clusters with attractive interactions. *Physical Review Letters*, 106(22):225503, June 2011.

[79] Peter J. Yunker, Zexin Zhang, Matthew Gratale, Ke Chen, and A. G. Yodh. Relationship between neighbor number and vibrational spectra in disordered colloidal clusters with attractive interactions. *The Journal of Chemical Physics*, 138(12):12A525, January 2013.

[80] Henry Eyring. The activated complex in chemical reactions. *The Journal of Chemical Physics*, 3(2):107–115, February 1935.

[81] E. Wigner. The transition state method. *Transactions of the Faraday Society*, 34(0):29–41, January 1938.

[82] Juro Horiuti. On the statistical mechanical treatment of the absolute rate of chemical reaction. *Bulletin of the Chemical Society of Japan*, 13(1):210–216, 1938.

[83] P. D. Kaplan, J. L. Rouke, A. G. Yodh, and D. J. Pine. Entropically driven surface phase separation in binary colloidal mixtures. *Physical Review Letters*, 72(4):582–585, January 1994.

[84] Eric Jones, Travis Oliphant, Pearu Peterson, et al. SciPy: Open source scientific tools for Python, 2001–. [Online; accessed 2014-11-12].

[85] William N. Lipscomb. Framework rearrangement in boranes and carboranes. *Science*, 153(3734):373–378, July 1966.

[86] Michael K. Gilson and Karl K. Irikura. Symmetry numbers for rigid, flexible, and fluxional molecules: Theory and applications. *The Journal of Physical Chemistry B*, 114(49):16304–16317, December 2010.

[87] Weinan E and Eric Vanden-Eijnden. Transition-path theory and path-finding algorithms for the study of rare events. *Annual Review of Physical Chemistry*, 61(1):391–420, 2010.

[88] Ian C. Jenkins, Marie T. Casey, James T. McGinley, John C. Crocker, and Talid Sinno. Hydrodynamics selects the pathway for displacive transformations in DNA-linked colloidal crystallites. *Proceedings of the National Academy of Sciences of the United States of America*, 111(13):4803–4808, April 2014.

[89] Norman Ralph Davidson. *Statistical Mechanics*. MacGraw-Hill, 1962.

[90] Dudley R. Herschbach, Harold S. Johnston, and Donald Rapp. Molecular partition functions in terms of local properties. *The Journal of Chemical Physics*, 31(6):1652–1661, December 1959.

[91] M.E. Cates. Self-assembly and entropy of colloidal clusters. http://www.condmatjournalclub.org/wp-content/uploads/2012/12/JCCM_DECEMBER2012_01.pdf, December 2012.

[92] Kenneth Sanborn Pitzer. *Quantum Chemistry*. Constable, 1953.

[93] Mattias Edén and Malcolm H. Levitt. Computation of orientational averages in solid-state nmr by gaussian spherical quadrature. *Journal of Magnetic Resonance*, 132(2):220–239, June 1998.

[94] Robert E. Tuzun, Donald W. Noid, Bobby G. Sumpter, and Chao Yang. Normal coordinate analysis for polymer systems: Capabilities and new opportunities. *Macromolecular Theory and Simulations*, 11(7):711–728, September 2002.

[95] Eran Eyal, Lee-Wei Yang, and Ivet Bahar. Anisotropic network model: Systematic evaluation and a new web interface. *Bioinformatics*, 22(21):2619–2627, November 2006.

[96] Stéfan van der Walt, S. Chris Colbert, and Gaël Varoquaux. The NumPy array: A structure for efficient numerical computation. *Computing in Science & Engineering*, 13(2):22–30, March 2011.

[97] Amir Haji-Akbari, Michael Engel, and Sharon C. Glotzer. Phase diagram of hard tetrahedra. *The Journal of Chemical Physics*, 135(19):194101, November 2011.

[98] SymPy Development Team. Sympy: Python library for symbolic mathematics. http://www.sympy.org, 2014.

[99] Stefano Sacanna, William T. M. Irvine, Laura Rossi, and David J. Pine. Lock and key colloids through polymerization-induced buckling of monodisperse silicon oil droplets. *Soft Matter*, 7(5):1631–1634, February 2011.

[100] Yu Wang, Yufeng Wang, Xiaolong Zheng, Gi-Ra Yi, Stefano Sacanna, David J. Pine, and Marcus Weck. Three-dimensional lock and key colloids. *Journal of the American Chemical Society*, 136(19):6866–6869, May 2014.

[101] Evan Spruijt, Henriëtte E. Bakker, Thomas E. Kodger, Joris Sprakel, Martien A. Cohen Stuart, and Jasper van der Gucht. Reversible assembly of oppositely charged hairy colloids in water. *Soft Matter*, 7(18):8281–8290, September 2011.

[102] Bhuvnesh Bharti, Gerhard H. Findenegg, and Orlin D. Velev. Co-assembly of oppositely charged particles into linear clusters and chains of controllable length. *Scientific Reports*, 2, December 2012.

[103] Nicholas B. Schade, Miranda C. Holmes-Cerfon, Elizabeth R. Chen, Dina Aronzon, Jesse W. Collins, Jonathan A. Fan, Federico Capasso, and Vinothan N. Manoharan. Tetrahedral colloidal clusters from random parking of bidisperse spheres. *Physical Review Letters*, 110(14):148303, April 2013.

[104] Jesse W. Collins. *Self-Assembly of Colloidal Spheres with Specific Interactions*. PhD thesis, Harvard University, May 2014.

[105] Yufeng Wang, Yu Wang, Dana R. Breed, Vinothan N. Manoharan, Lang Feng, Andrew D. Hollingsworth, Marcus Weck, and David J. Pine. Colloids with valence and specific directional bonding. *Nature*, 491(7422):51–55, November 2012.

[106] Alfons van Blaaderen. Colloidal molecules and beyond. *Science*, 301(5632):470–471, 2003.

[107] Adeline Perro, Etienne Duguet, Olivier Lambert, Jean-Christophe Taveau, Elodie Bourgeat-Lami, and Serge Ravaine. A chemical synthetic route towards "colloidal molecules". *Angewandte Chemie*, 121(2):367–371, January 2009.

[108] Etienne Duguet, Anthony Désert, Adeline Perro, and Serge Ravaine. Design and elaboration of colloidal molecules: an overview. *Chemical Society Reviews*, 40(2):941, 2011.

[109] Fan Li, David P. Josephson, and Andreas Stein. Colloidal Assembly: The Road from Particles to Colloidal Molecules and Crystals. *Angewandte Chemie International Edition*, 50(2):360–388, January 2011.

[110] Michael Grünwald and Phillip L. Geissler. Patterns without patches: Hierarchical self-assembly of complex structures from simple building blocks. *ACS Nano*, 8(6):5891–5897, June 2014.

[111] Nienke Geerts and Erika Eiser. DNA-functionalized colloids: Physical properties and applications. *Soft Matter*, 6(19):4647, 2010.

[112] Zorana Zeravcic and Michael P. Brenner. Self-replicating colloidal clusters. *Proceedings of the National Academy of Sciences*, 111(5):1748–1753, February 2014.

[113] W. Benjamin Rogers and Vinothan N. Manoharan. Programming colloidal phase transitions with DNA strand displacement. *Science*, 347(6222):639–642, February 2015.

[114] J. Happel and H. Brenner. *Low Reynolds Number Hydrodynamics: With Special Applications to Particulate Media*. Springer Science & Business Media, September 1983.

[115] Ellen Klein. Ground states and folding dynamics of colloidal clusters. In *Bulletin of the American Physical Society APS March Meeting 2015*, volume 60.

[116] John D. Hunter. Matplotlib: A 2D graphics environment. *Computing in Science & Engineering*, 9(3):90–95, May 2007.

[117] A. Sokal. *Monte Carlo Methods in Statistical Mechanics: Foundations and New Algorithms*, volume 361 of *NATO ASI Series*, pages 131–192. Springer US, 1997.